2018

Mechano-Magnetic Telemetry For Urban Infrastructure Monitoring

Daniel Jerome Orfeo
University of Vermont

MECHANO-MAGNETIC TELEMETRY FOR URBAN INFRASTRUCTURE MONITORING

A Thesis Presented

by

Daniel J. Orfeo

to

The Faculty of the Graduate College

of

The University of Vermont

In Partial Fulfillment of the Requirements
for the Degree of Master of Science
Specializing in Mechanical Engineering

January, 2018

Defense Date: December 13, 2017
Thesis Examination Committee:

Dryver R. Huston, Ph.D., Advisor
Tian Xia, Ph.D., Chairperson
Darren L. Hitt, Ph.D.
Cynthia J. Forehand, Ph.D., Dean of the Graduate College

ABSTRACT

Many cities seek utilities monitoring with centrally managed Internet of Things (IoT) systems. This requires the development of numerous reliable low-cost wireless sensors, such as water temperature and flow meters, that can transmit information from subterranean pipes to surface-mounted receivers. Traditional radio communication systems are either unable to penetrate through multiple feet of earthen and manmade material, or have impractically large energy requirements which necessitate either frequent replacement of batteries, or a complex (and expensive) built-in energy harvesting system. Magnetic signaling systems do not suffer from this drawback: low-frequency electromagnetic waves have been shown to penetrate well through several feet of earth and water. In the past, these signals were too weak for practical use; however, this has changed with the recent proliferation of high-sensitivity magnetometers and compact rare-earth magnets.

A permanent magnet can be either rotated or vibrated to create an oscillating magnetic field. Utilizing this phenomenon, two types of magnetic transmitter are investigated in this study: one which uses a propeller to directly rotate a diametrically magnetized neodymium magnet; and a second in which a permanent magnet is oscillated back-and-forth across a novel soft-magnet Y-stator, which projects a switching magnetic field. In principle, these oscillating magnetic fields can be used for communication from subterranean infrastructure sensors—such as flow meters and leak detection devices—to an aboveground long range (LoRa) radio-networked Arduino receiver equipped with a magnetometer. Simulation software models the oscillating electromagnetic fields produced by the Y-stator configuration. Laboratory performance and field tests establish the capability of two IoT-linked leak-detection sensors that use magnetic telemetry. Remote datalogging demonstrates the viability of integrating many sensors and surface receivers into a single LoRa wireless IoT network.

CITATIONS

Material from this thesis is in preparation for submission to Frontiers in Built Environment | Structural Sensing on December 22, 2017 in the following form:

Orfeo, D., Burns, D., Farrell, R., Qin, M., Mitchell, H., Ou, C., Xia, T., Huston, D.. (2017). Mechano-Magnetic Telemetry for Underground Water Infrastructure Monitoring. *Front. Built Environ.*

ACKNOWLEDGEMENTS

I would like to express my gratitude for the time and effort put in by my committee members. I would like to thank my advisor Dr. Huston for his support and guidance, and for giving me the opportunity to do research in his laboratory. I would also like to thank Dr. Xia for his helpful advice and critiques, and for agreeing to be the Chair of my thesis committee. Finally, I would like to thank Dr. Hitt for taking the time to be on my committee, and to advise me in this process.

I would also like to thank Robert Farrell and Yu Zhang, who have helped me throughout this project. I would like to express my appreciation to Dr. Burns, for his invaluable expertise and involvement with many aspects of design, fabrication, and testing. I would also like to thank Jon Miller and White River Technologies for advice and use of the magnetometer. This work has been supported by NSF grants 1647095 and 1640687, the University of Vermont SPARK Fund, and VT EPSCoR.

Finally, I want to thank my parents, and my wonderful partner, Amanda, for their support and love.

TABLE OF CONTENTS

Page

LIST OF TABLES

LIST OF FIGURES

LIST OF ABBREVIATIONS

ASCE	American Society of Civil Engineers
FFT	fast Fourier transform
FM	frequency modulated
IED	improvised explosive device
IoT	internet of things
LoRa	Long Range, low power wireless (868 or 915 MHz)
PLA	polylactic acid (plastic)
TTE	through-the-earth communication system
VLF	Very Low Frequency (3 kHz to 30 kHz)
ω_n	natural frequency (radians per second)
k	spring constant (Newtons per meter)
m	mass (kilograms)
κ	coupling strength (Winfree model)
$\theta_i(t)$	phase of the *i*th oscillator at time *t*
$g(\omega)$	symmetric, unimodal distribution
Γ	width of distribution $g(\omega)$
$X(\theta_j)$	phase-dependent effect (Winfree model)
$Z(\theta_i)$	sensitivity function (Winfree model)
K	coupling constant (Kuramoto model)
$r(t)$	complex order parameter
K_c	critical value of coupling constant (Kuramoto model)

ω_0	mean value of $g(\omega)$ used by Yeung
τ	time delay (seconds)
α	phase frustration parameter
$\xi_i(t)$	white noise function

1 INTRODUCTION

1.1 Underground Infrastructure Monitoring

Many cities seek methods of monitoring utility infrastructure with centrally managed Internet of Things (IoT) systems. This requires the development of many reliable low-cost wireless sensors, such as water temperature and flow meters, that can transmit information from subterranean pipes to aboveground receivers. Most materials, including earth and sea water, do not interact with magnetic fields that oscillate below 3,000 Hz. The ability of low frequency magnetic waves to penetrate through the earth and sea water opens up the possibility for communicating in challenging conditions that defeat most other techniques, such as traditional radio communication systems. Such radio systems are either unable to penetrate through multiple feet of earthen and manmade material, or have impractically large energy requirements which necessitate either frequent replacement of batteries, or a complex (and expensive) built-in energy harvesting system. Magnetic signaling systems do not suffer from this drawback: low-frequency electromagnetic waves can penetrate well through several feet of earth and water. In the past, these signals were too weak for practical use; however, this has changed with the recent proliferation of high-sensitivity magnetometers and compact rare-earth magnetic sources.

1.2 Recent Advances Enable Compact Magnetic Telemetry

Low-frequency magnetic fields have traditionally been generated and received with either large electric induction coils, or massive antennas which are physically resonant with the desired transmission frequency. Low frequency electromagnetic waves have free-space wavelengths which measure from tens to thousands of kilometers, making traditional

antenna designs—which must be resonant with the desired transmission frequency—impractically large and too expensive for most applications [1]. An example of this is Very Low Frequency (VLF) broadcasts with frequencies between 3 kHz and 30 kHz. Current VLF transmission facilities include the VLF Transmitter Cutler, shown in Figure 1, operated by the US Navy in Cutler, Maine. The facility requires a staff of over 50 people, and consumes up to 1.8 megawatts of power. An overhead-wire VLF antenna array located at the Jim Creek Naval Radio Station in Washington covers an area of approximately 700 acres.

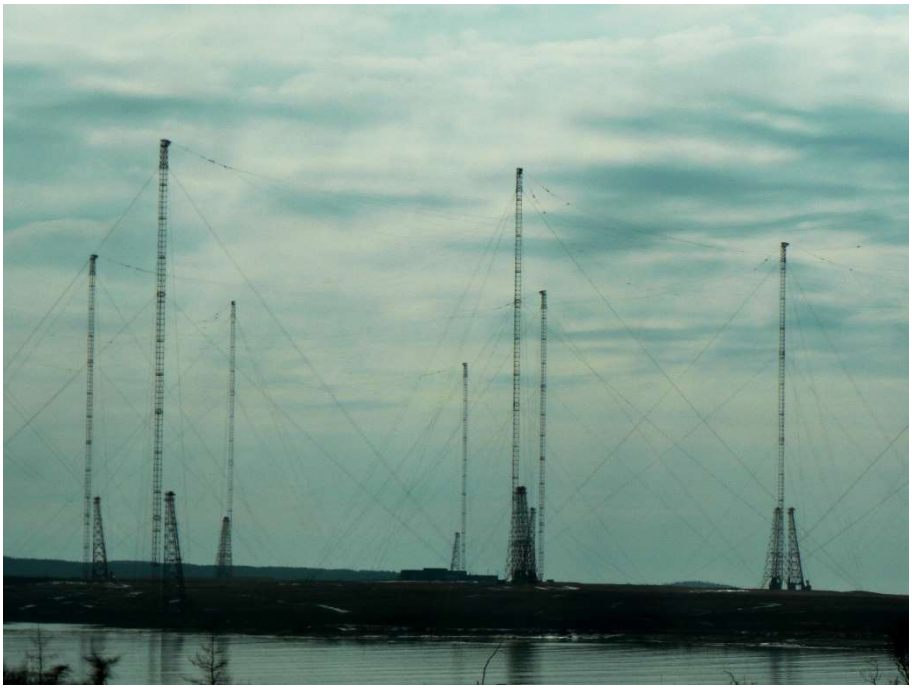

Figure 1 VLF Transmitter Cutler (24 kHz) [2]

Only in the past several years have low-cost alternatives become viable. The recent proliferation of inexpensive, high sensitivity magnetometers has dramatically increased the range of possible applications for magnetic signaling and sensing. At this same time, powerful rare-earth magnets, such as the one shown in Figure 2, show promise for the

development of smaller, lighter, and stronger signaling sources, which can operate at much lower power levels.

Figure 2 Diametrically magnetized neodymium magnet. Taken from [3]

A compact electromagnetic source can be created via the controlled mechanical movement of these rare earth permanent magnets. A simple version is a rotating permanent magnet, which works well at modest frequencies up to about 100 Hz. Mechanically vibrating magnets can operate at much higher frequencies, but do not directly create a reversing field. Preliminary work on a device to induce an oscillating field from a vibrating magnet is discussed later in this investigation.

1.3 Need for Magnetic Telemetry

Buried infrastructure, such as water and sewer pipes, are often located in congested urban areas. Communication with sensors in and around these utilities may be obstructed by asphalt, rebar, concrete, manhole covers, in addition to several feet of earth and soil. The penetrating ability of magnetic signaling makes it well suited to communication with sensors for monitoring these assets. The global yearly market for liquid level monitoring is projected to be $4.7 billion by 2020 with 25% of the expenditures in North America.

Water and wastewater management is expected to be the dominant application sub-segment.

Additional applications of magnetic signaling include communicating with subterranean machines and people in mines, and communication with underwater vehicles and structures. A compact source could also enable advanced mobile active magnetic sensing, potentially of use for counter landmine and counter improvised explosive device (IED) operations. The Department of Defense routinely has calls for novel communication systems for difficult environments. Another possible signaling application relates to NASA's interests in which the plasma produced by a hypersonic reentry vehicle prevents radio communication during descent. Under certain conditions, magnetic waves can penetrate through plasmas.

There is a need for communication with industrial equipment involved in oil drilling and hydraulic fracturing, both of which require signal transmission through challenging environments such as oil, water, or saltwater. Commercial systems currently available for communication with underground drilling and production equipment typically use long, heavy, expensive cables, and require considerable power consumption to operate. There are presently 400,000 oil and gas wells in the United States.

1.4 Need for Infrastructure Monitoring and Leak Detection

Underground water infrastructure is a product of urban growth and history, with many aging components in unknown locations and in unknown condition. The American Society of Civil Engineers (ASCE) gives drinking water and wastewater infrastructure in the United States grades of D and D+, respectively [4]. Leak management in fresh water supply systems is a prime example of the type of challenge faced. Figure 3(a) shows

nonrevenue water loss for four years for a municipal utility in northern Vermont. Water loss has been increasing and approaches 50%. Despite concerted efforts with meter tracking and conventional leak detection equipment, the problem remains largely unresolved. These problems can become exacerbated during and following extreme weather events, particularly when dealing with aging infrastructure. Figure 3(b) shows the number of miles of pipe of different ages currently in use in Burlington, VT [5].

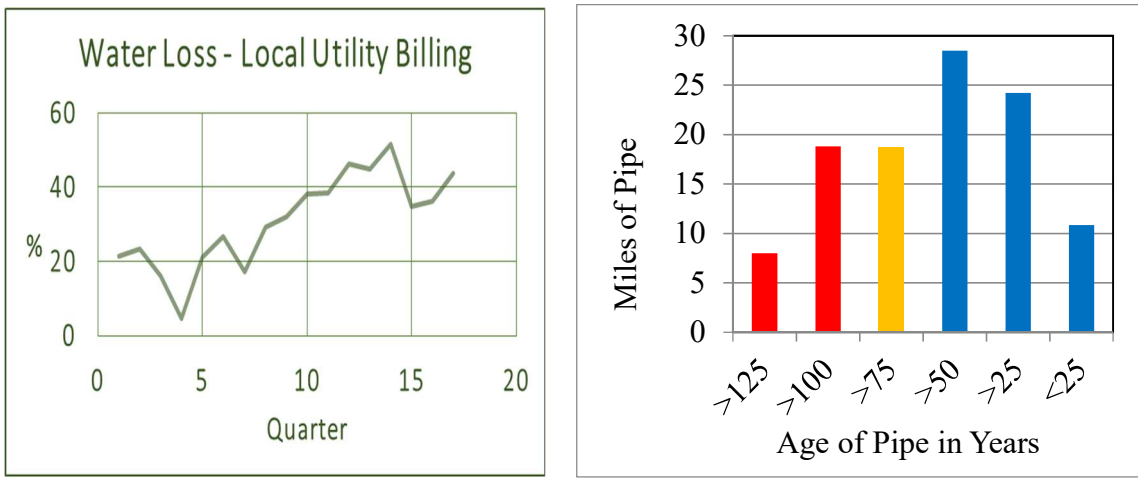

(a) (b)

Figure 3 (a) Nonrevenue water loss in northern Vermont municipal utility, and (b) age of water pipes in Burlington, VT (Courtesy of Burlington Public Works)

1.5 Strategies for Identifying and Monitoring Underground Leaks

The concept is to use multiple sensors and the Internet of Things (IoT) to determine the state of infrastructure. One strategy for leak detection is to use flow meters, like the one shown in Figure 4(a). Flow measurements are taken in a closed section of pipe such that flow differences may be used to indicate the presence of a leak. Another approach is a moisture sensor, as in Figure 4(b). These sensors can monitor for unexpected moisture around a specific pipe section to indicate leakage.

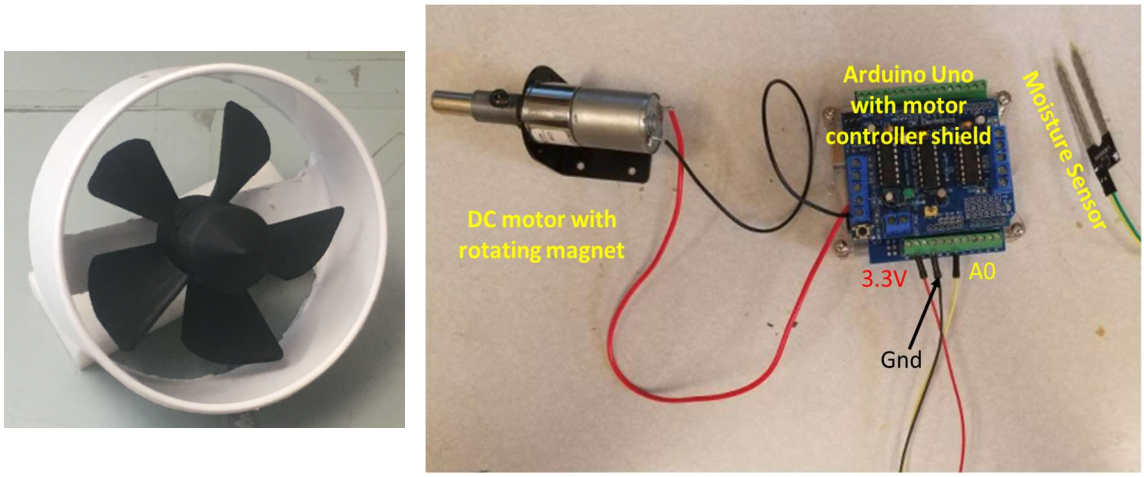

(a) (b)

Figure 4 (a) Flow meter and (b) moisture sensor built for leak detection

1.6 LoRa for IoT

An abbreviation of "Long Range", LoRa is a patented, wireless radio modulation format owned by the company Semtech [6]. It operates in the license-free range of the spectrum, at 868 MHz (European specification) or 915 MHz (North America specification) [7]. It is appealing for IoT purposes due to its low power consumption, low cost, potential for high interoperability between connected devices, and relatively long range (up to 1-10 miles [8]). A Dragino LoRa module (shown in Figure 5(a)), can easily add LoRa capability to an Arduino Uno microcontroller (Figure 5(b)) or Arduino Mega microcontroller (Figure 5(c)).

(a) (b) (c)

Figure 5 (a) Dragino LoRa Long Range Transceiver Shield 915 MHz, taken from [9] (b) Arduino UNO REV3, taken from [10] (c) Arduino MEGA 2560 REV3, taken from [11]

2 RESEARCH TASKS

2.1 Design and Build Self-Powered Magnetic Flow Meter

A device is proposed in which flowing water rotates a propeller causing a magnet to produce an oscillating field. A modular 3D-printed propeller containing a diametric neodymium magnet is shown in the SolidWorks model, Figure 6. The magnet is a cylinder installed inside the nose of the propeller, on the propeller rotation axis.

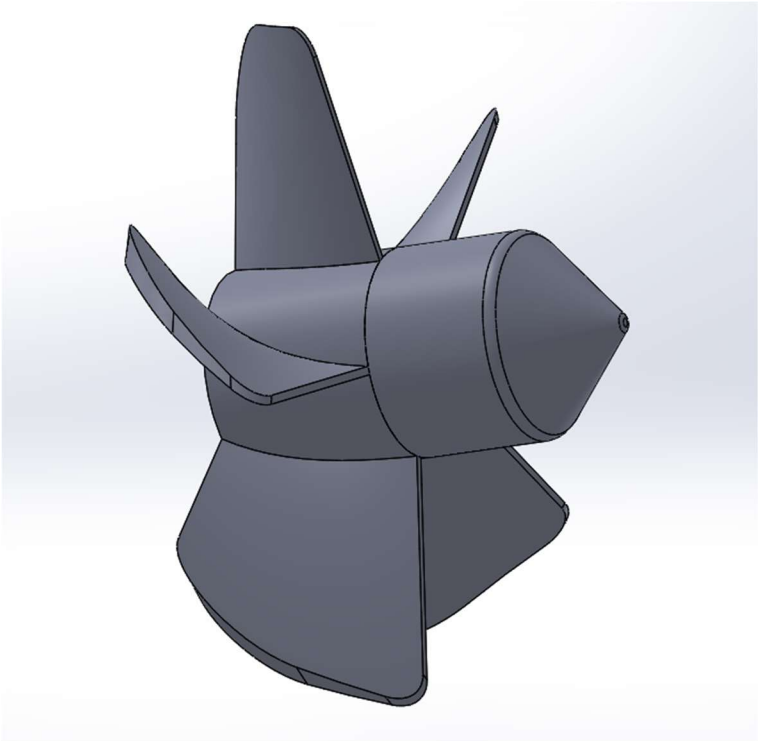

Figure 6 SolidWorks model of rotating magnet flow meter propeller assembly

As the propeller rotates with the flow of the water, so does the diametric magnet. This creates an oscillating magnetic field, which penetrates well through soil, pipes, and debris. Faster-flowing water causes the field to move faster, lending the device it's application as a flow meter. Measurements of the oscillating field provide wireless monitoring of the flow rate, even in subterranean locations inaccessible to traditional

wireless methods. The flow meter itself requires no wires, no power supply, and no physical connection to the LoRa network, unlike conventional flow meters or moisture sensors currently available. The device would not require a data logging pick-up to be installed on the outside of the pipe, opening the possibility for it to be lowered into any section of existing subterranean pipe without excavation. A prototype is shown in Figure 4(a). An HMC5883L magnetometer connected to a remotely installed Arduino Mega microcontroller captures a signal time history, allowing rate of rotation to be determined by Fast Fourier Transform (FFT). The Arduino connects wirelessly to the LoRa network, which transmits over an encrypted channel to fully integrate the magnetic flow meter into the IoT network.

2.2 Achieve LoRa Integration for Magnetic Telemetry Devices

A corollary goal was to design and build a two-stage sensor communication system, in order to network devices with magnetic telemetry. In the first stage, magnetic signaling is used to transmit information from subterranean sensors to surface mounted receivers. These receivers sample the signal using attached magnetometers. A LoRa radio transmits a signal to a LoRa receiver, which uploads data to a server or data-acquisition PC.

2.3 Incorporate Moisture Sensor with Rotating Magnet Telemetry

A battery-operated moisture sensor uses a low-power electric motor to rotate a diametrically magnetized permanent magnet according to the amount of moisture detected. The rate of rotation increases as soil moisture content increases. This rotating magnet produces an oscillating magnetic field, allowing information to be transmitted to an aboveground IoT-networked receiver, without the need for wires. This transmission is

accomplished using less power than a traditional radio-frequency transmitter. The device, designed by Dr. Dylan Burns, is shown in Figure 4(b). Successful functioning and incorporation of this device into the two-stage LoRa network provides evidence for both the viability of magnetic signaling, as well as for the robustness of the built magnetic-LoRa transceiver system.

2.4 Investigate Y-stators for Vibrating Magnet Transmitter

The vibrating magnetic antenna [5] is intended to transmit 3-30 kHz (VLF) frequency-modulated radio signals. It avoids the size challenge of traditional antenna designs by using an array of vibrating, coupled, permanent magnets to generate VLF signals. These permanent magnets move relative to an array of fixed soft magnet stators [12] so that the field reverses direction with each oscillation. Moving a single magnet of large volume far enough to reverse the alignment of its field (relative to a fixed stator) would require a large amount of energy. The solution is to use multiple small oscillating magnets, with the same total volume of magnetic material. Because each of these magnets is small, they do not have to be moved very far to reverse their magnetic fields (relative to a fixed stator), and doing so can take orders-of-magnitude less energy [12].

There are two critical elements of this device which are investigated here. First, in a device with multiple vibrating magnets, their movement must be coupled as to produce a coherent signal. For this purpose, a literature study of coupled oscillations is presented. Second, is the design and behavior of the soft magnet stators, which project the oscillating field. A simulation study of the projected field is performed to verify this phenomenon, for both single, and multiple coupled oscillators.

3 THEORY

3.1 Two Frequency Ranges for Electromagnetic Signaling

There are two relevant bands of EM signal: penetrating magnetic (< 3 kHz) and propagating electromagnetic (3 – 30 kHz) radiation. Subterranean magnetic telemetry devices, such as the rotating magnet flow meter and the rotating magnet moisture sensor, signal use penetrating magnetic radiation. This scenario achieves communication directly with the near-field magnetic field. This magnetic field penetrates well through physical media, and falls-off approximately according to the inverse of the distance cubed. This near-field magnetic field also induces propagation of a far-field electromagnetic signal. This signal transmits long distances, but is quickly attenuated by most solid media. It decreases inversely with distance. The vibrating magnet transmitter operates via this far-field propagating radiation.

3.2 Creating an Oscillating Magnetic Field with a Rotating Magnet

Figure 2 shows a diametrically magnetized neodymium cylinder. Critically, it is polarized north-south across its diameter. Therefore, rotation about its vertical axis causes open field lines to sweep out with the rotation of the cylinder. This creates an alternating oscillating field, as shown in Figure 7.

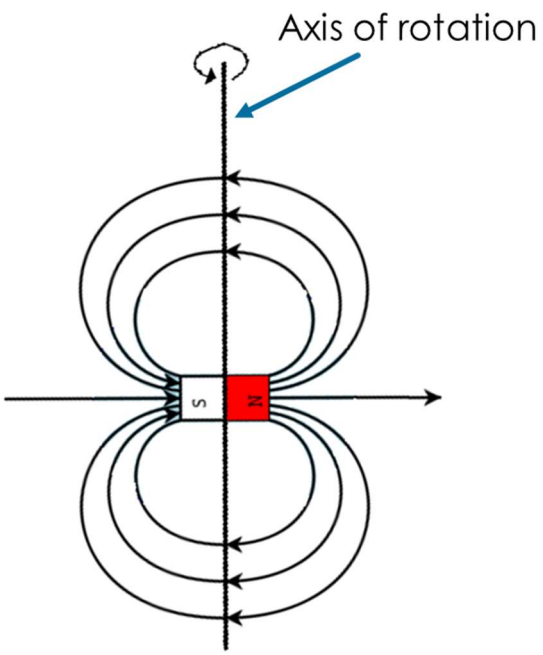

Figure 7 Rotating a diametrically magnetized cylinder about its vertical axis creates an oscillating magnetic field. Modified from [13]

3.3 Creating an Oscillating Magnetic Field with a Vibrating Magnet

Rotating magnets demonstrate the principle of oscillating magnetic fields for low frequencies (up to 300 Hz), but are impractical for the higher frequencies desired for higher-bitrate far-field propagating signaling (300 Hz to 3 kHz). This is because rotating a magnet at 3 kHz (180,000 rpm) is energy intensive, and makes frequency modulation extremely difficult due to the inertia of the system. This makes vibrating magnets more practical than rotating magnets for certain applications. However, as stated before, vibrating magnets do not naturally produce the required reversing magnetic field. A solution is to oscillate the magnet in such a way that the dipole moment reverses. Coupling the vibrating magnets with soft-magnet stators has the potential to produce magnetic field reversal without rotating the magnet. Soft magnetic materials project the magnetic field as the magnet moves side to side. The soft magnetic stators are arranged in a Y configuration.

The soft magnetic material permalloy, a nickel-iron alloy, has high magnetic permeability. The patent literature refers to these devices—in which a soft magnetic material manipulates or switches a magnet's magnetic field—as *supermagnets* [12]. Permalloy is often found in the cores of electric transformers due to the ease of magnetization and minimal hysteretic energy loss associated with field reversal. Figure 8 shows permalloy (dark grey) arranged in the Y-stator configuration.

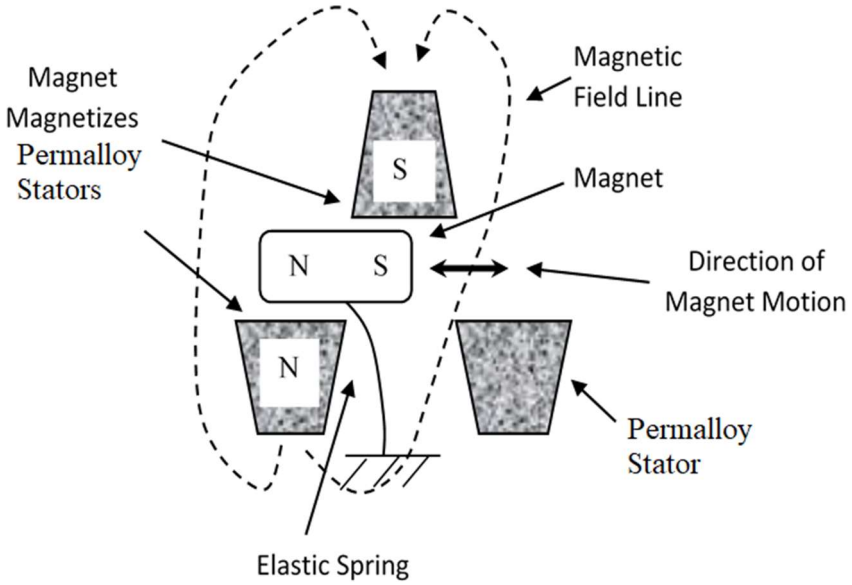

Figure 8 Y-stator configuration, taken from [12]

A single sprung permanent bar magnet oscillator moves back-and-forth, inducing poles in the permalloy stators. Figure 9 shows the direction of the oscillating field changing due to this movement.

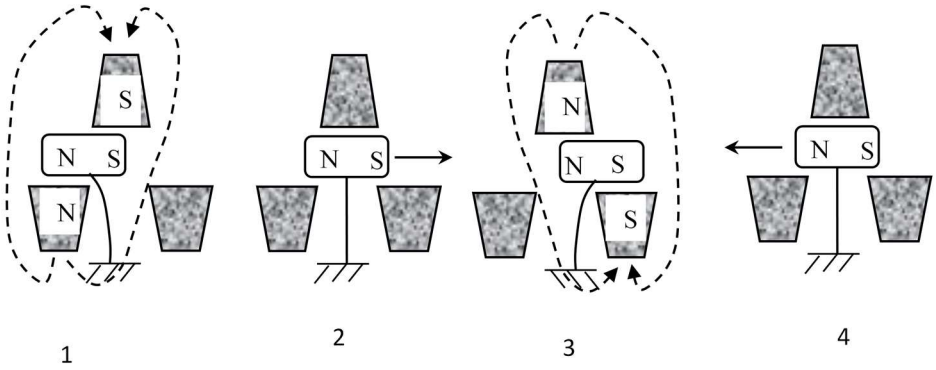

Figure 9 Diagram of oscillating field due to Y-stator, taken from [12]

3.3.1 Resonant and non-Resonant Oscillation

A resonant oscillator vibrates at its natural frequency, ω_n, a low energy state. Changing the natural frequency of a system is a low-energy method of frequency modulation since the frequency of vibration will spontaneously converge to the natural frequency. In contrast, in the case of non-resonant oscillation, an oscillator is forced at a frequency different from its natural frequency. This tends to require more energy, but modulation is often simpler since the vibration frequency can be altered without regard for the mechanics of the system.

3.3.2 Function of Soft Magnet Stators

In addition to projecting an oscillating field, the addition of permalloy soft-magnet stators increases the natural frequency of a freely vibrating permanent magnet oscillator. This is because it takes work to move a magnetic field through the permalloy stators, since doing so forces the field to extend through air. This work increases the magnetic potential energy (and therefore the total potential energy) of the mechano-magnetic system.

$$U = \frac{1}{2}kx^2 \tag{1}$$

An increase in potential energy raises the effective spring constant, k_{eff}. An increase in k_{eff} necessitates an increase in natural frequency, ω_n, according to:

$$\omega_n = \sqrt{\frac{k_{eff}}{m}} \tag{2}$$

where m is the mass of the oscillating element. Observation of this phenomenon is important for confirming our understanding of how the soft-magnet permalloy stators work.

3.3.3 Y-stators and Rotating Magnet Clamps

A familiar variation of the *supermagnet* is the rotating magnet clamp, often used for machine tools and optical bench bases [14]. Its function is analogous to that of the Y-stator configuration, and is detailed in Figure 10. In State 1 the magnet is positioned so that fields are confined to the ferromagnetic materials. This is a low energy position favored by the system: if the clamp is in State 2, the magnetic fields will apply a torque to the magnet rotating it back to State 1. Therefore, an external torque must be applied to rotate the magnet to State 2. State 2 is a high-energy state that projects an amplified magnetic field due to the relative permeability of the ferromagnetic material and the surrounding air—this corresponds to Position 1 and Position 3 shown in Figure 9. If a torsional spring was attached to the magnet in the rotating clamp, the clamp magnet would oscillate in torsional motions between States 1 and 2, thereby projecting a magnetic field.

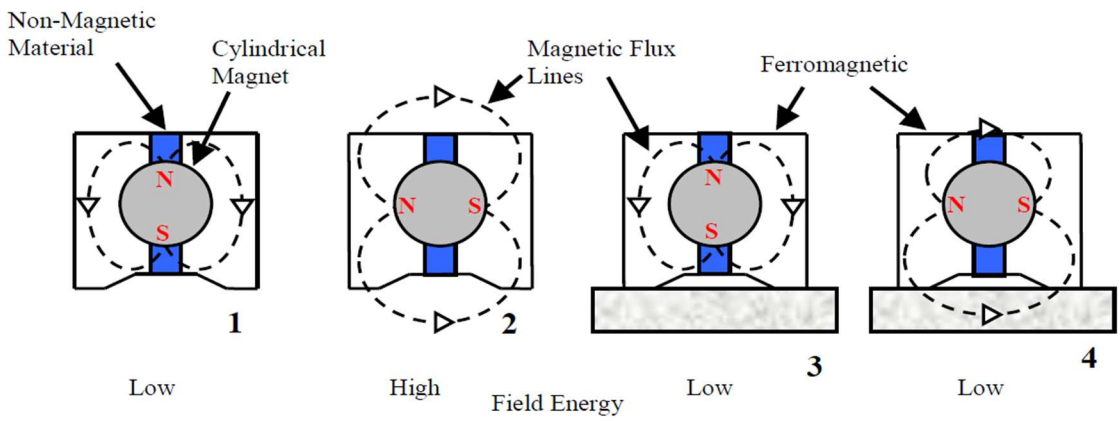

Figure 10 Rotating magnet clamp, taken from [12]

The addition of a ferromagnetic base (grey rectangle below clamps) in State 3 and State 4 alters the magnetic fields lines so that they flow through the ferromagnetic base rather than through the air. This lowers the energy state of State 4, and reduces the amount of torque required to spin the magnet to and from this position. This means that if ferromagnetic material was added to the Y-stator configuration, it would *lower* the natural vibration frequency of the oscillating magnet in a freely vibrating system. Additionally, in State 4 the magnetic field is no longer amplified because it is not being forced through the air. This is also what allows the magnetic clamp to "stick" to a ferromagnetic material—pulling the clamp away from the ferromagnetic base essentially forces it from low-energy State 4, to high-energy State 2. Going from a low energy state to a high energy state takes work.

3.3.4 Increasing the Strength of the Oscillating Magnetic Field

The strength of the projected magnetic field can be increased by vibrating a stronger magnet, or by vibrating a larger volume of magnetic material. Scaling principles favor arrays of small synchronized vibrating magnets rather than a single large magnetic oscillator. Y-stator arrays are shown in Figure 11.

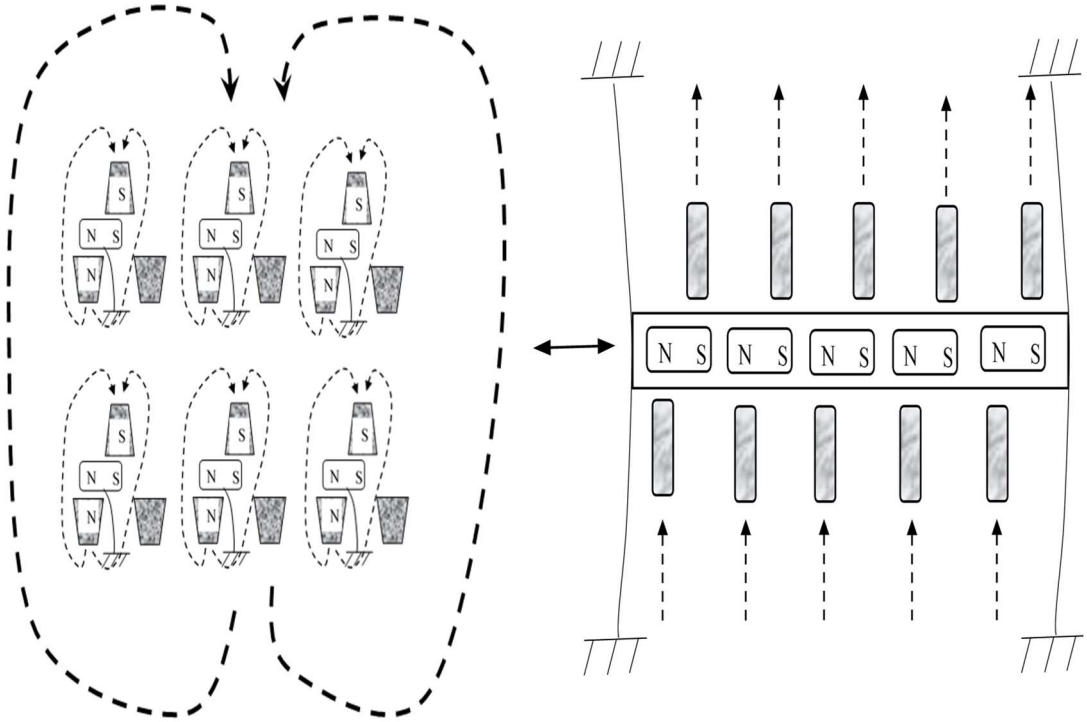

(a) (b)

Figure 11 Multiple oscillators increase the strength of the oscillating magnetic field. Taken from [12]

Kinetic energy requirements reduce (compared to a single large oscillator) when an array of smaller magnets with the same total volume of magnetic material vibrates synchronously. This produces an oscillating magnetic field of equal strength. Because each of the magnets in the array is small, it doesn't have to be moved very far (relative to a fixed Y-stator) to reverse its magnetic field. The scaling rules are as follows: The kinetic energy T of an array of N rectangular bar magnets of density ρ with a length L twice the width and oscillating with an amplitude equal to L at frequency f is:

$$T = \frac{1}{8} N \rho L^5 (2\pi f)^2 \tag{3}$$

The total volume V of the magnets is:

$$V = \frac{NL^3}{4} \tag{4}$$

This leads to an expression of kinetic energy in terms of number of magnets in the array:

$$\frac{T}{V} = T' = \frac{1}{2}\rho L^2(2\pi f)^2 \sim L^2 \quad (5)$$

The kinetic energy requirement increases as a square of the length of an oscillator, so minimizing this length saves significant energy even as the number of oscillators increases.

3.3.5 Changing Resonance to Achieve Frequency Modulation

The vibrating magnetic transmitter encodes information by frequency modulation (FM) accomplished with resonance change. By adjusting a bias current in the soft magnetic stators, the effective magneto-elastic stiffness of each oscillator changes [12]. This changes the natural frequency of each oscillator. In other words, changing the stiffness of the mechano-magnetic spring changes the frequency at which oscillators vibrate, which changes the frequency of the oscillating magnetic signal. The population of oscillators couples their motions due to the strength of the interaction between the individual oscillators.

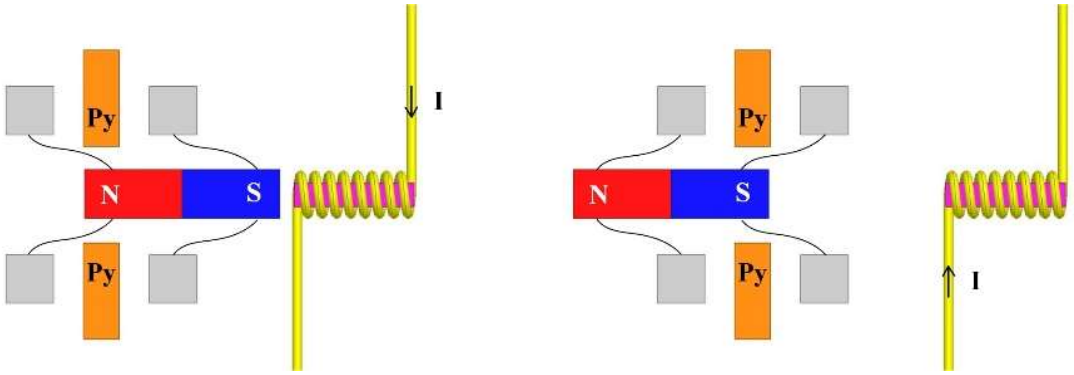

Figure 12 Diagram of simple vibrating oscillator reversing alignment, taken from [12]

Figure 12 shows a simplified Y-stator (essentially half of the previously described Y-stator configuration), which uses a solenoid to stimulate vibration in the permanent-magnet oscillator. The permalloy soft magnet stators are labeled Py.

3.4 Description of Magnetic Fields

A model for the fields generated by moving magnetic dipoles appears in Wangsness 1986 [15]:

$$\vec{B} = -\frac{k^3 m_0}{4\pi\epsilon_0 c^2}\left\{\left[\frac{2i}{(kr)^2} - \frac{2}{(kr)^3}\right] cos\theta\hat{r} + \left[\frac{1}{kr} + \frac{i}{(kr)^2} - \frac{1}{(kr)^3}\right] sin\theta\hat{\theta}\right\} e^{i(kr-\omega t)} \tag{6}$$

where $k = \frac{2\pi}{\lambda}$, m_0 is the dipole moment, and ϵ_0 is the vacuum permittivity constant, $\epsilon_0 \approx 8.854\times10^{-7}\ \frac{C^2}{N*m^2}$ Permittivity is a measure of the ability of a material to resist the formation of an electric field within it. In the near field, the magnetic field $\vec{B}$ is dominated by denominator terms with $(kr)^3$, and:

$$\vec{B} \approx \frac{k^3 m_0}{4\pi\epsilon_0 c^2}\left[\frac{2}{(kr)^3} cos\theta\hat{r} + \frac{1}{(kr)^3} sin\theta\hat{\theta}\right] e^{i(kr-\omega t)} \tag{7}$$

In the far field, the magnetic field $\vec{B}$ is dominated by denominator terms with (kr), and:

$$\vec{B} \approx -\frac{k^2 m_0}{4\pi\epsilon_0 c^2}\frac{1}{r} sin\theta\hat{\theta} e^{i(kr-\omega t)} \tag{8}$$

3.5 Magnetic Field Detection

3.5.1 Hall Effect

The Hall effect is the process by which a voltage difference forms across an electrical conductor, perpendicular to the flow of a current, as determined by an applied magnetic field perpendicular to both the conductor and the current flow. The voltage difference, called the Hall voltage, forms because the charge carriers (typically electrons, electron holes, or ions) in the current have their paths altered by the Lorentz force—a

combination of electric and magnetic forces [16]. Figure 13(a) shows the sensor when no magnetic field is applied: there is no voltage gradient across the electrical conductor. In Figure 13(b), a magnetic field has been applied, creating a voltage difference proportional to the strength of the magnetic field. In this way, the strength of a magnetic field can be determined by measuring the voltage difference.

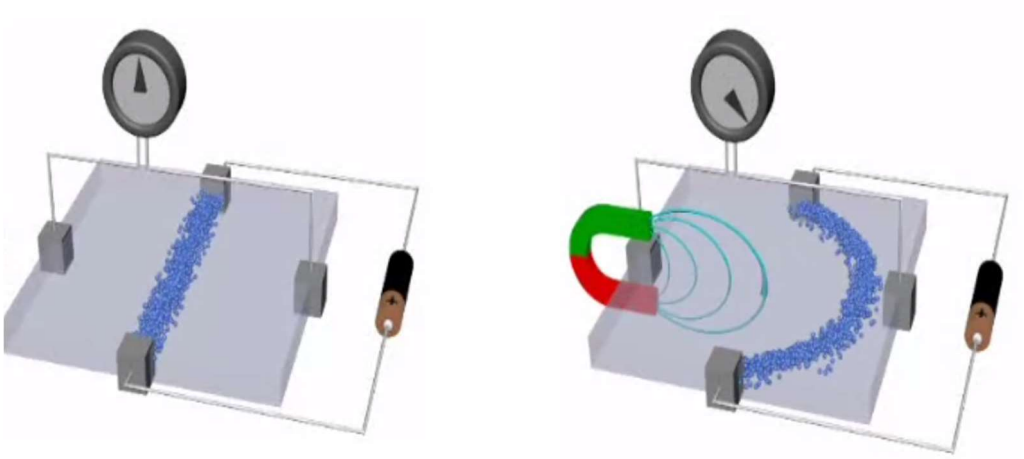

(a) (b)

Figure 13 The Hall Effect, taken from [17]

3.5.2 Quantum Hall Effect

The quantum Hall effect can be thought of as the application of the Hall effect to systems of electrons at low temperatures, subjected to a strong magnetic field [18]. Notably, it is found that in these conditions the Hall conductance takes on values which are exactly quantized. Hall conductance is defined by:

$$\sigma = \frac{I}{V_H} \tag{9}$$

where I is the current, and V_H is the Hall voltage.

3.5.3 Magnetoresistive Sensors

Magnetoresistance is the property wherein a material changes its directional electrical resistance based on the application of an external magnetic field [19].

Magnetoresistive sensors are designed to be small and to operate with low power consumption [20], without the need to operate at low temperatures.

3.5.4 SERF Atomic Magnetometer

A spin exchange relaxation-free magnetometer functions by measuring the precession frequency of certain gaseous alkali atoms, such as potassium, in a magnetic field [21]. Figure 14 details the principle of operation. The magnetic moment of the alkali atoms causes them to precess around an external magnetic field. Circularly polarized light produced by a diode laser aligns the magnetic moments of the individual atoms in the same direction, producing a coherent moment [21]. A linearly-polarized orthogonal probe light is optically rotated by the coherent precession, thereby giving an extremely sensitive vector measurement of the three directional components of the external magnetic field.

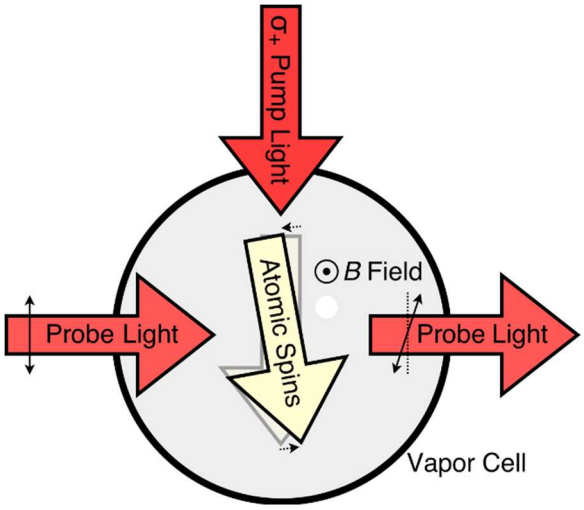

Figure 14 Principle of operation of SERF atomic magnetometer. Taken from [22]

3.5.5 Superconducting Quantum Interference Device (SQUID)

A disadvantage of atomic magnetometers is that their high sensitivity requires that they be operated only in very-weak or near-zero magnetic fields. Superconducting quantum interference device (SQUID) magnetometers do not suffer from this limitation, and can be

nearly as sensitive [23]. They function using superconducting loops containing Josephson tunnel junctions [23]. A disadvantage, however, is that Josephson tunnel junctions require cryogenic refrigeration.

3.6 Data Analysis for Oscillating Fields

Magnetometers allow acquisition of magnetic field strength over time. Figure 15(a) shows a three-axis time history of an oscillating magnetic field. A Fourier Transform converts the time-domain oscillating field to frequency domain, and allows for determination of the frequency of the oscillating field, as shown in Figure 15(b).

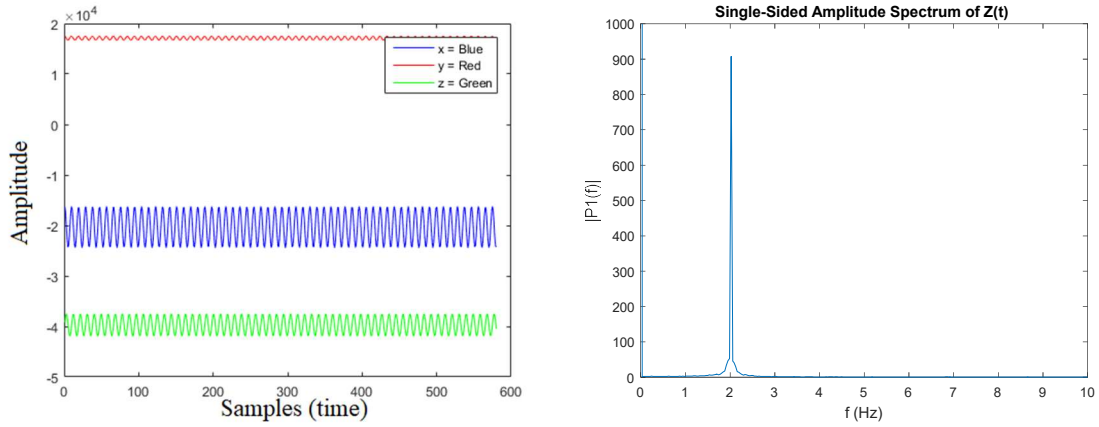

(a) (b)

Figure 15 (a) Time-history of X,Y,Z-axis oscillating fields, and (b) frequency-domain spectra of Z-axis showing major feature at 2 Hz.

4 PRELIMINARY EXPERIMENTS

4.1 Signal Generation with Rotating Magnet

Preliminary experiments were conducted to verify that detectable signals can be generated from both rotating and vibrating magnets. All rotating magnet tests in this inquiry use the same specification magnet: a diametrically magnetized neodymium cylinder with a diameter of ¼ inches, and a length of 1 inch. Residual magnetic flux density is approximately equal to 13,200 gauss, with a pull force of roughly 14 lbs [24, 25]. This magnet was inserted into a drill press chuck and rotated at 10 Hz, as shown in Figure 16(a). A circular RF probe was connected to a spectrum analyzer to measure the magnetic frequency spectrum, shown in Figure 16(b). A feature is clearly visible at 10 Hz.

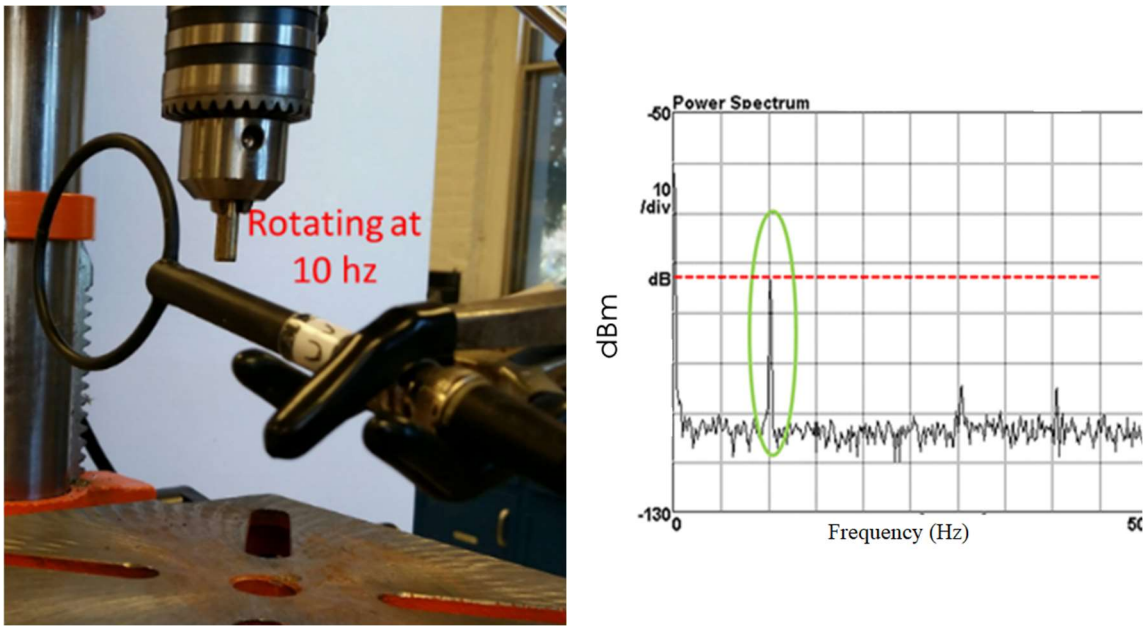

(a) (b)

Figure 16 Signal generation with rotating magnet

4.2 Signal Generation with Vibrating Magnet

Permanent magnets were mounted on a jigsaw blade to evaluate the ability of permalloy soft-magnet Y-stators to project a signal, as shown in Figure 17. The permalloy

was taken from the core of an electric transformer. An RF probe connected to a spectrum analyzer was used to measure the signal. The jigsaw is shown to oscillate at 22.3 Hz. The oscillating magnetic field induces an electric current in the probe's coil, per Ampere's circuital law.

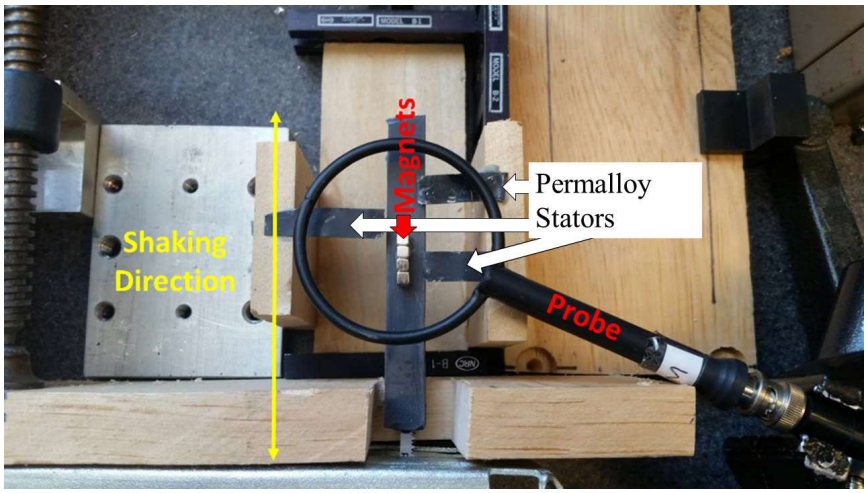

Figure 17 Signal generation with vibrating magnet and Y-stator

A comparison of Figure 18(a) with Figure 18(b) shows the inclusion of the Y-stators increased frequency-domain feature strength by approximately 150%.

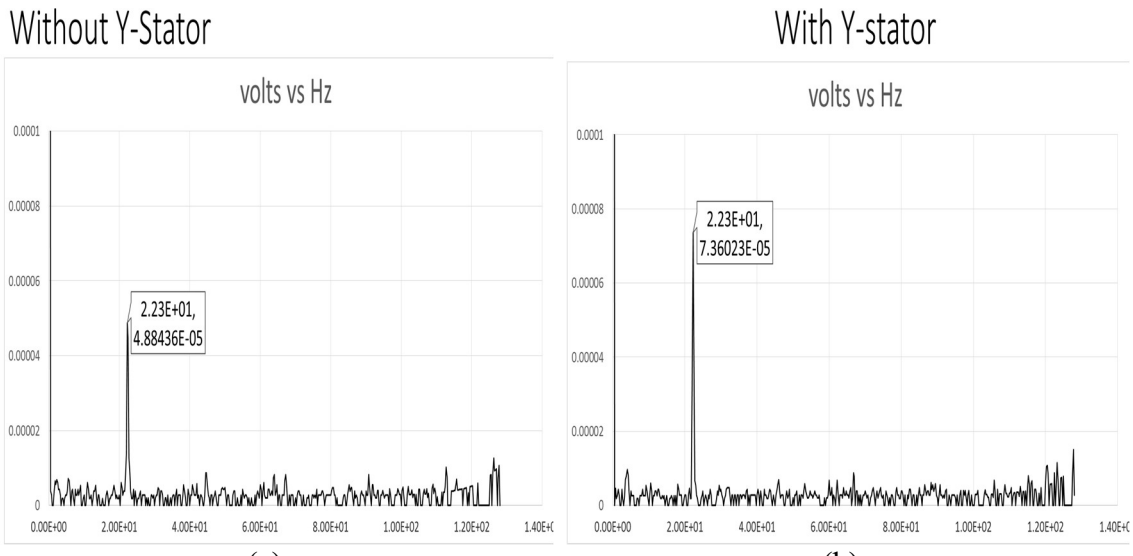

(a) (b)

Figure 18 Y-stator increases signal amplitude

4.3 Permalloy Stators Increase Natural Frequency

An accelerometer was used to measure the vibration frequency of a metal plate suspended by guitar strings, in order see if the addition of permalloy soft-magnet stators causes the expected increase in the natural frequency of a freely vibrating system. Figure 19(a) shows a birds-eye view of the setup, with the permalloy stators located out-of-the-way at the bottom of the image. Without interaction with the stators, the system recorded a natural frequency of 8.25 Hz, shown in Figure 19(b).

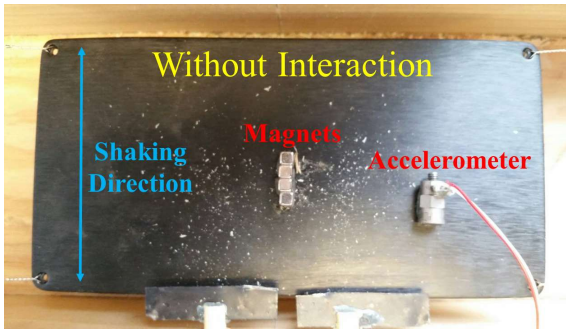

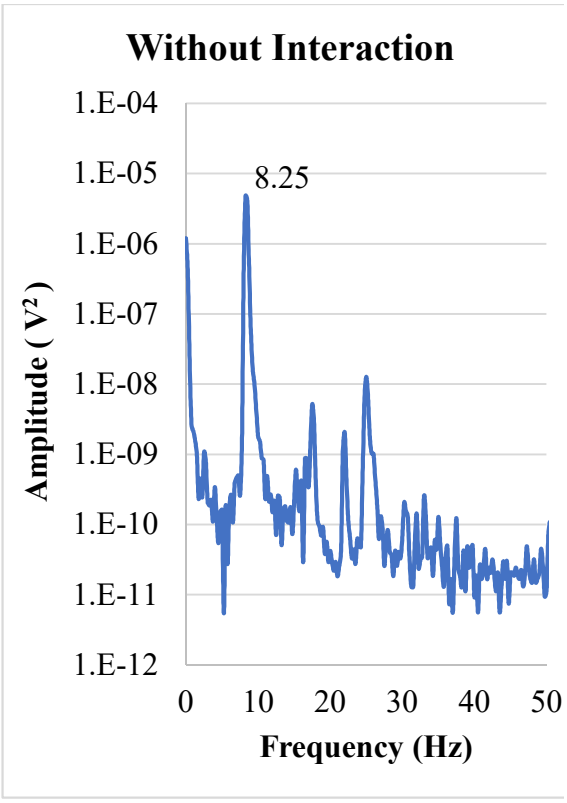

(a) (b)

Figure 19 Natural frequency without permalloy stators

Figure 20(a) shows the same experimental setup, except with the placement of the permalloy stators in a half-Y configuration. Figure 20(b) shows that this addition has increased the natural frequency to 10.0 Hz. The narrowness of this peak is indicative of a low-damping scenario. The decrease in the amplitude of the feature (compared to the

feature in Figure 19(b)) is likely due to slightly unequal input forces being used to initiate free vibration.

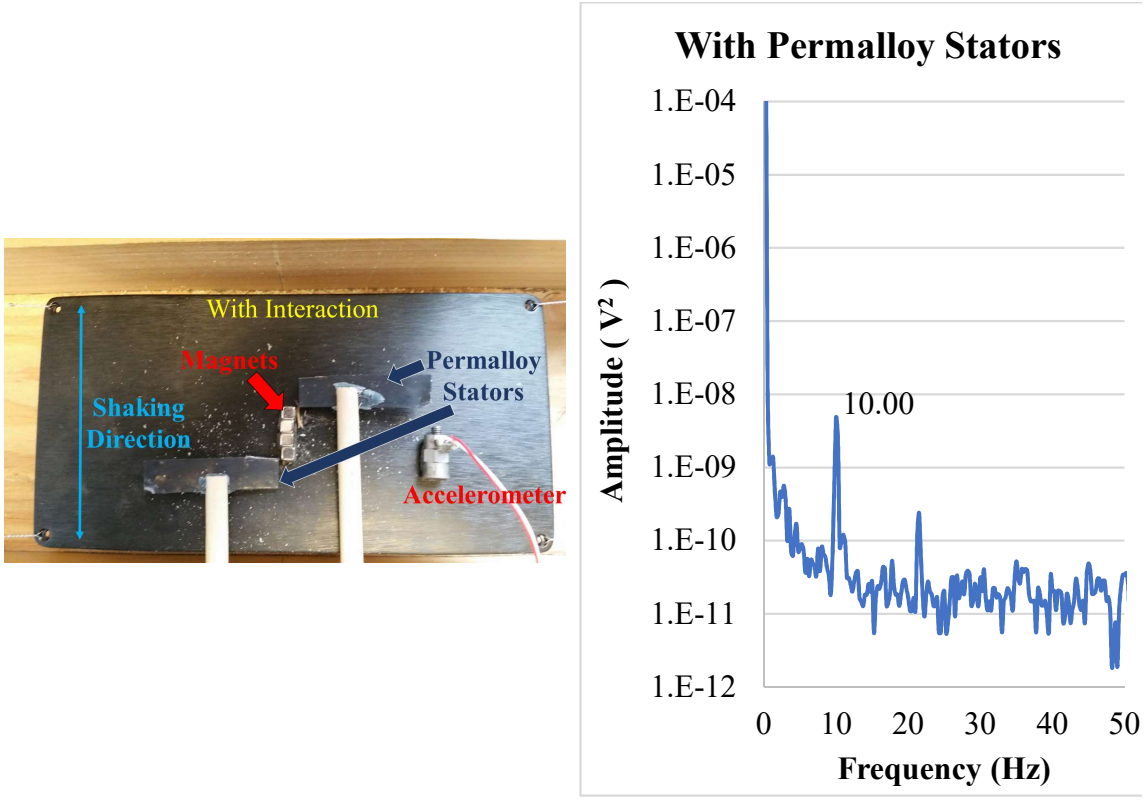

Figure 20 Natural frequency with permalloy stators

4.4 Propagation of Magnetic Signal through Media

The ability of a magnetic field to transmit frequency information over distances, and through obstacles, must be well understood in order to use magnetic signaling for subterranean sensing. Tests were performed to measure experimentally how a rotating magnetic field might be attenuated by distance, and by different obstructing materials. A diametrically magnetized neodymium cylinder was rotated by a servo motor at approximately 2 Hz to create a rotating field. The servo motor, power supply, and magnet were sealed in a 7” by 7” waterproof housing, which was weighted with rocks and gravel. The waterproof housing containing the rotating magnet was placed in a plastic storage bin.

A Honeywell HMR2300 3-axis Hall effect magnetometer was mounted approximately 18 inches above the rotating magnet. It measured the magnetic field strength at various distances, as measured horizontally from the rotating magnet. The magnetometer orientation was aligned with the front of the magnetometer (the X-axis sensor) pointing toward the spinning magnet. Tests were performed with the plastic storage bin empty (except for the sealed housing), filled with 12" of water, filled with 12" of soil, and empty but with an additional thin steel pipe surrounding the waterproof housing. An additional test was also performed without the plastic bin or the waterproof housing, with the servo motor and magnet instead sealed inside an aluminum case.

Signal strength versus time was recorded for each axis (20 samples per second). The HMR2300 uses three Hall sensors, one for each of the X, Y, and Z directions. A Fourier Transform converts the information to the frequency domain, and allows for determination of the frequency of the spinning magnet. A stronger, more stable signal will creature a larger primary Fourier feature. The amplitude of the primary Fourier frequency feature determined the strength of the signal. Figure 21 shows a combination of the strength of the X, Y, Z frequency features, for the different media types. Figure 22, Figure 23, and Figure 24 show the individual X, Y, and Z features, respectively. In all of Figure 21 through Figure 24, the vertical axis uses a logarithmic scale.

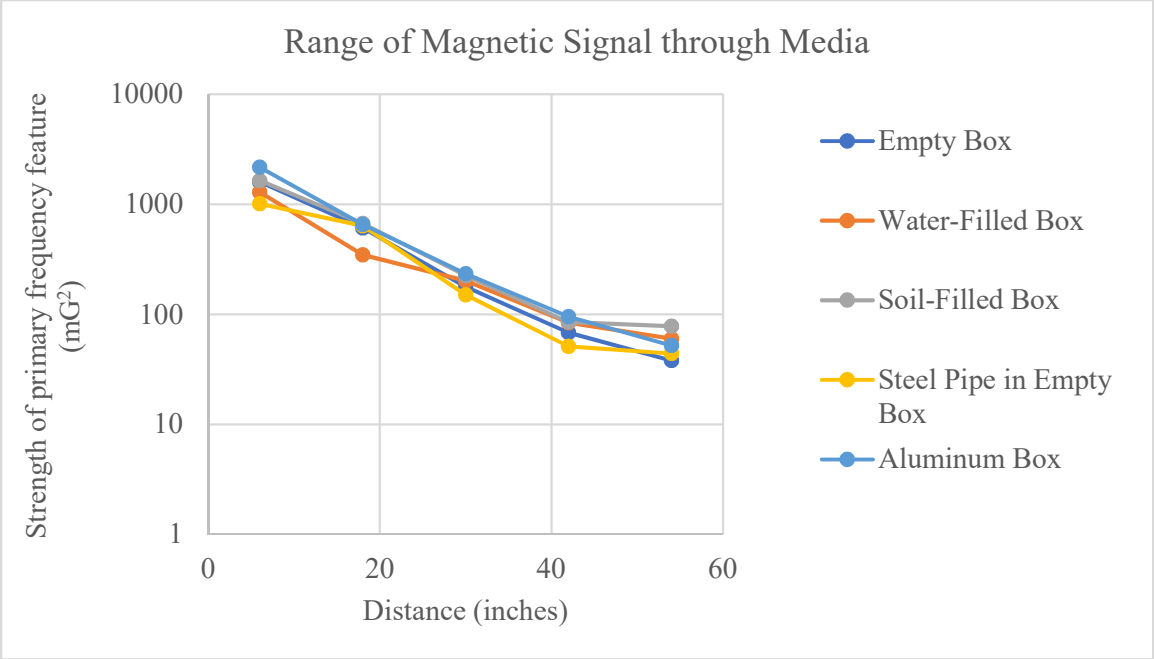

Figure 21 Combined (X, Y, Z) strength of primary frequency feature versus distance, with rotating magnet source at ~2 Hz. (HMR2300)

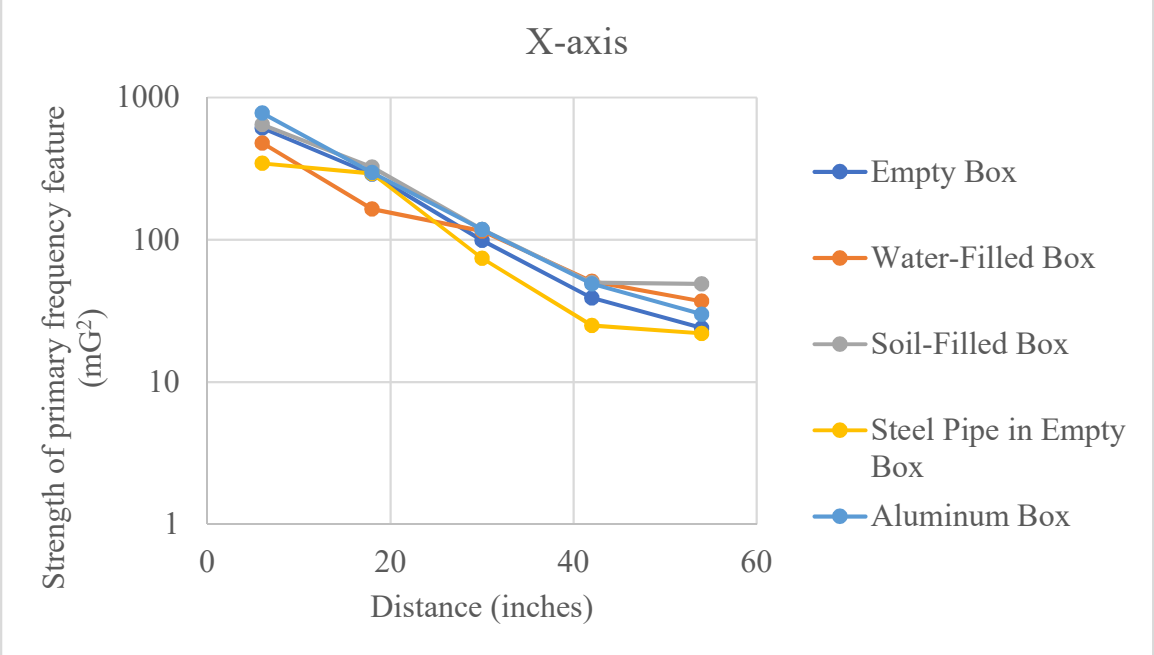

Figure 22 Strength of primary frequency feature (X-axis) versus distance

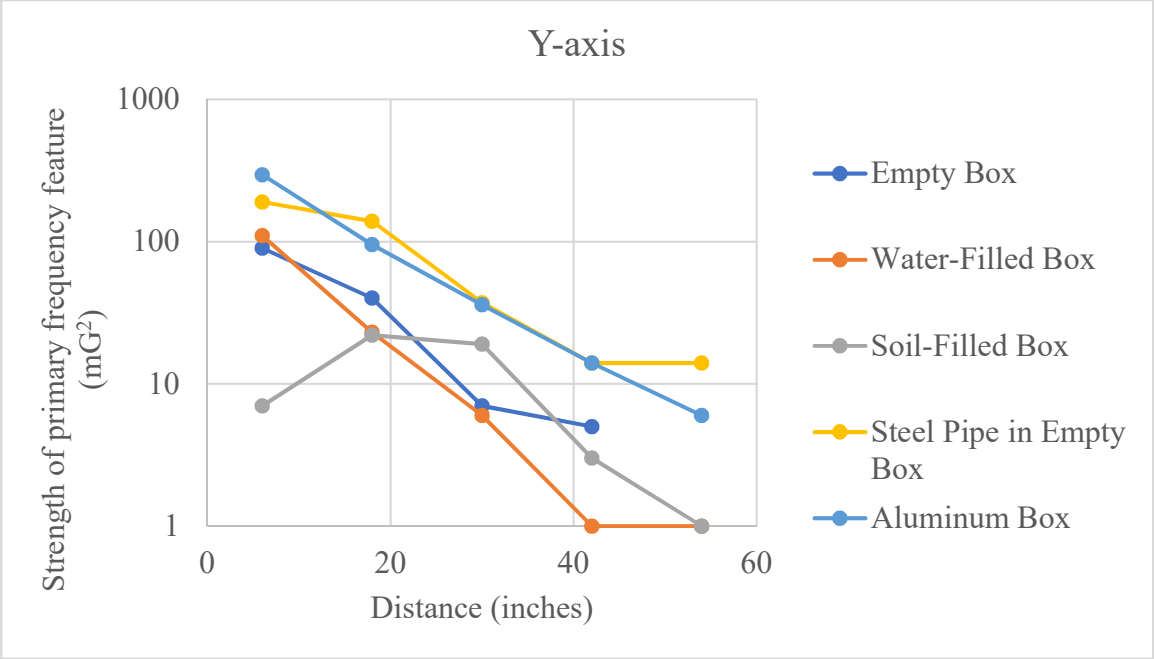

Figure 23 Strength of primary frequency feature (Y-axis) versus distance

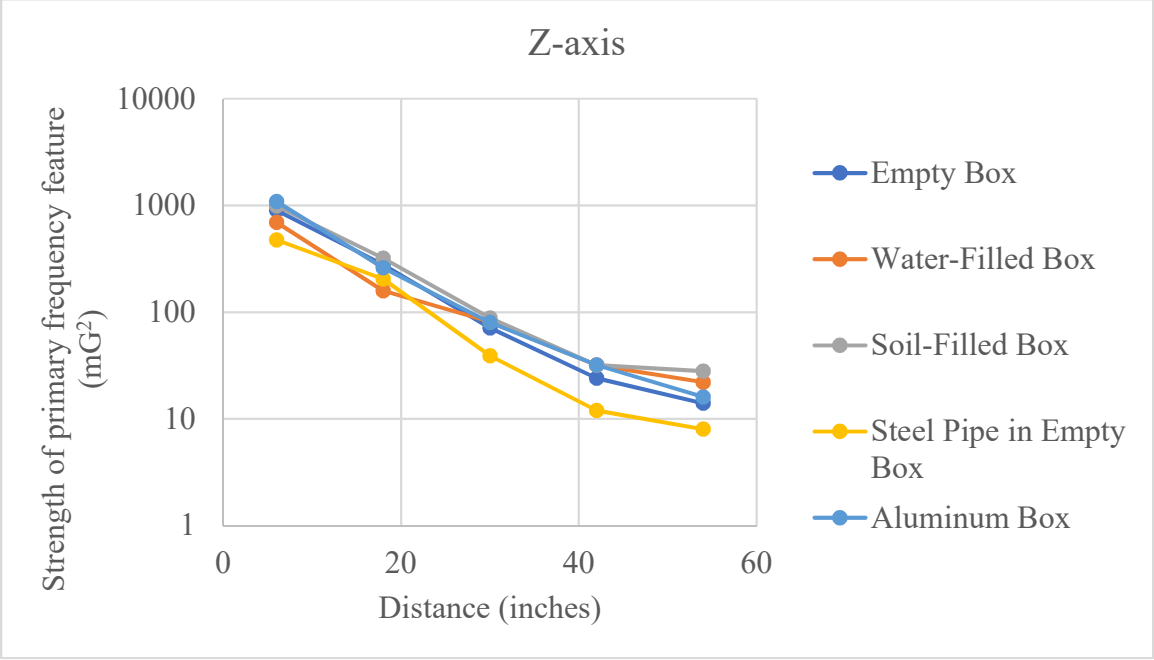

Figure 24 Strength of primary frequency feature (Z-axis) versus distance

Material obstacles, particularly the thin steel pipe, caused up to a 2-3 fold decease in the strength of the frequency feature. The combined strength of the three (X, Y, Z) primary frequency features remained at least 10x above the noise floor in all test variations.

Metal and natural obstacles had a less-than-expected impact on signal transmission, and signal range appears adequate for many infrastructure sensing applications.

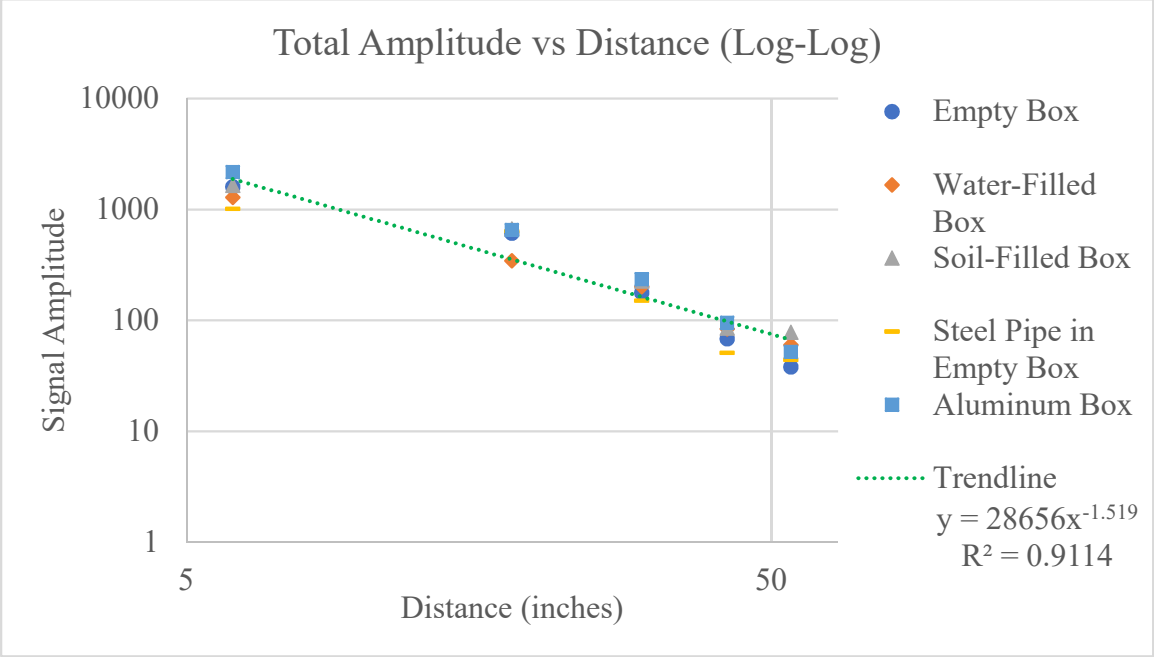

Figure 25 Combined (X, Y, Z) strength of primary frequency feature versus distance, with rotating magnet source at ~2 Hz. Plotted on log-log scale with trendline

Figure 25 reproduces the data shown in Figure 21 on a log-log scale. A trendline for all test scenarios at all test distances is shown. This trendline has a relatively high R^2 value of 0.9114, which demonstrates that this trendline has good fit for signal propagation regardless of the type of obstructing media. This indicates that the magnetic signal propagates almost equally well through all tested obstructions. Furthermore, open-air tests show that the signal slightly overperforms compared to the theoretical 1/r^3 near-field signal strength drop-off, shown in Figure 26. This may be due to a combination of near and far field effects.

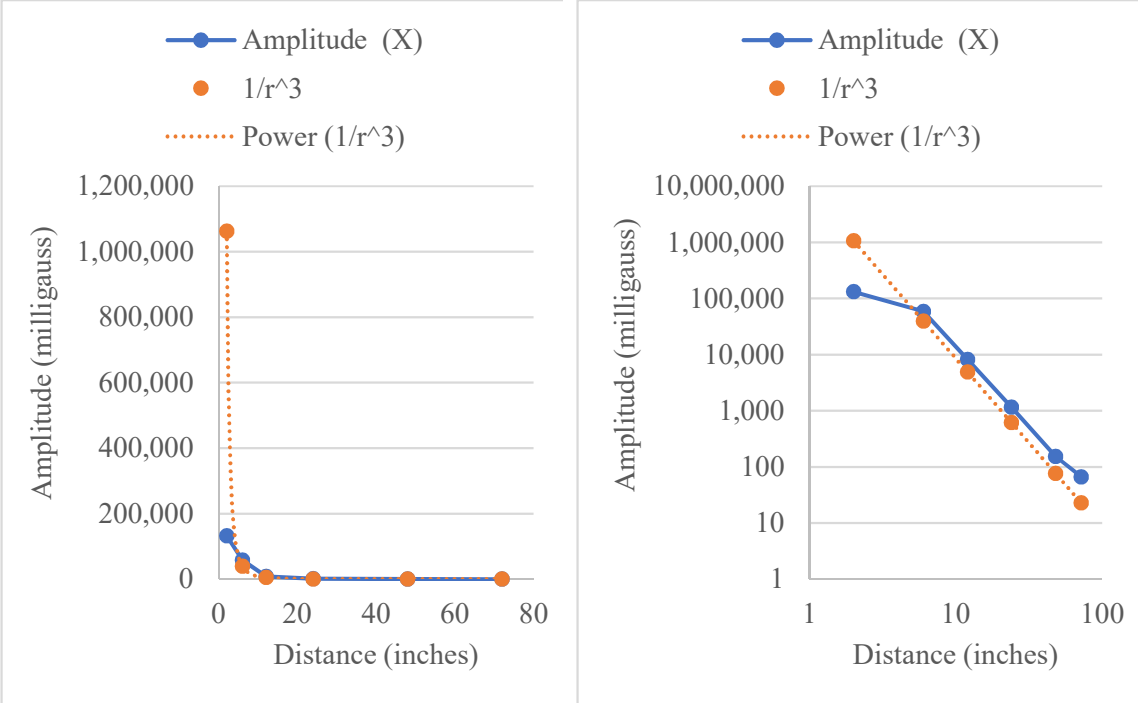

(a) (b)

Figure 26 Comparison of experimentally observed (X-axis) and theoretical near-field values in air using HMR2300 magnetometer. (a) shows results using base-10, while (b) uses a log-log scale.

4.5 Long-Range Laboratory Tests with HMR2300

The same diametrically magnetized neodymium cylinder was again rotated at approximately 2 Hz. The HMR2300 magnetometer was pointed at side of the rotating magnet at a distance of 25 feet, across the Perkins 103 laboratory. Physical obstacles such as cabinets and the sandbox were present, and other instruments in the lab were powered-on. Figure 27(a) shows the small, but present detected frequency feature at 2 Hz. Figure 27(b) shows the same spectrum processed using the MATLAB pwelch function, to implement Welch averaging. This function takes the entire Z-axis data set and breaks it into smaller segments of a specified length, in this case 512 data points. It then computes as many spectra as there are segments, and averages them to yield a single smoother

spectrum with less variance [26]. This processing enhances the 2 Hz signal feature relative to the noise.

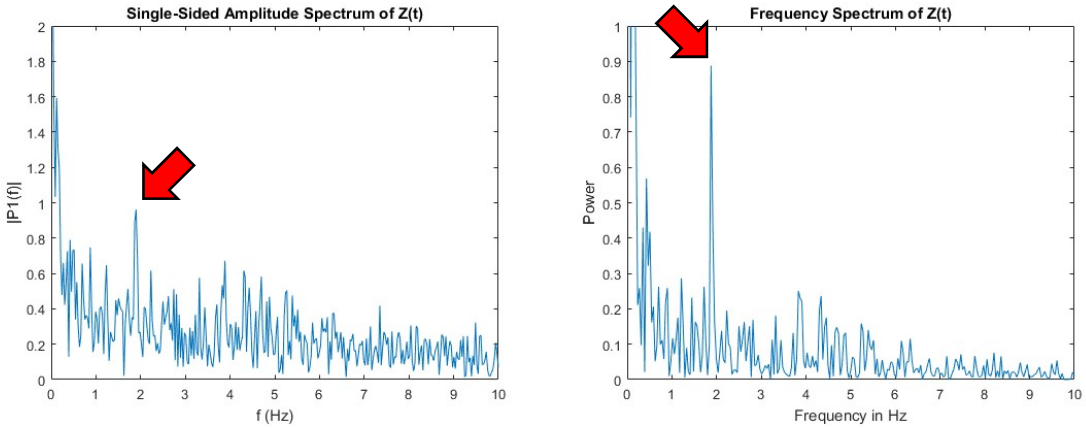

(a) (b)

Figure 27 (a) Frequency feature detected at 2 Hz, at indoor range of 25 feet. (b) The same spectrum smoothed using MATLAB pwelch function, yielding an enhanced feature.

The test was then repeated with the oscillating sourced moved closer, to approximately 15 feet. Figure 28(a) shows the spectrum when the source was turned-off, i.e. background noise. Figure 28(b) shows a prominent 2 Hz feature produced when the servo rotates the magnet.

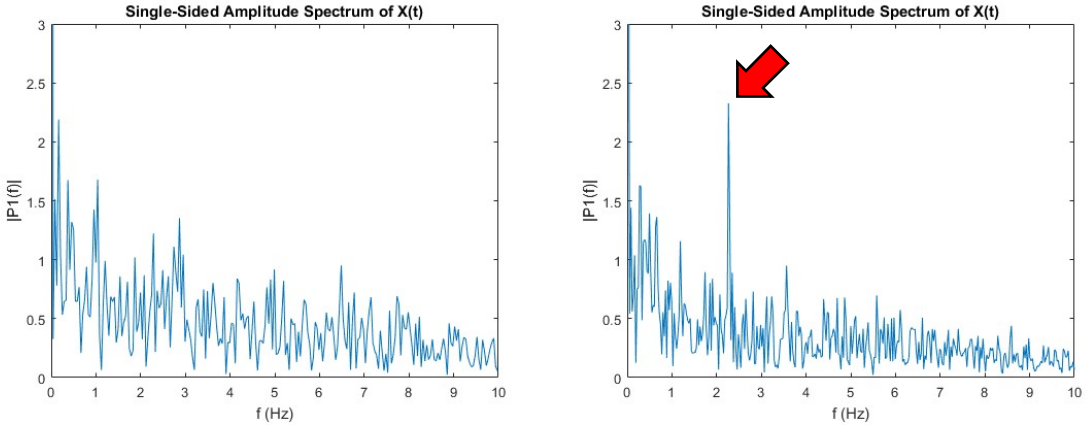

(a) (b)

Figure 28 Distance test at 15 feet: (a) background noise, and (b) magnet rotating at 2 Hz

4.6 Rotating Magnet in Drain Pipe at Sheraton Hotel

The ability of an oscillating magnetic signal to transmit out of a corrugated plastic drain pipe was tested at a drain near the front entrance of the Sheraton Hotel in South Burlington, Vermont. The HMR2300 magnetometer was approximately 7-8 feet away from the rotating magnet source (straight-line distance). The soil/rock/gravel layer above the pipe was approximately 4 feet thick.

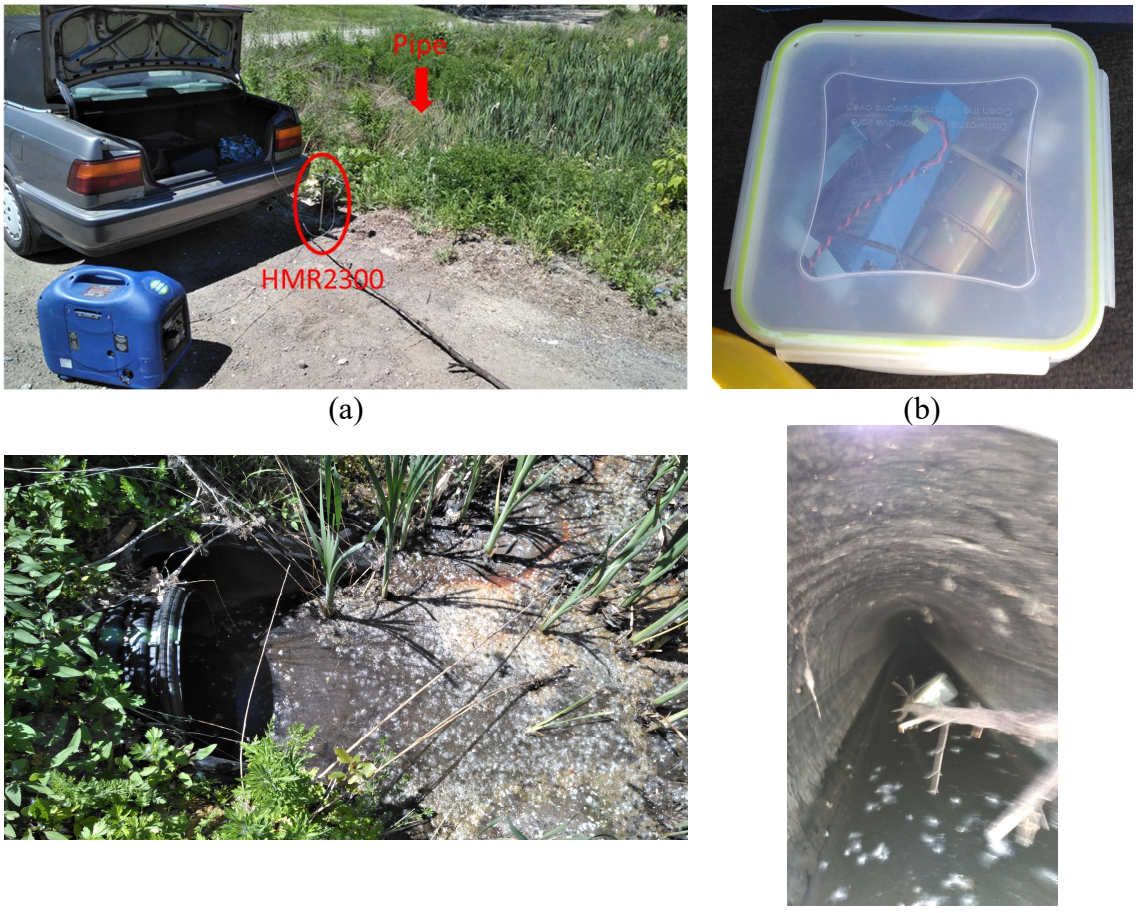

Figure 29 (a) Site and test equipment. HMR2300 magnetometer indicated, (b) rotating magnet in sealed enclosure, (c) mouth of corrugated plastic drain pipe, and (d) looking inside the pipe, with rotating magnet source attached to stick.

The top row of Figure 30 shows the X, Y, and Z frequency spectra after data were collected for 38.2 seconds. The X and Z sensors easily detected the 2 Hz signal. An identical setup was used for the bottom row of Figure 30, except data was acquired for only 18.15 seconds—meaning less than half as many data points were collected. Because the

default sampling rate of the HMR2300 is only 20 samples per second, this had an adverse effect on signal detection: only the Z-axis sensor was able to resolve the 2 Hz signal. Still, this test demonstrates successful magnetic telemetry out of an actual storm drain.

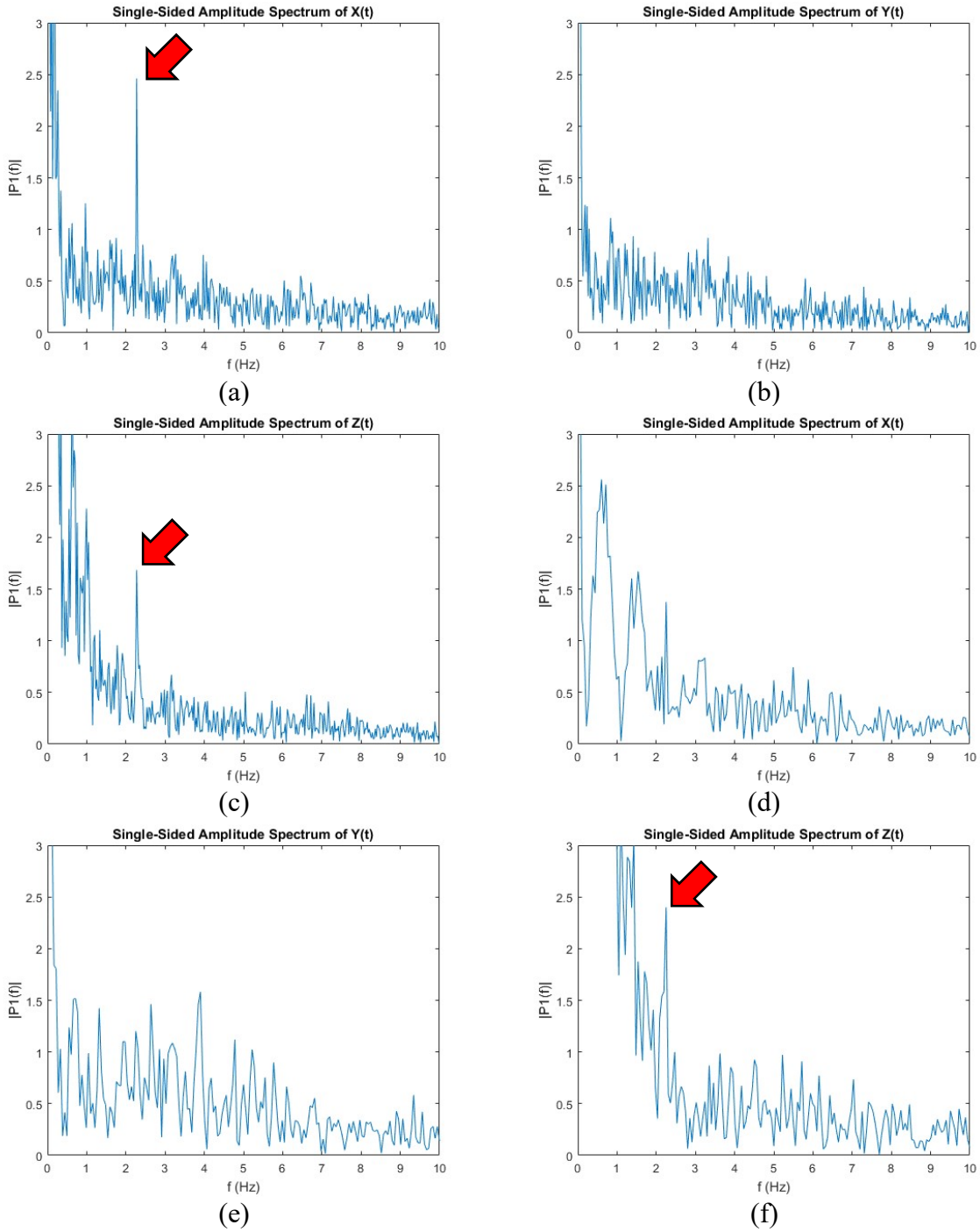

Figure 30 (a) X, (b) Y, and (c) Z frequency spectra after 38.2 second data acquisition. (d), (e), and (f) are the frequency spectra after an 18.15 second acquisition.

5 LITERATURE STUDY OF COUPLED OSCILLATIONS

5.1 Purpose of Study and Introduction to Coupled Oscillations

Properly coupling the oscillations of ganged Y-stators is critical for the operation of sophisticated versions of the vibrating magnetic antenna. The phenomenon of coupled oscillations was first recorded in 1665 by the Dutch physicist Christiaan Huygens [27]. Huygens—the inventor of the pendulum clock—noticed that the pendulums of two clocks hanging on the same wall would always synchronize. However, if the clocks were moved to opposite sides of a room, their movements would decouple. Huygens proposed that the clocks must be able to influence one-another at short distance, through some sort of minute vibration or imperceptible air movement [27]. This observation is the first recorded case of a great many examples of synchronous oscillators in the natural world.

It is appropriate to define what, exactly, is meant by an oscillator. An oscillator is an object or quantity with a property that varies in time about a central value [28]. A classic physical example of an oscillatory system is an undamped spring-mass system, as shown in Figure 31. The natural frequency, ω_n, of the system is given by:

$$\omega_n = \sqrt{\frac{k}{m}} \tag{10}$$

where k is the spring constant in units of N/m, and m is the mass of the object in kg. The significance of Huygens' observation is that two systems with slightly different natural frequencies may couple to the same frequency, given sufficient interaction forces.

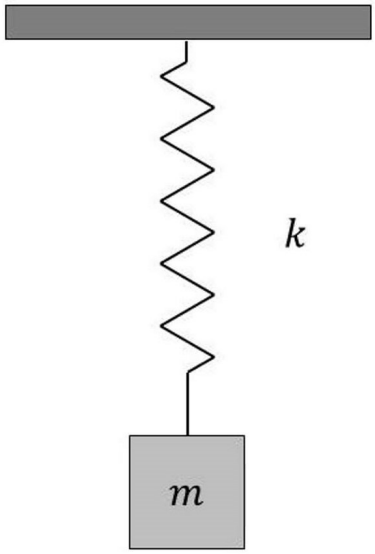

Figure 31 Undamped spring-mass oscillatory system. Taken from [29]

Coupled oscillations are not confined to the realm of simple mechanical systems, however. Other engineering examples include coupled chemical reactions, synchronized laser arrays, nanomechanical oscillators, and Josephson junctions [30]. Furthermore, coupled oscillators are present in many biologic systems [27], such as pacemaker cells in the heart [31], neurons in the brain [32], glycolytic synchrony in yeast cell suspensions, pancreatic beta cells, menstrual synchrony among women [33], synchronous applause of audiences [30], synchronously flashing Southeast Asian fireflies, and the chorusing of crickets [33].

A mathematically rigorous description of these phenomenon has only been developed in the last several decades. The primary motivation has been to answer the basic question of how multiple interacting oscillators can couple themselves, despite variations in the natural frequencies of the individuals [32]. In short, when the range of natural frequencies in a population of oscillators is large comparted to the coupling force, each oscillator runs at its own natural frequency, rather than coupling. If the range of natural

frequencies decreases sufficiently, or if the relative coupling increases beyond a critical measure, a portion of the population of oscillators spontaneously couples [33].

5.2 Theory of Coupled Oscillations

The dynamics of large systems of coupled oscillators have been studied since Huygens' first writings in 1665. A breakthrough came in 1967 when Winfree [34] considered the special attributes of biological systems. Previously, most investigations had focused on the idealized physics problem, in which oscillators are identical and conserve energy [33]. An example of this is an idealization of the pendulum from one of Huygens' clocks. While the period of the motion of the pendulum is always the same, the amplitude of its motion depends on the height from which the pendulum is released. This is not what Winfree observed in biological systems, however. He noted that biological systems tend to not only have characteristic frequency, but also, amplitude [27]. Such systems are known as limit-cycle oscillators. This type of system incorporates a mechanism to dissipate too-large oscillations, and the ability to add energy to increase the amplitude of too-small oscillations [27]. Furthermore, biological oscillators are never identical due to the natural variability of genetic factors [33]. These features of biological systems allowed Winfree to make two important assumptions:

i. A collection of oscillators will have a random distribution of natural frequencies, but may be considered identical by all other metrics [33].
ii. Each oscillator is coupled to the collected rhythm of every other oscillator [35].

From this, Winfree was able to conclude that as the range of natural frequencies in a population is reduced, coupling occurs spontaneously amongst subpopulations. As the

frequency distribution narrows further, more and more of the oscillators cooperatively couple their motions. Winfree's model [30] is:

$$\frac{d\theta_i}{dt} = \omega_i + \frac{\kappa}{N}\sum_{j=1}^{N} X(\theta_j)\, Z(\theta_i) \tag{11}$$

for $i = 1,\ldots,N$ and $\kappa \geq 0$. In this equation, $\theta_i(t)$ is the phase of the ith oscillator at time t, and κ is the coupling strength. The frequencies ω_i are taken from a symmetric, unimodal distribution $g(\omega)$, which has a width Γ, and is time-scaled to have a mean of 1 [30]. The coupling can be interpreted in the following way: each oscillator j exerts a phase-dependent effect $X(\theta_j)$ on every other oscillator. The response of oscillator i to the average effect from the whole population depends on its phase θ_i, via the sensitivity function $Z(\theta_i)$ [35]. Tying this into the earlier explanation, when $\kappa = 0$ (no coupling/locking), the oscillators behave incoherently per their randomly varying natural frequencies. Increasing κ, or sampling from a narrower $g(\omega)$, leads to frequency coupling (also called locking).

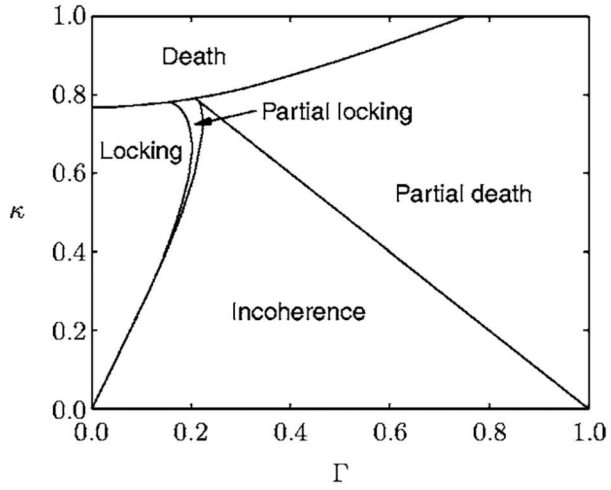

Figure 32 Stability diagram for a special case of the Winfree model. Taken from [30]

Figure 32, taken from Quinn [30], shows a stability diagram for the Winfree model, in the special case where $X(\theta) = 1 + \cos(\theta)$ and $Z(\theta) = -\sin(\theta)$. The plot shows the

case of *N*=800 oscillators with natural frequencies evenly distributed on the interval [1- Γ, 1+ Γ]. Notice that for a given distribution width, say Γ=0.1, increasing from $\kappa = 0.1$ to $\kappa = 0.3$, takes the system from a state of incoherence to a phase-locked state. Similarly, for a given value of coupling strength, say $\kappa = 0.4$, reducing the width of the distribution from Γ=0.2 to Γ=0.1, takes the system from an incoherent to a coupled state. Oscillation death occurs when oscillators achieve a stable rest state [36].

While revolutionary, Winfree's model is difficult to use. It requires two arbitrary functions, $X(\theta_j)$ and $Z(\theta_i)$, as well as knowledge of both absolute phases, θ_i and θ_j [30]. In 1975, Kuramoto published [37] a refinement of Winfree's model:

$$\frac{d\theta_i}{dt} = \omega_i + \frac{K}{N}\sum_{j=1}^{N} \sin(\theta_j - \theta_i) \qquad (12)$$

for $i = 1,\ldots,N$ and $K \geq 0$. As before, frequencies ω_i are taken from a symmetric, unimodal distribution $g(\omega)$. [30]. *K* is the coupling constant: it serves the same function as κ, but may take on different values. This is much simpler than Winfree's model! The arbitrary functions $X(\theta_j)$ and $Z(\theta_i)$ have been replaced by the more familiar sine function; and furthermore, coupling now depends only on the phase difference $(\theta_j - \theta_i)$, not on the values of the individual phases θ_j and θ_i. This gives insight into the rotational symmetry of the problem [30]. It can also be determined that the Kuramoto model produces three distinct states [38]:

i. When $\frac{K}{N}$ is small, and/or the phase difference $(\theta_j - \theta_i)$ is large (but not close to 180°), oscillators vibrate according to their natural frequencies and do not couple.

ii. When $\frac{K}{N}$ is large, and/or the phase difference $(\theta_j - \theta_i)$ is small, the entire population of oscillators exhibits phase coupling.

iii. For the remaining combinations of moderate $\frac{K}{N}$ and phase difference $(\theta_j - \theta_i)$, a partially-coupled state emerges, in which a subpopulation of oscillators phase couple to one another.

Note that because of the cyclic nature of the sine function, a 180-degree phase difference corresponds to perfect anti-symmetry, and will induce coupling. These three states correspond to the three states present near the origin of the Winfree model, shown in Figure 32. This makes sense, because in the case of weak coupling and nearly identical natural frequencies, the Winfree model reduces precisely to the Kuramoto model [30].

A complex order parameter $r(t)$ can be defined for the Kuramoto model. It can be thought of as a macroscopic quantity corresponding to the collective rhythm produced by the entire population of oscillators [35]. It has the benefit of making it easier to visualize the effects of parameter changes on the behavior of oscillator populations.

$$re^{i\psi} = \frac{1}{N}\sum_{j=1}^{N} e^{i\theta_j} \tag{13}$$

Here, $r(t)$ determines the phase coherence, and $\psi(t)$ is the average phase among the oscillators. If every oscillator is phase-coupled, $r = 1$. If every oscillator vibrates at its own unique natural frequency, $r = 0$ [39]. The Kuramoto model can be rewritten in terms of this parameter [35]:

$$\frac{d\theta_i}{dt} = \omega_i + Kr\sin(\psi - \theta_i) \tag{14}$$

for $i = 1,\ldots,N$. This form illustrates clearly the comparison of the phase of each individual oscillator to the overall phase behavior of the system. Furthermore, one can see that the overall strength of coupling is proportional to the complex order parameter, r [35]. This explains the spontaneous coupling phenomenon Winfree observed: as the population becomes more coherent, r increases, which increases the overall coupling strength Kr. This enables the coupled subpopulation to pull more oscillators closer to its average phase, which may increase r further. This process continues until the addition of oscillators fails to increase the complex order parameter, at which point the process self-limits [35].

By defining a critical coupling constant, K_c, it is possible to evaluate the evolution of the complex order parameter over time. Figure 33, taken from Strogatz [35], shows a numerically-derived time evolution of $r(t)$. For $K < K_c$, order decreases, and the system becomes uncoupled. For $K > K_c$, order converges to a nonzero value of r.

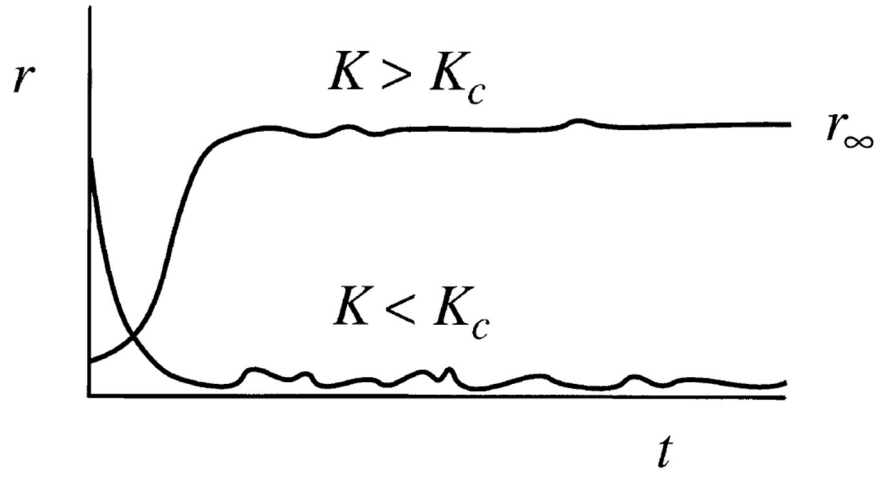

Figure 33 Time evolution of the complex order parameter r(t). Taken from [35]

One can also visualize directly the impact that varying the coupling constant, K, has on the complex order parameter, r. Figure 34 shows that the system is disordered (uncoupled)—despite increases in the coupling constant, K—until critical value K_c is reached. Increasing

K beyond the value K_c causes r to increase rapidly to convergence. Furthermore, the non-responsiveness of r to changes of K below K_c, suggests that the final phase coherence depends only on K, and not on initial conditions [35].

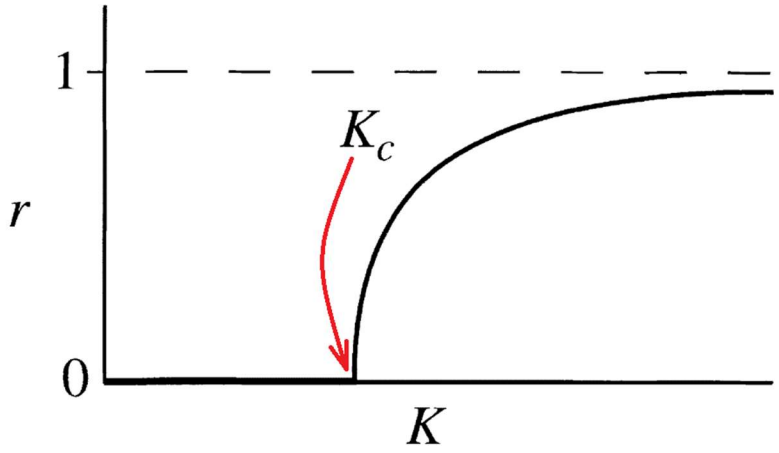

Figure 34 Dependence of order parameter, r*, on the coupling strength,* K*. Taken from [35]*

A further refinement of the Kuramoto model was provided by Bronski [38] in 2012. For the case of fully coupled, phase-locked oscillators, and a Gaussian frequency distribution $g(\omega)$, Bronski found that the standard Kuramoto model errs by a logarithmic factor. This is due to the external value statistics of the random frequency vector [38]. The specification of a Gaussian distribution does not make this a highly specialized case. Indeed, it is widely used and is the correct distribution for any number of physical and biological applications. This correction factor is:

$$\frac{\sqrt{\log(N^2)}}{N} \tag{15}$$

as opposed to the previously accepted factor of:

$$\frac{1}{N} \tag{16}$$

This gives a slightly altered version of the complete model [38]:

$$\frac{d\theta_i}{dt} = \omega_i + K\frac{\sqrt{\log(N^2)}}{N}\sum_{j=1}^{N}\sin(\theta_j - \theta_i) \tag{17}$$

5.3 Properties of Simple Systems of Coupled Oscillators

While the Winfree and Kuramoto models consider systems with large numbers of oscillators, there is also much to be gained from an analytical look at simpler systems consisting of only a small number of oscillators. It will be useful now to formalize the distinction between synchrony and coupling. Synchrony is the simplest behavior case of coupled identical oscillators [27], but not the only case. For example, a system of two identical oscillators has exactly two stable coupled states. Synchrony is a special case of coupling in which the phase difference is precisely 0°.

A system of three identical oscillators is slightly more complicated, but still easily parsed. This first coupled case is again synchrony. There is a second possible state with oscillators whose periods differ by one third. Another stable state is two oscillators in synchrony and one completely uncoupled (but still with the same period). The fourth and final stable coupled state is where two oscillators are 180° out of phase, and the third oscillates with half the period. This third oscillator is driven by the combined effect of the first two. One can imagine that it receives an input of energy every time one of the other two oscillators peaks [27].

Strogatz [27] also notes the parallels between the mathematical description of these states, and the gaits of various animals. A possible reason for this is that while animal limbs bear little resemblance to oscillators of any kind, neurons have been shown to exhibit coupling behavior when firing [32].

5.4 Coupled Oscillations with Time Delay

Up to this point, the primary concern has been to describe the coupling of oscillators that communicate their phase information instantaneously. This is a useful simplification, and it is valid for many—if not most—coupled systems [39]. Recently, however, more attention has been devoted to the study of this neglected class of oscillator, which needs time to transmit its information. Yeung and Strogatz describe a simple example:

> "[T]he problem is similar to that faced by the fans sitting in an enormous football stadium, all of whom (we suppose) are trying to clap in unison. Even if everyone were successfully clapping in perfect synchrony, it would not sound that way to the fans themselves, as the applause coming from far across the field would be significantly delayed, because of the finite speed of sound" [39].

Given this difficulty, is phase-coupling possible in these sorts of situations? To address this, Yeung and Strogatz provide a modification of the Kuramoto model [39]. Because this investigation predates Bronski's work [38], this model uses Kuramoto's original correction factor, and not Bronski's improvement:

$$\frac{d\theta_i}{dt} = \omega_i + \xi_i(t) + \frac{K}{N}\sum_{j=1}^{N} \sin[\theta_j(t-\tau) - \theta_i(t) - \alpha] \qquad (18)$$

for i = 1,…,*N*. As in the original Kuramoto model, $\theta_i(t)$ is the phase of the *i*th oscillator at time *t*, and *K* is the coupling constant. Once again, ω_i are taken from a symmetric, unimodal distribution $g(\omega)$, except with the change that the mean of $g(\omega)$ is now taken to be ω_0. τ is the time delay, α is a phase frustration parameter, and $\xi_i(t)$ is a white noise function which represents frequency fluctuations due to temperature [39]. Notice that this reduces to Kuramoto's original model in the case of $\tau = \alpha = \xi_i(t) = 0$.

By setting $\xi_i(t) = 0$, Yeung is able to determine conditions under which time-delayed oscillators exhibit stable behavior. Incoherence—no coupling between oscillators—is stable, and will persist, when the following two conditions are met [39]:

$$K < \frac{\omega_0}{2n-1} \tag{19}$$

$$\frac{(4n-3)\pi}{2\omega_0 - K} < \tau < \frac{(4n-1)\pi}{2\omega_0 + K} \tag{20}$$

for any positive integer *n*. Stated another way, the oscillators can remain in a disordered state if these first two conditions are met. Furthermore, Yeung is able to conclude that stable synchronized states do *not* exist if and only if:

$$K < \frac{\omega_0}{2(2n-1)} \tag{21}$$

$$\frac{(4n-3)\pi}{2\omega_0 - 2K} < \tau < \frac{(4n-1)\pi}{2\omega_0 + 2K} \tag{22}$$

again for any positive integer *n* [39]. If these last two conditions are met, coupling can never occur.

These two regions can be compared, as in Figure 35. The Y-axis is coupling strength *K*, normalized by ω_0. The X-axis has units of $\omega_0\tau$, that is, time delay given in periods. The area underneath the grey curves (including the black area) is that defined by Yeung's first two conditions: parameter space in which oscillators can remain in a disordered state. The black regions are the parameter space defined Yeung's two later conditions: circumstances under which coupling can never occur. This leads to an important observation: there are grey regions that are not also black. In these regions, the system exhibits bistability [39]: stable coupling is possible, but so is stable incoherence.

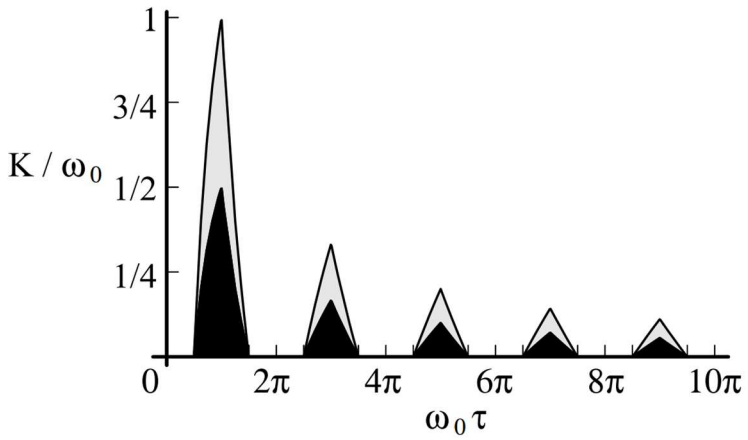

Figure 35 Coupling cannot occur in black regions. The incoherent state is stable in grey and black regions. Taken from [39]

5.5 Application of Coupled Oscillators

The vibrating magnetic antenna uses an array of vibrating, coupled, permanent magnets to generate magnetic signals. Changing the stiffness alters the natural frequency of an oscillator. Because each oscillator will tend to vibrate at its own natural frequency, any variation in the manufacture of the individual oscillators, or in the bias current, will result in different oscillators having somewhat dissimilar vibration frequencies. This is problematic, because to produce a coherent signal the entire population of magnetic oscillators must be able to reliably and quickly couple to the same frequency.

The Bronski-Kuramoto model can be used to evaluate this design challenge. A Gaussian distribution of oscillator natural frequencies is appropriate for manufactured devices. The coupling constant K is determined by the force of the magnetic field acting on each oscillator, according to:

$$\boldsymbol{F} = \nabla(m \cdot \boldsymbol{B}) \tag{23}$$

where m is the magnetic moment of the oscillating magnet, and $\boldsymbol{B}$ is the overall magnetic field. N is the number of magnetic oscillators. Numeric simulations of the model may be

used to determine the maximum phase difference $\theta_j - \theta_i$ between oscillators for which total phase locking will occur. This determines the manufacturing tolerances needed for the magnetic oscillators.

6 SIMULATION STUDY OF Y-STATOR BEHAVIOR

6.1 Specifications of Model

A simulation study was conducted using COMSOL software to model and investigate the behavior of the proposed permalloy Y-stator configuration. Table 1 lists the material properties used. The system was filled with gaseous air with a relative permeability of 1. An iron magnet (relative permeability set equal to 4,000) was magnetized lengthwise at 750,000 A/m. Stators were assigned a preloaded material—nickel steel supermalloy, with a relative permeability of 800,000.

	Air [Gas]	Iron	Nickel Steel Supermalloy
Relative Permeability	$\mu_r = 1$	$\mu_r = 4{,}000$	$\mu_r = 800{,}000$
Magnetization	-	750,000 A/m	-

Table 1. Material properties and magnetization

Model dimensions are detailed in Table 2. The size of the air box was limited by the computational power available, and may be the source of edge effects. Gap spacing refers to the space left between magnet and permalloy stators, at closest approach. This value was chosen to be 1 millimeter, as a conservative estimate of what might be easily achieved in a first prototype of the device.

	Width	Depth	Height
Magnet	x = 0.08 meters	y = 0.02 meters	z = 0.02 meters
Air Box	x = 0.50 meters	y = 0.20 meters	z = 0.40 meters
Permalloy	x = 0.02 meters	y = 0.02 meters	z = 0.06 meters
Gap Spacing	x = 0.001 meters		

Table 2. Dimensions of Y-stator components in COMSOL models

6.2 Single Y-Stator Model

A single Y-stator featuring three permalloy stators and a single bar magnet was the first configuration investigated. The system was modeled with the magnet in five different

positions across its range of motion, as show in Figure 36 through Figure 40. Thin red lines trace the magnetic field paths, and the red arrows indicate field direction and magnitude, with the reference point being the end of their tails.

Figure 36 shows that the two permalloy stators adjacent to the magnetic bar project the field as expected, as indicated by the top two magnetic vector arrows. Figure 40 demonstrates projected field reversal (along with a slight angle change, potentially caused by edge-effects of the air box), as indicated by the bottom two magnetic vector arrows. However, the third stator (the stator farthest away from the magnet) continued to project the field (bottom arrow in Figure 36, and top arrow in Figure 40). Not only that, but it projects the field in the opposite direction. This was unexpected behavior. In fact, the "far away" stator continues to project in each of Figure 36 through Figure 40, the entire range of motion for the device. The is potentially problematic, because it may be partially canceling-out the net projected oscillating field.

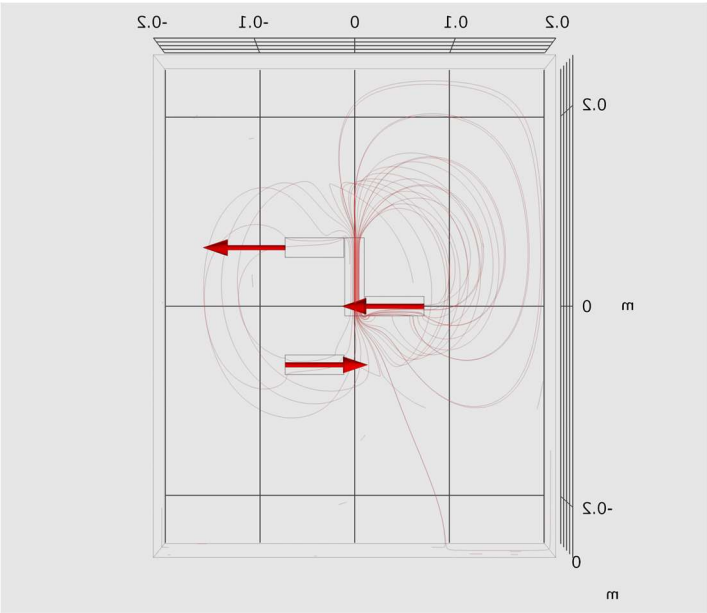

Figure 36 COMSOL model of single Y-stator device in position 1

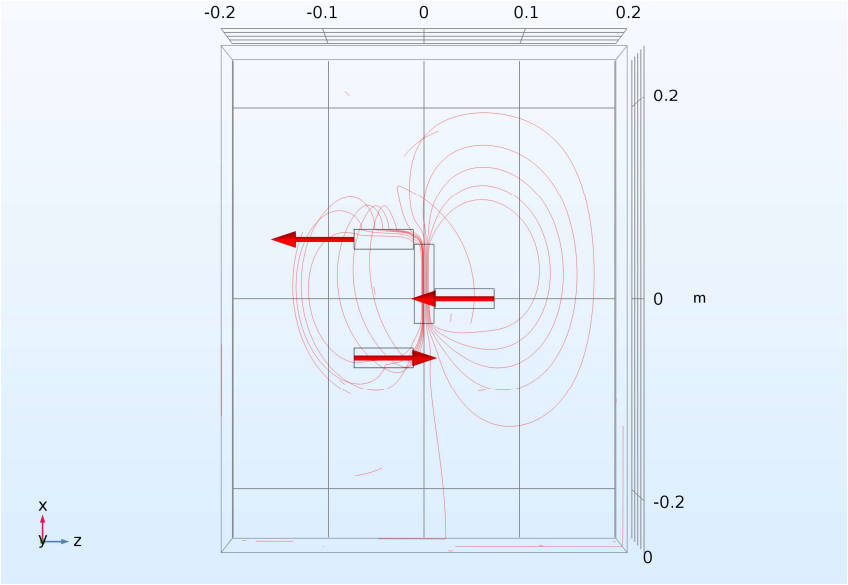

Figure 37 COMSOL model of single Y-stator device in position 2

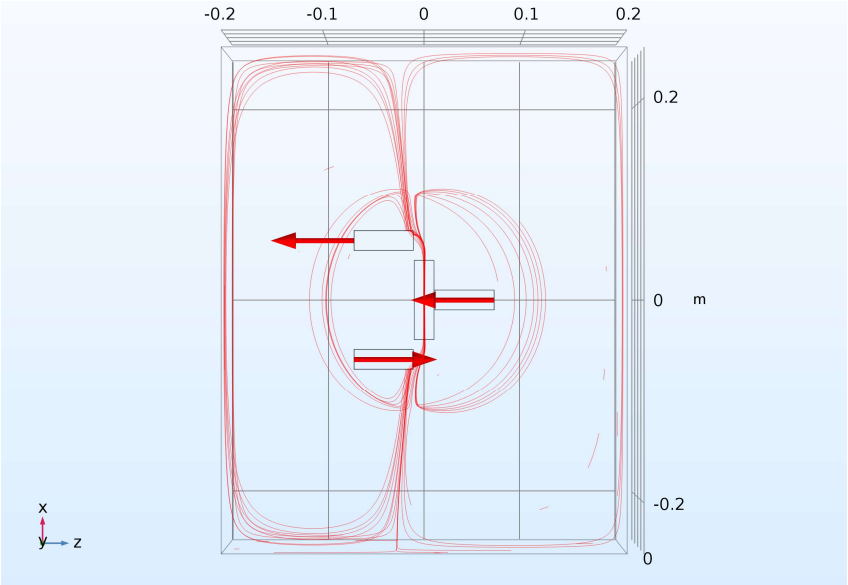

Figure 38 COMSOL model of single Y-stator device in position 3

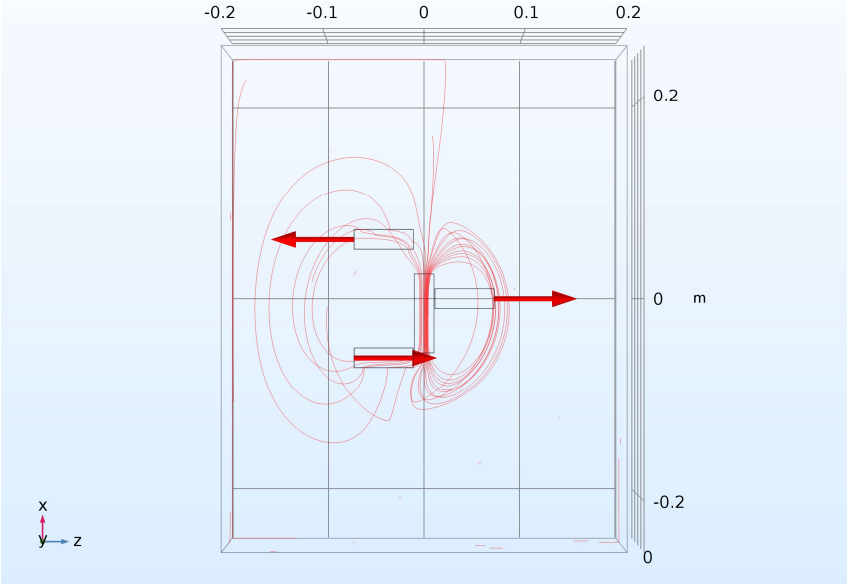

Figure 39 COMSOL model of single Y-stator device in position 4

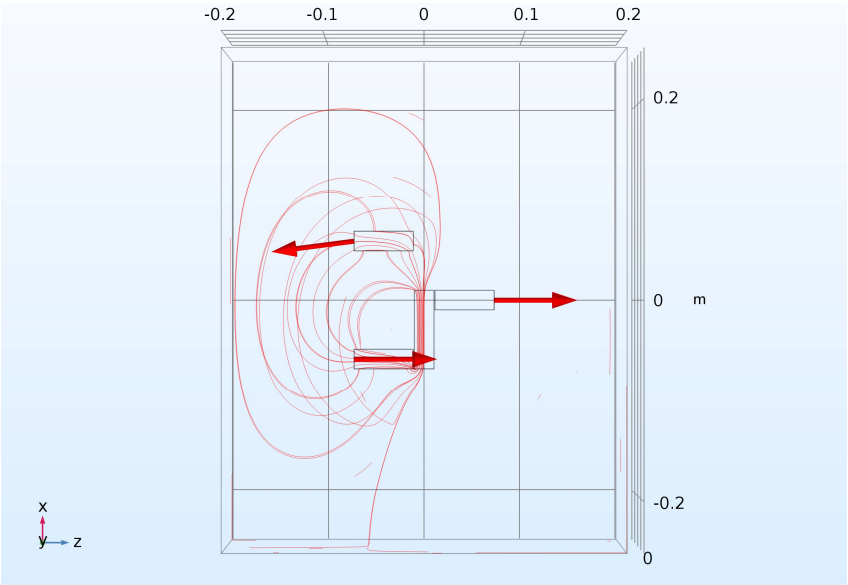

Figure 40 COMSOL model of single Y-stator device in position 5

6.3 Forces and Torques in Single Y-stator Model

COMSOL was used to determine forces and torques at a point 0.1 meters above the origin of the model (that is, 0.1 meters towards the reader as shown in the birds-eye views of Figure 36 through Figure 40). These appear in Table 3.

	Position 1	Position 2	Position 3	Position 4	Position 5
Electromagnetic force, X-component (N)	-0.83233	2.7707	-1.2256	-3.1292	0.047377
Electromagnetic force, Y-component (N)	-1.0439	-0.46017	-1.2256	0.58543	-0.30008
Electromagnetic force, Z-component (N)	-0.82449	-17.883	-3.2411	-18.51	-1.0933
Torque, X-component (N*m)	0.0055551	-6.85E-04	-0.0018383	0.0024586	-0.0028191
Torque, Y-component (N*m)	1.5611	1.085	0.069338	-1.1107	-1.636
Torque, Z-component (N*m)	-0.018327	-0.053385	0.074086	0.015514	-0.0069403

Table 3. Forces in COMSOL model of single Y-stator

6.4 Gang of Triple Y-Stators

Modeling a system of Y-stators is important both for understanding versions of the magnetic transmitter which require multiple oscillators for greater signal strength, as well as to investigate the "opposite direction" field arrow observed in models of the single Y-stator. A system of three ganged Y-stators is shown in Position A (Figure 41) and Position B (Figure 42). While there are again some off-axis angle tweaks apparent, the system shows good field reversal. Even more promising, since there is now only one "distant" permalloy stator (bottom stator in Figure 41, top stator in Figure 42), there is now only one "opposite direction" projected field out of seven total projecting stators. This is a marked improvement over the single Y-stator configuration, in which one-third of the stators projected an opposite-direction field. This observation provides a compelling argument for the development of ganged Y-stator transmitters with multiple (or many) magnet oscillators.

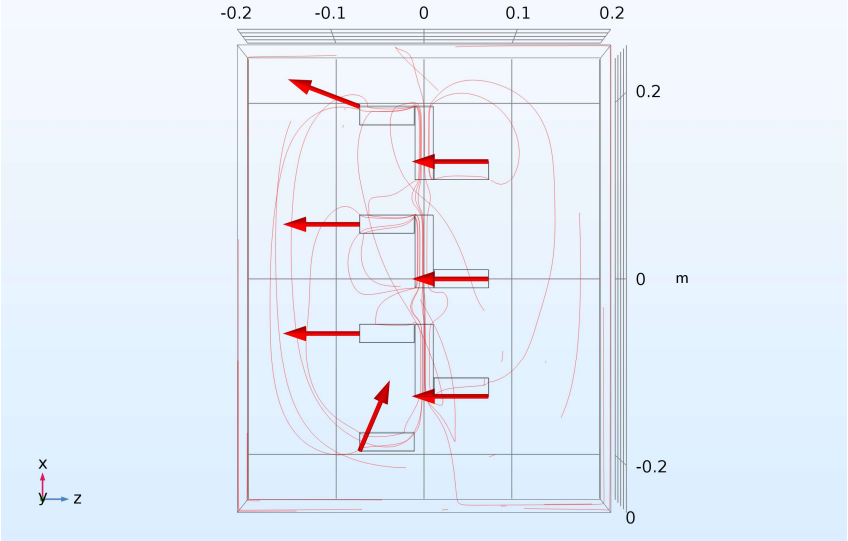

Figure 41 COMSOL model of Y-stator gang in position A

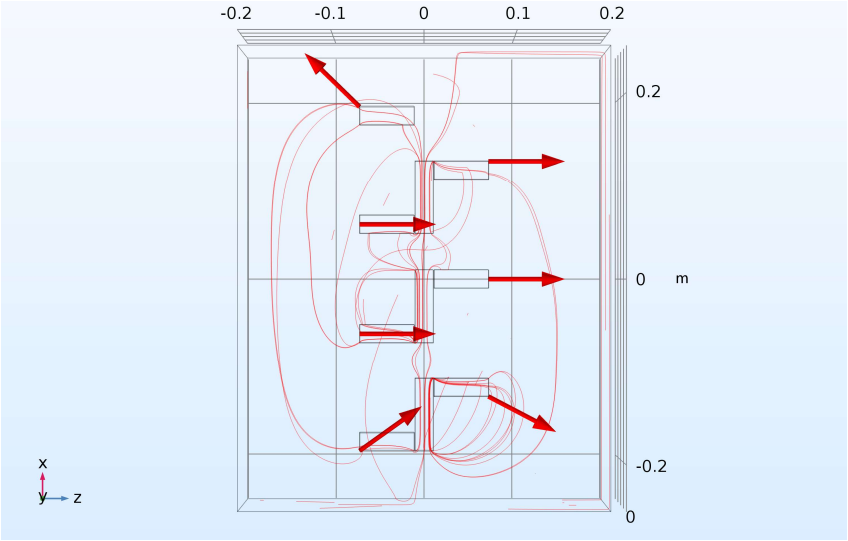

Figure 42 COMSOL model of Y-stator gang in position B

7 DEVELOPMENT OF TESTING APPARATUS

7.1 Magnetometers

A Honeywell HMR2300 3-axis Hall magnetometer (Figure 43(a)) was used for much of the early testing and concept evaluation. This unit, however, is large (approximately four inches long), requires an external 120-volt power supply, and retails for over $800. While it has excellent performance, these limitations make it somewhat unsuited for compact, inexpensive, low-power IoT systems. Because of this, later iterations of testing utilized a Honeywell HMC5883L 3-axis Magnetoresistive Arduino magnetometer, shown in Figure 43(b). While not quite as sensitive as the HMR2300, this unit still performs well. It measures less than 1-inch square, costs less than $10, and can be controlled and powered by an Arduino microcontroller.

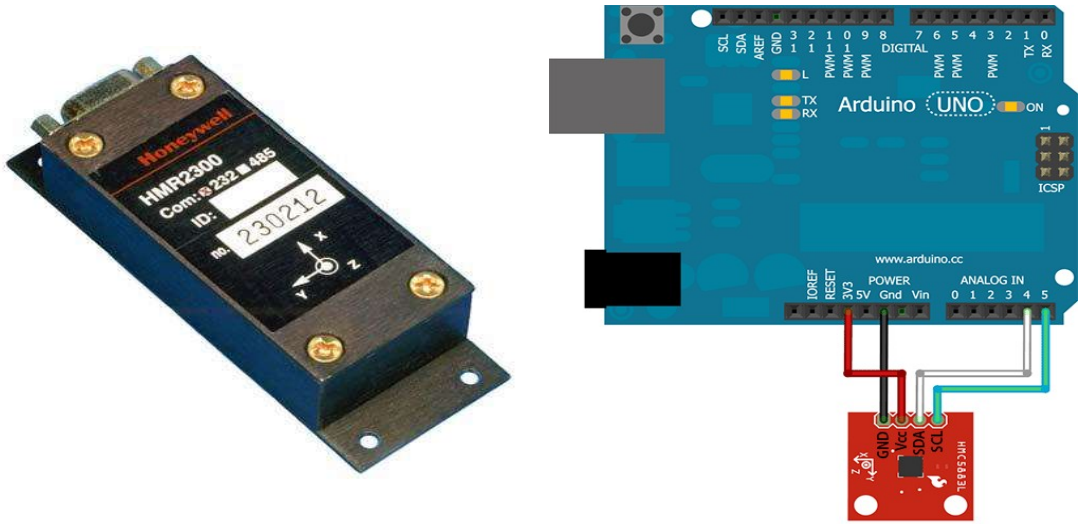

(a) (b)

Figure 43 (a) Honeywell HMR2300 magnetometer [40], and (b) Honeywell HMC5883L Arduino magnetometer [41]

7.2 Rotating Magnet Flow Meter System

The rotating magnet flow meter system is summarized in Figure 44.

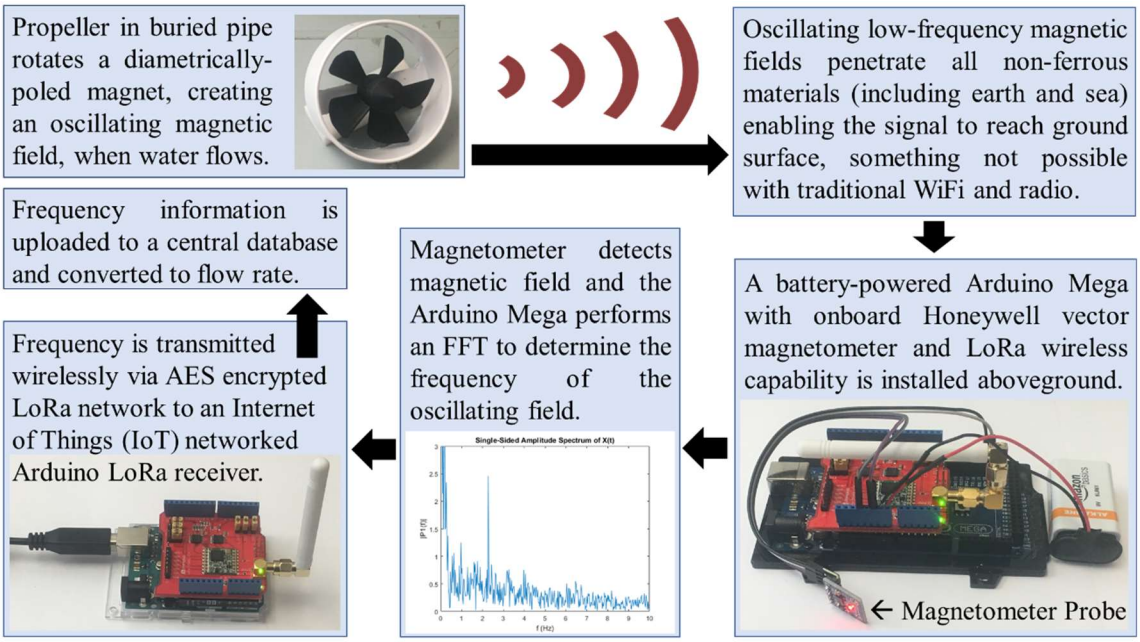

Figure 44 Magnetic telemetry with underground IoT flow sensor

Figure 45 shows (a) SolidWorks assembly of the two-piece modular propeller, (b) the nose cone which holds the diametrically magnetized cylinder, and (c) the propeller without the noise cone. It was printed using polylactic acid (PLA) plastic. When assembled, the nose cone is fixed to the propeller body. The propeller assembly rides on two low-resistance ceramic ball bearings, which are press-fitted into the 3D printed propeller part. Traditional steel ball bearings were used in a first prototype, but they interacted with the rotating magnet, creating drag. The ceramic ball bearings have the additional advantage of not rusting. The two ball bearings ride on a nonmetallic fiberglass bolt—with head underneath the nose cone, and threads extending out the back of the propeller. A fiberglass nut secures the bearings, and keeps the propeller from sliding on the bolt. The protruding, threaded end of the bolt can be threaded into a mount for flow-meter installation.

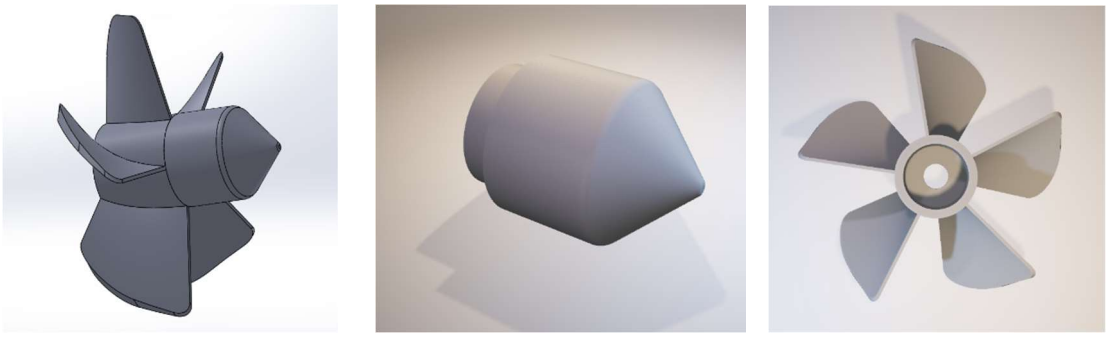

(a) (b) (c)

Figure 45 Three views of rotating magnet flow meter SolidWorks Model

7.3 Rotating Magnet Moisture Sensor

A version of the rotating magnet moisture sensor is shown in Figure 46. A low-power electric motor drives a diametrically magnetized neodymium magnet. An Arduino Uno provides the control. The Arduino connects to a moisture sensor through a signal amplifier. As moisture content increases, the Arduino spins the motor faster.

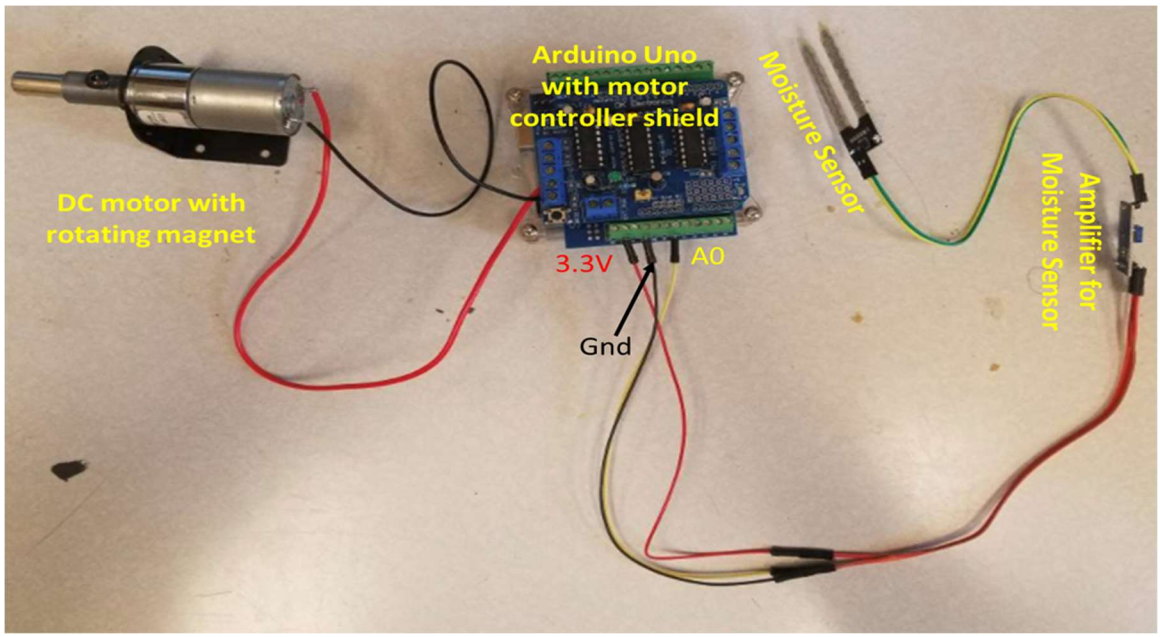

Figure 46 Moisture sensor design

Figure 47 details how this configuration enables magnetic telemetry. Note that it shows a slightly different build of the moisture sensor: here the moisture sensor connects directly to a relay instead of an Arduino. This is a simpler configuration, but it provides

only on/off (yes/no) moisture sensing, and is unable to detail specific moisture content by altering the rotational frequency. Nevertheless, whether controlled by an Arduino or a relay, the operating principles remain the same.

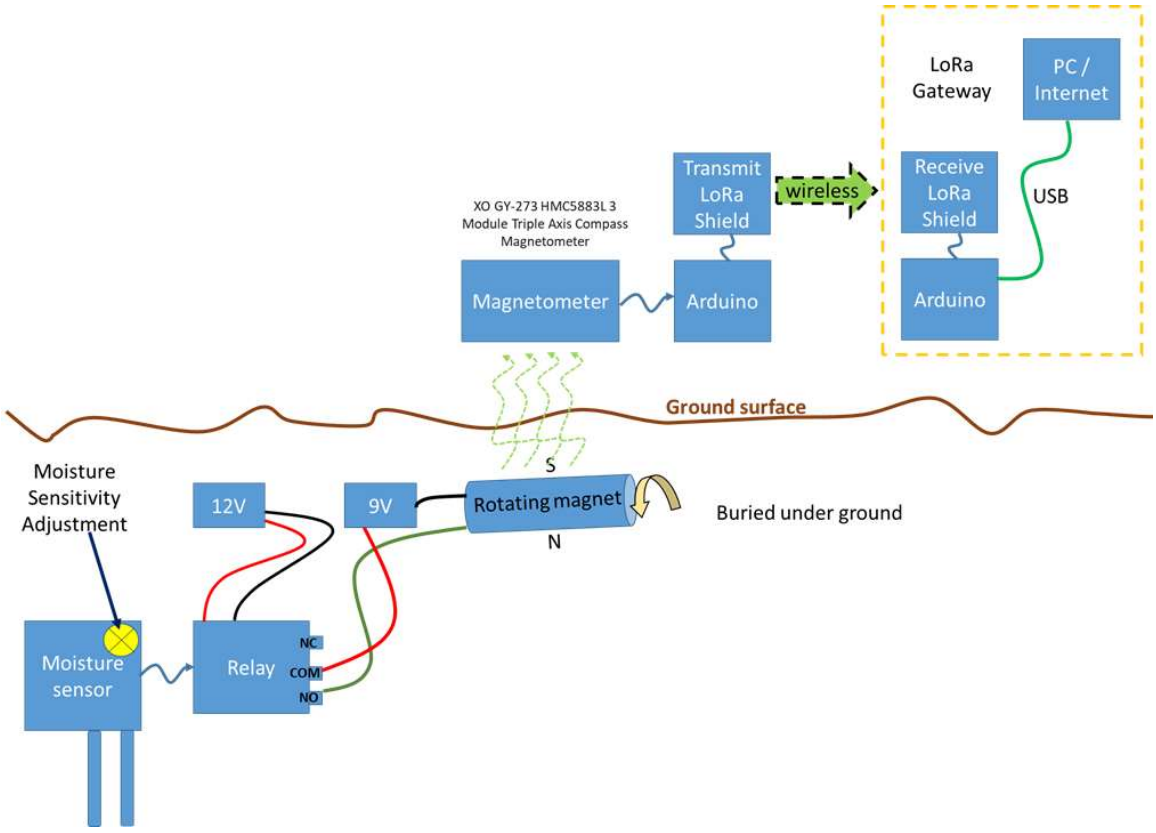

Figure 47 Magnetic telemetry with IoT-linked moisture sensors

7.4 Design and Features of Arduino Code

7.4.1 Magnetometer Receiver with LoRa Transmitter

The magnetometer receiver with LoRa transmitter is shown in Figure 48. The device is controlled by an Arduino Mega run off a 9-volt battery. Connected to this are an HMC5883L 3-axis magnetometer and a Dragino LoRa Long Range Transceiver Shield. The device runs on custom Arduino code provided in Appendix A. It is set up to take 20 magnetic field strength samples per second using the magnetometer. 256 samples are taken for each of the X, Y, and Z axes. A 256-bin Fast Fourier Transform (FFT) is then performed

using the arduinoFFT.h library on each axis dataset to calculate the frequency spectra. This is the reason for using an Arduino Mega instead of the slightly less expensive Arduino Uno: the Uno lacks the computational memory to perform the 256-bit transform. Next, the major frequency feature for each axis is determined. Because an FFT of noise (in this case, if no oscillating magnetic field is present or detectable) will still produce a frequency spectrum, a signal amplitude check is performed on the time-domain signal data for each of the three axes. If the signal amplitude fails to exceed a user-set threshold value, the system overwrites the calculated frequency (for that axis) with a value of 0.00. Signal amplitude values are then encrypted using the 128-bit AES AESLib.h encryption library. These encrypted values are then transmitted via LoRa.

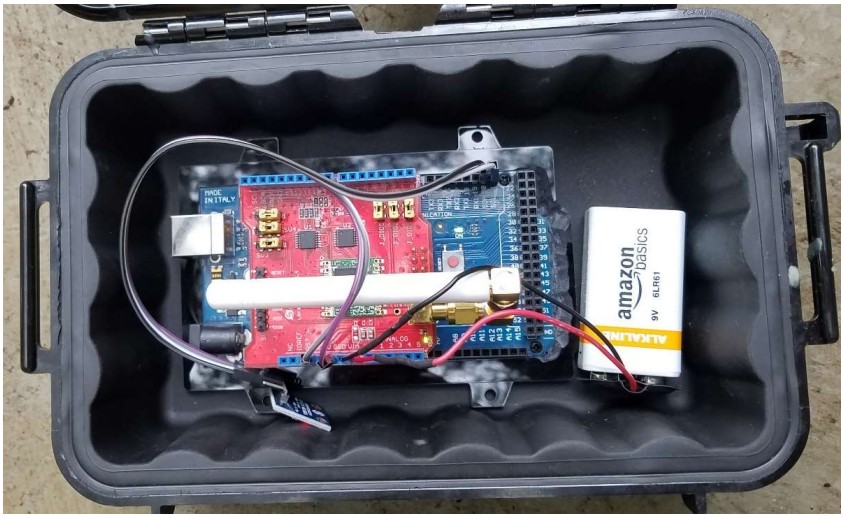

Figure 48 Magnetometer receiver (Arduino Mega with HMC5883L magnetometer) with LoRa transmitter in weatherproof case

7.4.2 LoRa Receiver

The LoRa receiver consists of an Arduino Uno with a Dragino LoRa Long Range Transceiver Shield. Custom Arduino code—again available in Appendix A—receives and decrypts the LoRa transmission. Data are uploaded via USB serial port to a data-acquisition PC.

8 TEST RESULTS

8.1 Amplitude Thresholds

Tests were conducted to verify the functionality of the previously described amplitude-check in the LoRa transceiver system. The threshold level was set based on time-domain signal amplitude, with the X, Y, and Z channels all set to same threshold level. The test was conducted with a two-foot separation between rotating diametric magnet and magnetometer. This threshold level was tweaked until a dimensionless value of 150 was determined to be appropriate for a two-foot separation. With the threshold at this level, the system reliably detected a 2 Hz source signal, while also filtering-out noise when the 2 Hz source was disabled. The test was performed with the magnetometer receiver in three different orientations (Figure 49), so that each of the X, Y, and Z magnetoresistive sensors faced the rotating source. Data were acquired via USB serial port to simplify acquisition.

(a)

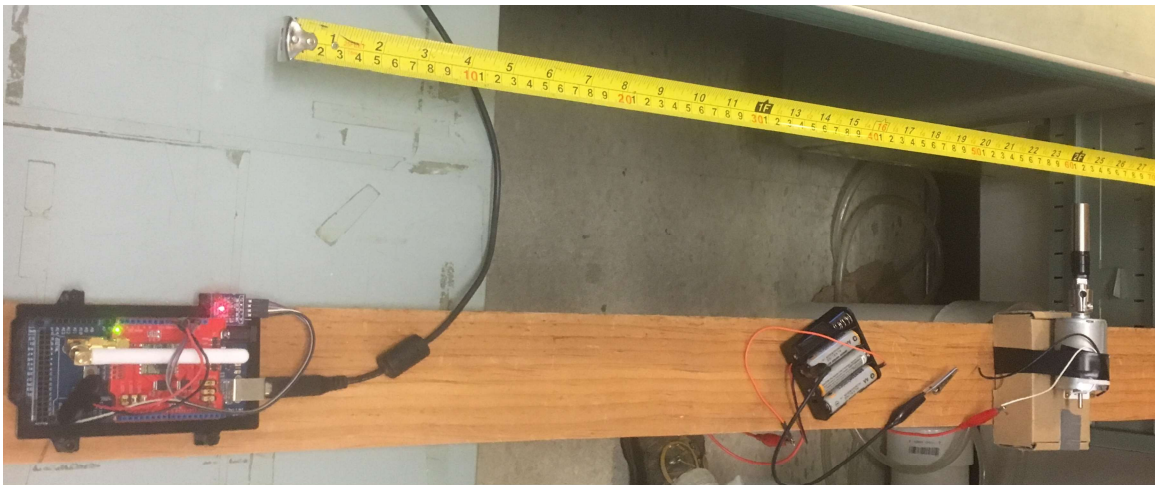

(b)

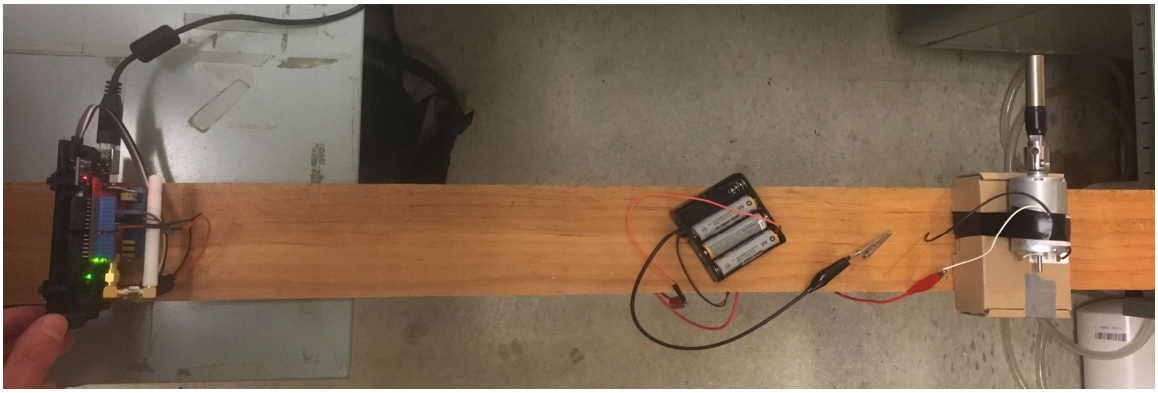

(c)

Figure 49 Three orientations of test setup for amplitude threshold test

Results of this test appear in Table 4. In Orientation (a), the Y-axis of the magnetometer experiences the greatest signal amplitude increase due to the spinning magnet. In Orientation (b), the X-axis of the magnetometer experiences the greatest signal amplitude increase due to the spinning magnet. However, maximum signal strength remained below 150, so the X-frequency was not transmitted. Setting the X,Y,Z thresholds independently is one solution to this. In Orientation (c), the Z-axis of the magnetometer experiences the greatest signal amplitude increase due to the spinning magnet.

Orientation (a)

Serial output (motor off)			Serial output (motor on)		
Trial 1	Trial 2	Trial 3	Trial 4	Trial 5	Trial 6
X-max amplitude: -6 Y-max amplitude: -147 Z-max amplitude: 134	X-max amplitude: -7 Y-max amplitude: -147 Z-max amplitude: 135	X-max amplitude: -7 Y-max amplitude: -147 Z-max amplitude: 136	X-max amplitude: -14 Y-max amplitude: -192 Z-max amplitude: 134	X-max amplitude: -16 Y-max amplitude: -191 Z-max amplitude: 132	X-max amplitude: -14 Y-max amplitude: -193 Z-max amplitude: 133
X-direction frequency: 0.00 Y-direction frequency: 0.00 Z-direction frequency: 0.00	X-direction frequency: 0.00 Y-direction frequency: 0.00 Z-direction frequency: 0.00	X-direction frequency: 0.00 Y-direction frequency: 0.00 Z-direction frequency: 0.00	X-direction frequency: 0.00 Y-direction frequency: 6.61 Z-direction frequency: 0.00	X-direction frequency: 0.00 Y-direction frequency: 6.51 Z-direction frequency: 0.00	X-direction frequency: 0.00 Y-direction frequency: 6.44 Z-direction frequency: 0.00

Orientation (b)

Serial output (motor off)			Serial output (motor on)		
Trial 7	Trial 8	Trial 9	Trial 10	Trial 11	Trial 12
X-max amplitude: -10 Y-max amplitude: 94 Z-max amplitude: 146	X-max amplitude: -9 Y-max amplitude: 94 Z-max amplitude: 147	X-max amplitude: -10 Y-max amplitude: 93 Z-max amplitude: 147	X-max amplitude: -77 Y-max amplitude: 94 Z-max amplitude: 153	X-max amplitude: -78 Y-max amplitude: 96 Z-max amplitude: 153	X-max amplitude: -78 Y-max amplitude: 94 Z-max amplitude: 154
X-direction frequency: 0.00 Y-direction frequency: 0.00 Z-direction frequency: 0.00	X-direction frequency: 0.00 Y-direction frequency: 0.00 Z-direction frequency: 0.00	X-direction frequency: 0.00 Y-direction frequency: 0.00 Z-direction frequency: 0.00	X-direction frequency: 0.00 Y-direction frequency: 0.00 Z-direction frequency: 6.57	X-direction frequency: 0.00 Y-direction frequency: 0.00 Z-direction frequency: 6.50	X-direction frequency: 0.00 Y-direction frequency: 0.00 Z-direction frequency: 6.49

Orientation (c)

Serial output (motor off)			Serial output (motor on)		
Trial 13	Trial 14	Trial 15	Trial 16	Trail 17	Trial 18
X-max amplitude: 57 Y-max amplitude: 126 Z-max amplitude: 119	X-max amplitude: 60 Y-max amplitude: 127 Z-max amplitude: 121	X-max amplitude: 62 Y-max amplitude: 126 Z-max amplitude: 121	X-max amplitude: 58 Y-max amplitude: 162 Z-max amplitude: 212	X-max amplitude: 57 Y-max amplitude: 160 Z-max amplitude: 213	X-max amplitude: 58 Y-max amplitude: 161 Z-max amplitude: 212
X-direction frequency: 0.00 Y-direction frequency: 0.00 Z-direction frequency: 0.00	X-direction frequency: 0.00 Y-direction frequency: 0.00 Z-direction frequency: 0.00	X-direction frequency: 0.00 Y-direction frequency: 0.00 Z-direction frequency: 0.00	X-direction frequency: 0.00 Y-direction frequency: 6.42 Z-direction frequency: 6.42	X-direction frequency: 0.00 Y-direction frequency: 6.40 Z-direction frequency: 6.41	X-direction frequency: 0.00 Y-direction frequency: 6.33 Z-direction frequency: 6.33

Table 4. Amplitude thresholds

The X-direction sensor did not exceed the threshold value in any of these tests. It is likely this was due to the limited orientations tested, or, that this sensor is less sensitive than the Y,Z sensors, and will need its own (lower) threshold. This will be monitored during future testing. It is also worth noting that over the course of testing, the motor's

batteries appear to have been losing power—detected rotation frequency drops from 6.61 Hz at the beginning of the tests, to 6.33 Hz at the end.

Test results indicate that setting an amplitude threshold on the time-domain raw signal is an effective way to reduce the number of "noise" signals which are processed. With this improvement, background noise does not produce recorded frequencies and true signals are not filtered-out, with a proper threshold setting.

8.2 Sink in Lab

A rotating magnetic flow meter was installed in a short length of 4" diameter PVC pipe, and held under a high-flow drain pipe in Perkins 103 laboratory. The HMC5883L Arduino magnetometer collected and recorded magnetic field data. For a comparison, a commercial flow meter was connected to an Arduino Uno for data acquisition as shown in Figure 50(a).

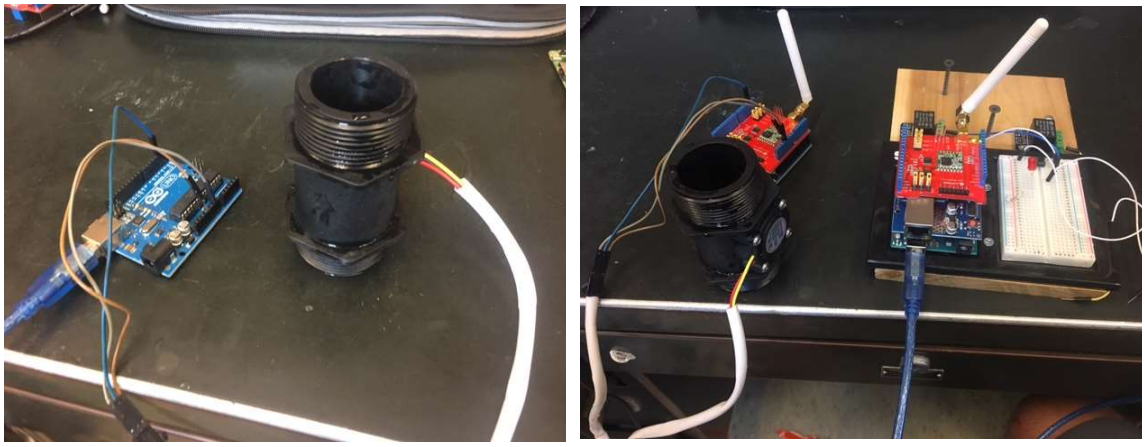

(a) (b)

Figure 50 (a) Commercial flow meter connected to Arduino for data collection, and (b) shown connected to LoRa transceiver components

By comparing the flow rate detected by the commercial flow meter, to the rate of rotation of the magnetic flow meter, a preliminary calibration of the magnetic flow meter can be performed.

(a)

(b)

Figure 51 (a) commercial flow meter under drain pipe in lab, and (b) rotating magnet flow meter under drain pipe in lab

Figure 51 shows both flow meters under test. Additional tests will allow for real-time conversion of rotating-frequency data into water flow-rates. Results from this test for the rotating magnet flow meter are shown in Figure 52. A frequency spike is visible between 2-3 Hz, on average approximately 2.3 Hz.

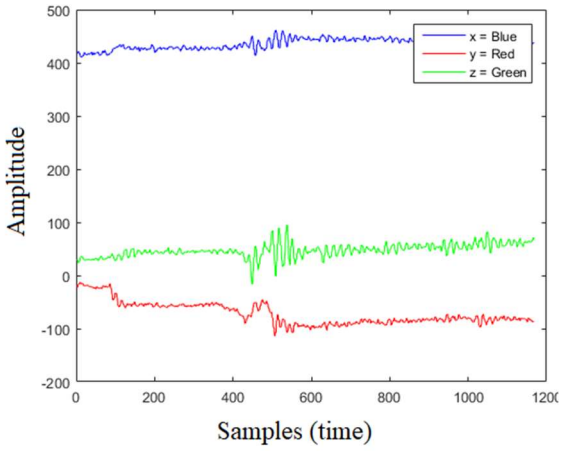

(a)

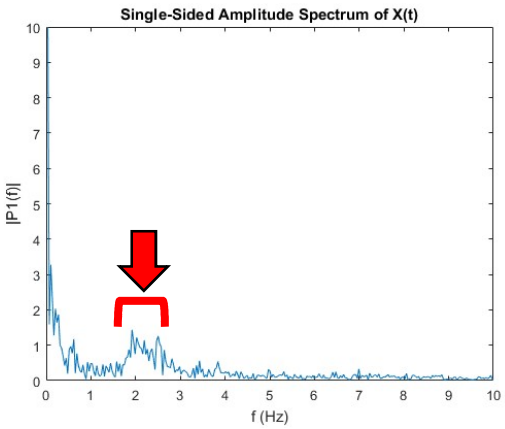

(b)

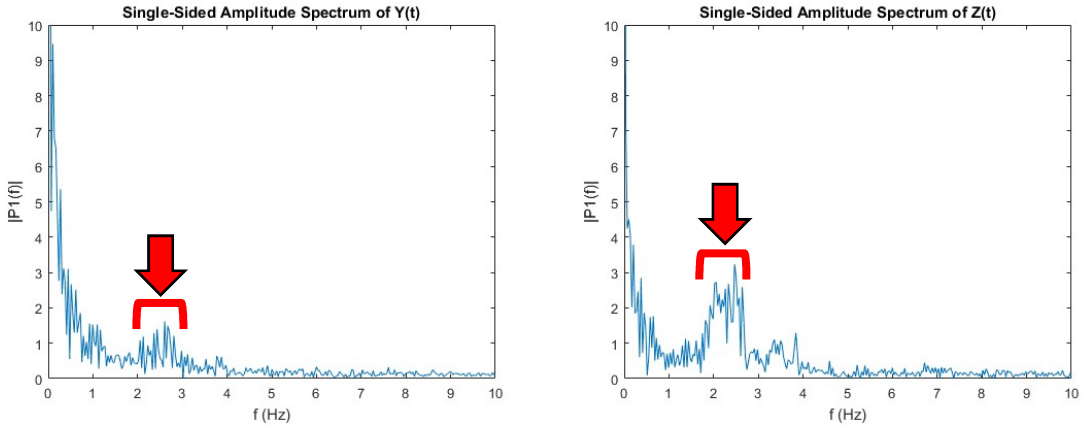

(c) (d)

Figure 52 Drain-test results for rotating magnetic flow meter: (a) magnetic signal time history, (b) X-axis rotation frequency: 2.25 Hz, (c) Y-axis rotation frequency: 2.5 Hz, (d) Z-axis rotation frequency: 2.25 Hz

Figure 53 shows the flow-rate data output of the commercial flow meter, exported via customized Arduino code. It shows a flow rate, on average, of roughly 34 L/min. This indicates that a rotation frequency of approximately 2.3 Hz from the rotating magnet flow meter may correspond to a flow rate around 34 L/min.

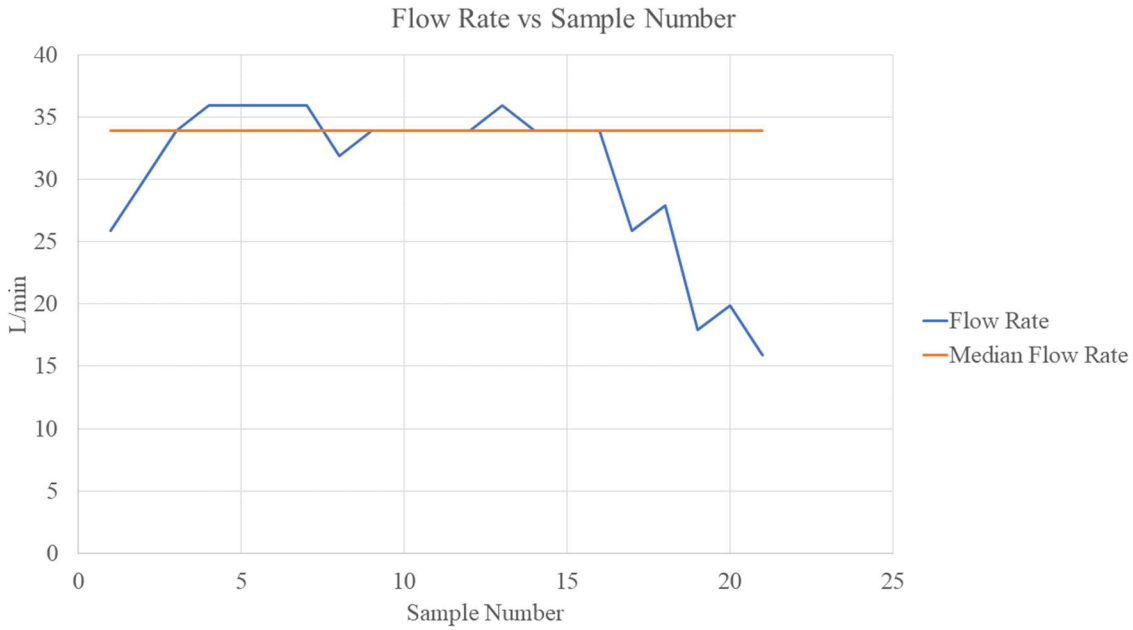

Figure 53 Flow-rate data output of commercial flow meter, recorded by Arduino controller

8.3 Concrete Slab

The goals of this test were to demonstrate functionality and LoRa integration of the rotating magnet moisture sensor, and also to demonstrate that a rotating magnet can be used to transmit information through a 5.5-inch-thick rebar-reinforced concrete slab. Figure 54 shows test setup details.

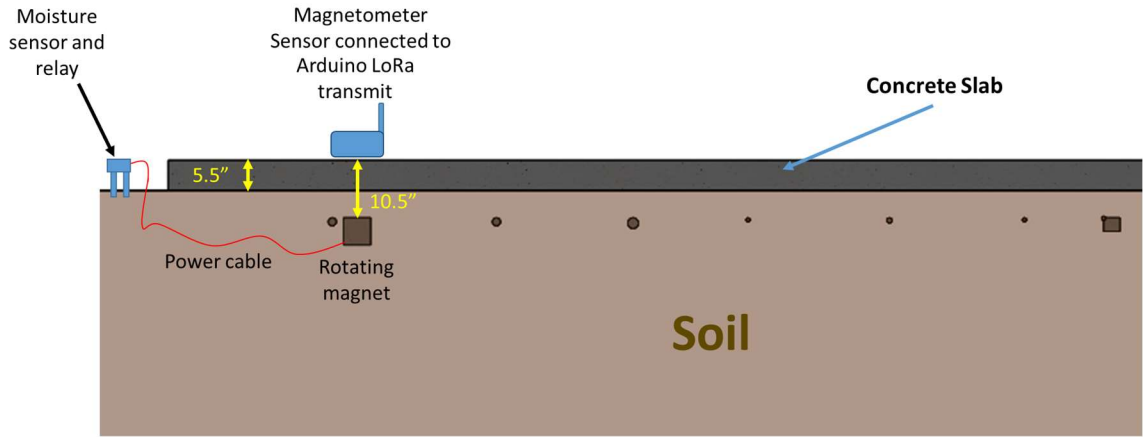

Figure 54 Schematic of moisture sensor test setup

The moisture sensor was inserted into damp soil, as shown in Figure 55(a). A rotating magnet source (Figure 55(b)) was buried under the concrete slab. The magnetometer-receiver/LoRa-transmitter unit was placed on the surface of the concrete.

Figure 55 (a) moisture sensor in soil, and (b) rotating magnet source before being buried under concrete slab

Figure 56(a) shows the LoRa receiver connected to a data-acquisition PC. Figure 56(b) shows the detected oscillation frequency: 1.6 Hz. This rotation rate can be used as a measure of the moisture content of the soil.

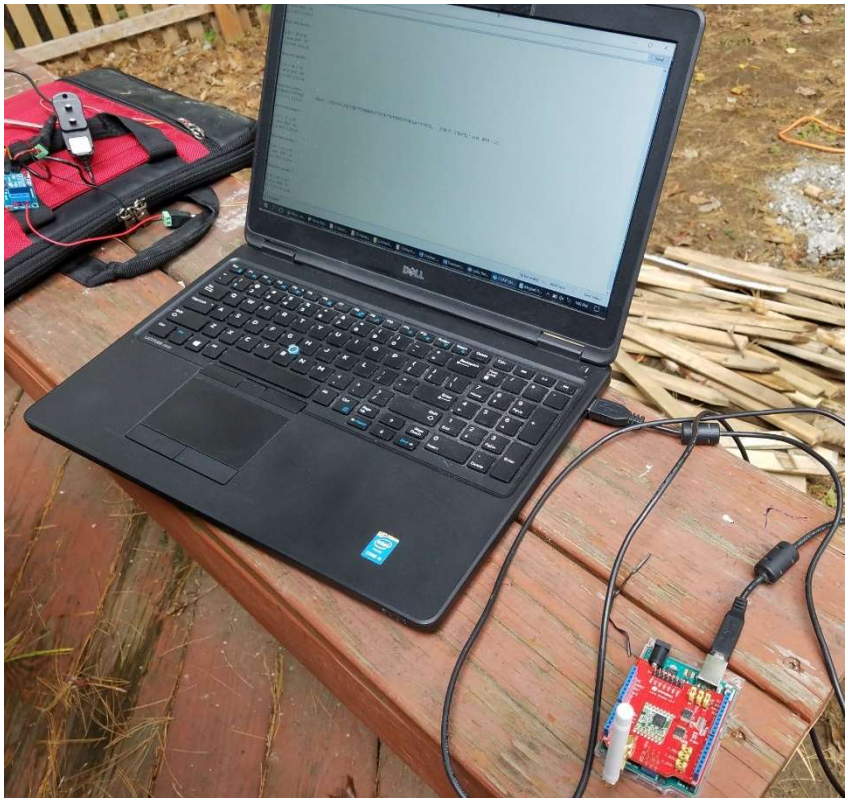

```
Received packet '

1.63 1.88 1.57
' with RSSI -59
1/1/1970 0:13:43

Received packet '

1.63 1.64 1.64
' with RSSI -60
1/1/1970 0:13:58

Received packet '

1.60 1.60 1.60
' with RSSI -60
1/1/1970 0:14:12

Received packet '

1.61 1.62 1.62
' with RSSI -58
1/1/1970 0:14:27

Received packet '

1.59 1.59 1.59
' with RSSI -63
1/1/1970 0:14:41
```

(a) (b)

Figure 56 (a) LoRa receiver connected to data-acquisition PC, and (b) acquired frequency data indicates periodicity of 1.6 Hz.

8.4 Flume

A flow test was performed with the rotating magnet flow meter and magnetometer/LoRa transceiver system at the University of Vermont Votey building flume. The flume is one meter wide, and a circular drain dam was installed 483 cm down

its length. The inner diameter of the circular drain was 7.5 cm. The flume motor was set to 15 Hz, and the water was 22 cm deep.

Figure 57(a) shows the Arduino LoRa receiver connected to a data acquisition PC. Visible in the background is the flume with a submerged 4" PVC pipe, containing a rotating magnet flow meter. Figure 57(b) shows water flowing through the submerged flow-meter pipe. Also present is the magnetometer and LoRa transmitter unit, visible in a weatherproof black box on top of an aluminum shelf.

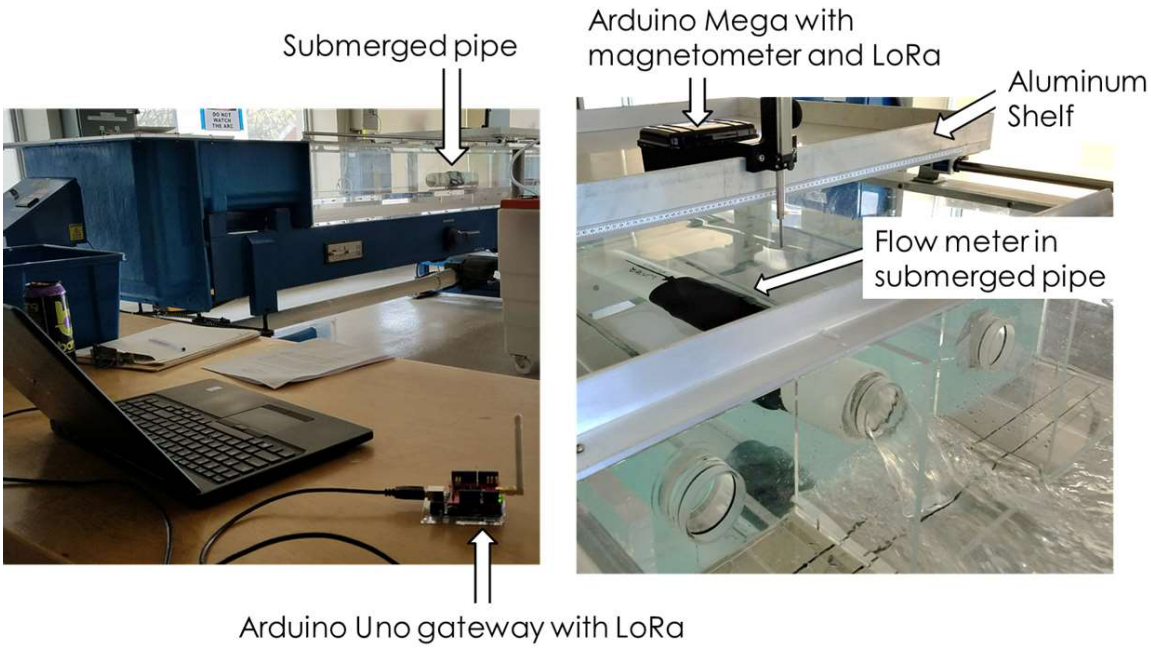

Figure 57 Left: LoRa Arduino receiver connected to data-acquisition PC, and right: rotating magnet flow meter submerged in flume

Magnetic telemetry was successful through water and the aluminum shelf, as was LoRa transmission across the room. Table 5 shows calculated frequency information for the X, Y, and Z axes of the Arduino magnetometer. A rotation frequency of approximately 8.38 Hz was detected. This can be used to calculate flow rate, and flow-rate information may be applied to detect pipe leaks.

X-axis	Y-axis	Z-axis
Received packet ' decrypted:X: 8.39 Estimated SNR (dB): 5.75	Received packet ' decrypted:Y: 8.38 Estimated SNR (dB): 7.25	Received packet ' decrypted:Z: 8.38 Estimated SNR (dB): 7.25

Table 5. Readout of data recorded by data-acquisition PC

A follow-up test was performed at the Votey flume to provide a more complete flow calibration of the rotating magnet flow meter. For this test only, a second build of the flow meter was used, identical to the first version except equipped with a slightly larger 3/8-inch diameter magnet. The circular drain dam was used as before, along with a rectangular thin-plate weir installed approximately one meter downstream, as shown in Figure 58.

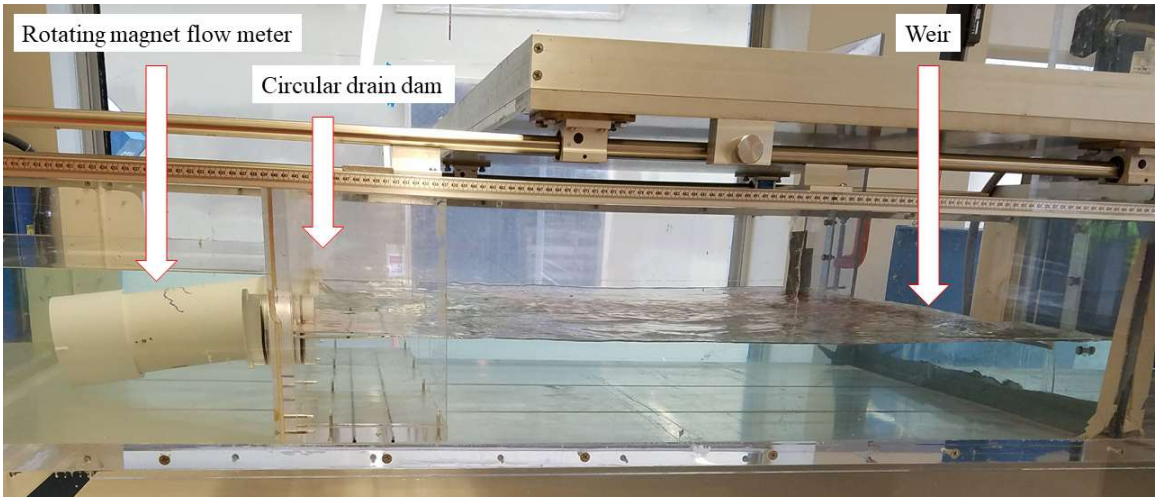

Figure 58 Flow calibration test setup for rotating magnet flow meter

The weir allows for calculation of water flow by measuring the depth of the water flowing over the weir. By making the reasonable assumption that the volume of water between the circular drain dam and the weir is roughly constant, calculating water flow over the weir gives a good measure of water flow through the dam, and therefore, through the rotating magnet flow meter. The height of the water flowing over the weir is converted to flow using the Kinsvater and Carter weir equation:

$$Q\left(\frac{m^3}{sec}\right) = C_{KC}\left(1 + a_{kc}\frac{h}{P}\right)(b + k_b)\sqrt{g}(h + 0.001)^{\frac{3}{2}} \quad (24)$$

where C_{KC}, a_{KC}, k_b are coefficient values, g is acceleration due to gravity, h is the height of the water above the weir plate, P is the height of the weir plate, and b is the width of the weir opening. These are shown in Figure 59(a). C_{KC}, a_{KC}, k_b are determined by the relationship b/B, where B is the width of the flume.

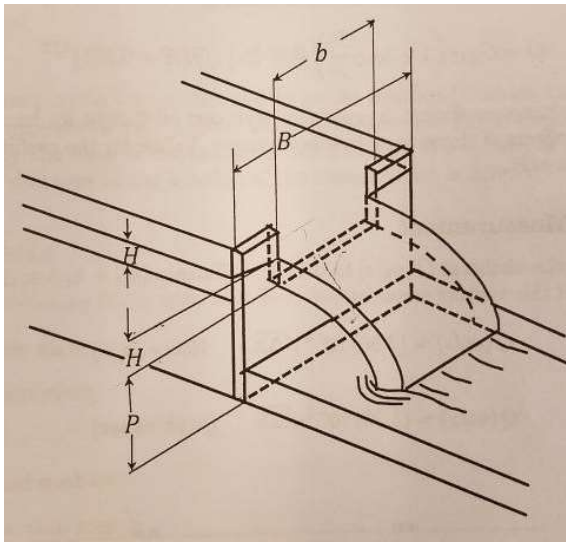

(a)

b/B	C_{KC}	a_{KC}	K_b	Type of weir
1	0.567	0.125	-0.0010	Full width
0.9	0.564	0.107	0.0038	
0.8	0.562	0.076	0.0042	
0.7	0.560	0.050	0.0040	
0.6	0.559	0.030	0.0035	Partially contracted
0.5	0.558	0.022	0.0030	
0.4	0.557	0.010	0.0027	
0.3	0.556	0.003	0.0025	
0.2 - 0	0.555	-0.003	0.0025	Fully contracted

(b)

Figure 59 (a) Weir dimensions detailed [42], and (b) coefficient values based on B/b

Additionally, a Venturi flow meter was used to measure the flow rate of water entering the flume, upstream of the circular drain dam. It gives flow in units of "inches of H_2O" which can be converted to a flow rate bounded by:

$$Q\left(\frac{m^3}{sec}\right) = 3.8 * 10^{-4}\sqrt{\Delta h} \quad (low\ boundary) \quad (25)$$

and

$$Q\left(\frac{m^3}{sec}\right) = 3.36 * 10^{-3}\sqrt{\Delta h} \quad (high\ boundary) \quad (26)$$

where Δh is "inches of H_2O". In this test, the low and high boundaries were averaged to give a single flow value.

The magnetic flow meter calibration was performed at three flow rates: the flume motor set to 15 Hz, 23 Hz, and 30 Hz. Test setup, including use of Arduino magnetometer/LoRa two-step IoT system, was the same as in the first flume experiment. Results are given in Figure 60, with full test data available in Appendix B.

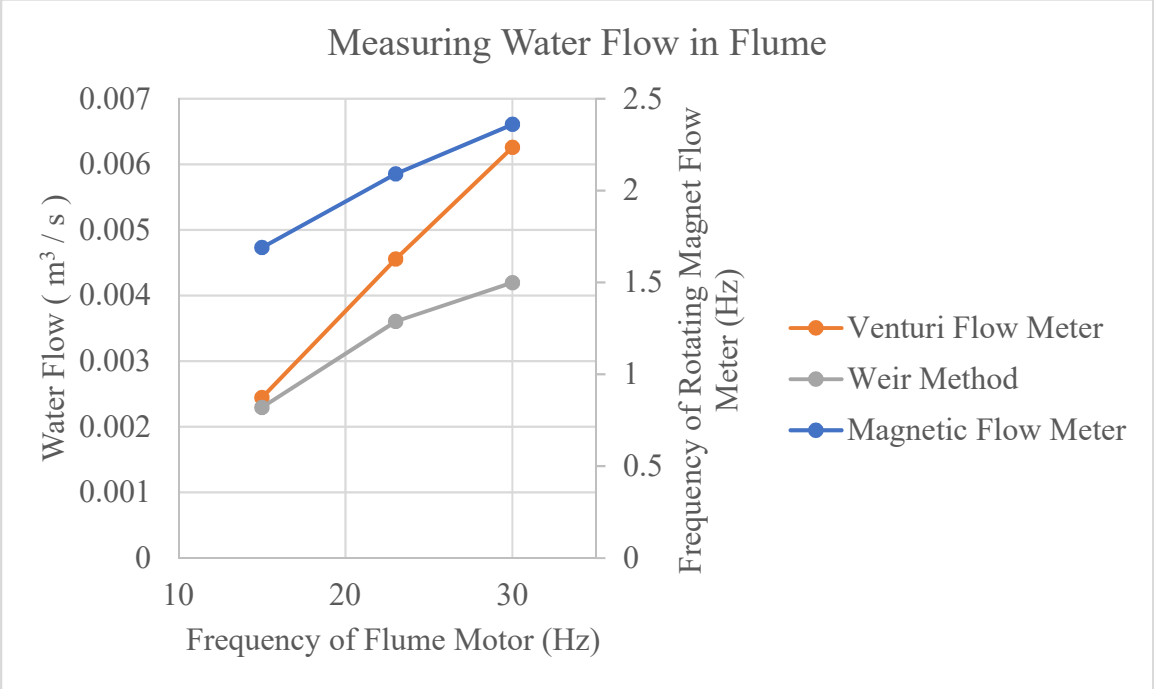

Figure 60 Calibration of rotating magnet flow meter

Inspection of Figure 60 shows that the magnetic flow meter (blue) tracks very well with the calculated flow rates obtained by using the weir method (grey). This indicates that as flow increases, the frequency of the magnetic flow meter increases appropriately, such that flow rate can be readily calculated. During testing, it was noticed that at the two higher flow rates (23 Hz and 30 Hz) the upstream portion of the flume filled faster than water could drain through the flow meter. This is evidenced by the Venturi flow meter, which measured water volume entering the flume. It is shown as the orange line in Figure 60. As the flume pump motor speed increases, the flow into the flume increases faster than the

flow leaving the flume. Thus, the orange Venturi meter line has a stepper slope than the other two measurements.

Figure 61 shows extrapolated linear trendlines comparing actual flow rate (as determined by the previous weir calculation), with rotating magnetic flow meter rotation frequency.

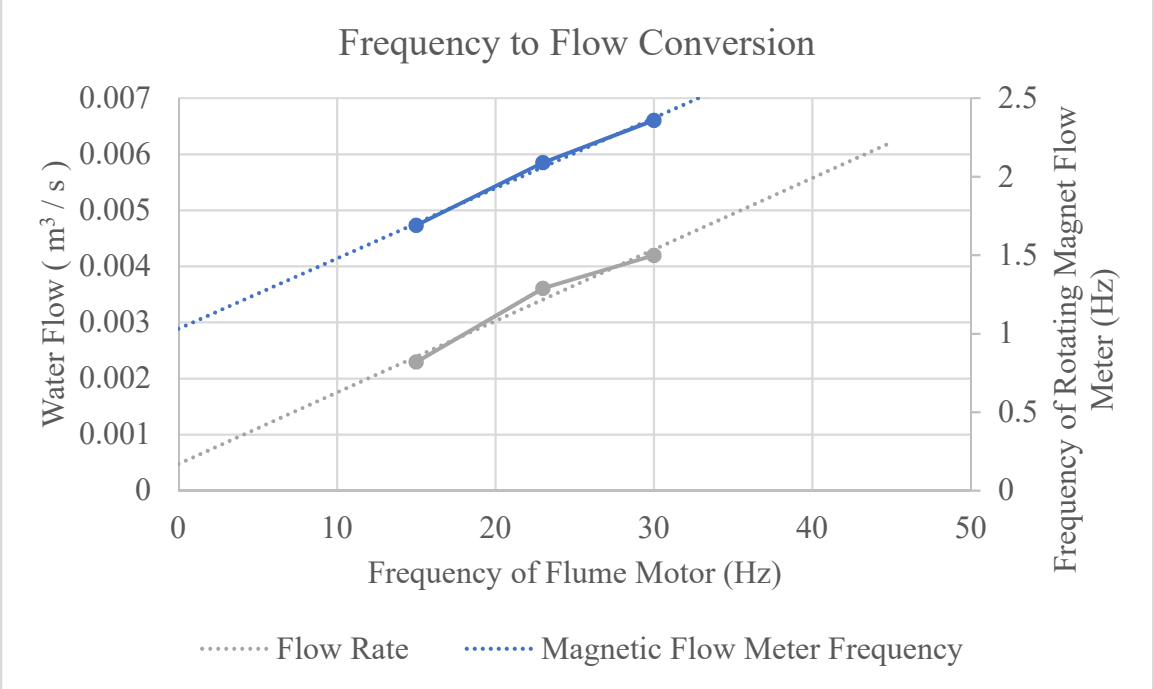

Figure 61 Frequency to flow conversion for rotating magnet flow meter

8.5 Buried Pipe

An approximately 12-foot length of 4-inch inner diameter PVC pipe was buried 12-18 inches below ground surface on a hill, as seen in Figure 62(a-d). The soil was sandy. A rotating magnet flow meter was installed approximately halfway through the length. The system is fed by a rain barrel filled by a garden hose, Figure 62(a). Figure 62(d) shows the two drains on the system—one which has a 1.5 inch diameter, and a second smaller drain with a ¾ inch diameter. This secondary drain splits off from the main pipe approximately

one foot below the flow meter. Opening and closing this drain can be used to simulate a pipe leak downstream of the flow sensor.

(a)

(b)

(c)

(d)

Figure 62 Buried pipe containing rotating magnet flow meter

Data were acquired by placing the Arduino magnetometer unit on the ground surface near to the location of the flow meter. The goal was to detect a flow difference caused by opening the secondary drain valve, i.e. detecting a leak. Preliminary data were gathered before the pipe was buried to verify the system was working; however, Y-axis data were not recorded due to an intermittent software glitch.

	Water flow (Hz)				
	X	Y	Z	Mean	Median
Unburied Pipe	6.59	-	6.57	6.58	6.58
Unburied Pipe—Leak Open	7.60	-	6.19	6.895	6.995
Buried Pipe	3.37 6.24	6.87 6.30	6.84 6.28	5.983	6.29
Buried Pipe—Leak Open	- 7.85	7.25 7.87	7.27 7.86	7.82	7.85

Table 6. Detected frequencies due to flow in buried pipe

After the pipe was buried, data was taken successfully, as shown in Table 6. With only the primary drain open, the LoRa magnetic transceiver system detected a median flow rate of 6.29 Hz. When the "leak" drain was opened, frequency increased to a median value of 7.85 Hz. This represents a flow increase of 125%. Considering the size of the pipes involved, this makes sense. The ratio of the size of the drain area of the primary drain plus the "leak" drain, compared to the area of the primary drain alone, is:

$$\frac{\pi * {r_p}^2 + \pi * {r_l}^2}{\pi * {r_p}^2} = \frac{\pi * \left(\frac{1.5}{2}\right)^2 + \pi * \left(\frac{0.75}{2}\right)^2}{\pi * \left(\frac{1.5}{2}\right)^2} = 1.25 \qquad (27)$$

So we would expect that opening the "leak" drain would result in a 125% increase in water flow, which, remarkably, is precisely what was observed. While this is clearly a simplification of the fluid dynamics processes, it does suggest that a rotating magnet flow meter transmitting to a magnetometer/LoRa transceiver may be able to detect changes in water flow associated with leak development.

9 DISCUSSION

9.1 Magnetic Telemetry for Internet of Things Leak Detection

The viability of magnetic telemetry for subsurface infrastructure monitoring was assessed through a series of computational and empirical experiments. It was determined that both rotating and vibrating magnets can be used to produce detectable oscillating magnetic fields. These magnetic signals were found to propagate well through air, as well as a variety of urban-relevant media. Tests at a local storm drain demonstrated these signal transmission capabilities in a real-world environment.

To further explore the potential of this technology, a self-powered flow meter with magnetic telemetry was designed and built. A unique two-step transmission system was developed, in which the magnetic flow meter uses oscillating magnetic fields to transmit flow information to a custom-built low-cost, low-power magnetometer-equipped LoRa IoT device. This device performs data analysis, and transmits encrypted information to a LoRa receiver, which acts as a gateway to a data-acquisition PC, network, or server. This two-step process was also used to gather and interpret data from a rotating magnet moisture sensor.

These two magnetic signaling sensors were evaluated in a variety of test environments, including a laboratory drain, a concrete slab testbed, the UVM flume, and a length of buried PVC pipe. The results provide evidence for the potential effectiveness of these types of sensors for low cost IoT-capable leak detection.

9.2 Improving Range of Magnetic IoT Sensors

While the completed magnetic sensing and LoRa system showed good system performance, it may be desirable to increase the transmission range of the magnetic sensor. The diametric neodymium magnet used in testing had a magnetic material volume of approximately 0.196 in^3. Increasing from a ¼ to a ½-inch diameter magnetic cylinder would result in a 4-fold increase in magnetic material and magnetic field strength. Because of the experimentally-verified inverse-cube signal deterioration experienced in near-field magnetic sensing, this corresponds to a range increase by a factor of $4^{1/3} = 1.59$. An increase in material volume at this scale would be relatively easy to achieve with the current design; however, significantly larger magnet volumes may be prohibitive due to the size restraints associated with fitting in small pipes, as well as the energy requirements to move a larger mass. A very large pipe with strong water flow may accommodate a larger device: for example, a 4-inch diameter neodymium cylinder 6-inches long would provide an 11.6-fold range increase compared to the magnet used in the current design. For smaller applications that demand high-strength, long-distance fields, the scaling advantages of a vibrating magnet array make it an attractive alternative.

Another way to improve magnetic sensing range is to use a more sensitive magnetometer. While the HMC5883L is appealing for IoT applications due to its extremely low cost, it may be advantageous to have certain IoT units equipped with more sensitive magnetometers. A possible candidate is the MultiDimension Technology Company USB2705A Axial Low-Field USB magnetoresistive magnetometer, which retails for around $100. A test unit was shown to have good performance, and its USB connectivity may allow for easy integration with the Arduino Mega sensor.

9.3 Oscillating Field Projection using Vibrating Magnets

The design of the Y-stator configuration for magnetic field switching has been presented and discussed. A software simulation study demonstrated the concept of field shaping with permalloy Y-stators. Literature research was conducted on the topic of coupled oscillations in order to better understand the conditions necessary for synchrony of Y-stator magnets in ganged-array arrangements. It was found that not only are arrays favored due to scaling considerations, but also due to the presence of an opposing field vector induced in the "far-away" permalloy stator. A future prototype could be built according to these findings.

9.4 Future Applications of Technology

Iot-enabled flow sensors with magnetic telemetry have the potential to integrate with and supplement other IoT and infrastructure monitoring systems. Further refinement of the technology—including less-heralded aspects like propeller design—will continue to bring these devices closer to marketability. A logical next step in system design is the integration of many IoT flow sensors into *two-way* communication networks. Current software versions only feature LoRa communication from the magnetometer-receiver/LoRa-transmitter unit, to the LoRa receiver.

A promising application for the vibrating magnetic transmitter is as a source for through-the-earth (TTE) communication systems used by coal miners in emergency scenarios. In emergency situations, it is important to have a compact means of communication with the surface that does not depend on large-scale mine infrastructure, which could become damaged in a disaster [43]. A vibrating magnet array could be both compact and low-power, making it appealing for this application. Furthermore, existing

TTE systems are generally low-bitrate and operate between 300 Hz and 5,000 Hz [43], frequencies and throughput for which a vibrating magnet array would be well suited. Development of a vibrating magnet transmitter prototype may provide more evidence of the usefulness of the technology for this and other applications.

10 REFERENCES

1. Huston, D., *Mechano-Magnetic Signaling and Sensing*. 2017, SPARK VT: University of Vermont.
2. Keyser, N., *Closeup of a few of the antenna towers of the U.S. Navy Cutler VLF transmitter facility at Cutler, Maine.* 2007.
3. Magnets4Less. Available from: http://www.magnet4less.com/images/0.375x1-TD.jpg.
4. ASCE. *2017 Infrastructure Report Card*. 2017; Available from: https://www.infrastructurereportcard.org/americas-grades/.
5. Huston, D., et al. *Mapping, Assessing and Monitoring Urban Underground Infrastructure*. in *11th International Workshop on Structural Health Monitoring 2017*. 2017. Stanford, California: DEStech Publications, Inc.
6. Labs, L. *What are LoRa & LoRaWAN?* 2017; Available from: https://www.link-labs.com/lora.
7. Prajzler, V., *LoRa, LoRaWAN and LORIOT.io.* 2015.
8. *Extreme Range Links: LoRa 868 / 900MHz SX1272 LoRa module for Arduino Waspmote and Raspberry Pi*. 2017]; Available from: https://www.cooking-hacks.com/documentation/tutorials/extreme-range-lora-sx1272-module-shield-arduino-raspberry-pi-intel-galileo/.
9. RobotShop. *LoRa Long Range Transceiver Shield 915 MHz (North America)*. 2017; Available from: http://www.robotshop.com/en/lora-long-range-transceiver-shield-915-mhz-north-america.html.
10. Arduino. *ARDUINO UNO REV3*. 2017; Available from: https://store.arduino.cc/usa/arduino-uno-rev3.
11. Arduino. *ARDUINO MEGA 2560 REV3*. 2017; Available from: https://store.arduino.cc/usa/arduino-mega-2560-rev3.
12. Huston, D., T. Xia, and D. Burns, *DARPA AMEBA Technical Area 2*. 2017, DARPA: University of Vermont.
13. TStein. Available from: https://en.wikipedia.org/wiki/File:Earths_Magnetic_Field_Confusion.svg.
14. Huston, D., *Structural Sensing, Health Monitoring, and Performance Evaluation*. Series in Sensors, ed. B. Jones and W.B. Spillman. 2011, Burlington, USA: Taylor and Francis. 645.
15. Wangsness, R.K., *Electromagnetic Fields*. 1986, New York: John Wiley & Sons.
16. NIST. *The Hall Effect*. 2016; Available from: https://www.nist.gov/pml/engineering-physics-division/hall-effect.
17. FraunhoferIIS. Available from: https://upload.wikimedia.org/wikipedia/commons/7/77/Hall_Sensor.webm.
18. Tong, D., *The Quantum Hall Effect: TIFR Infosys Lectures*. 2016, Cornell University Library.
19. Quasdorf, J. *A Case Study: MR vs. Hall Effect for Position Sensing*. 2005; Available from: https://www.sensorsmag.com/components/a-case-study-mr-vs-hall-effect-for-position-sensing.

20. Arrow-Electronics. *Magnetoresistive Sensor*. 2017; Available from: https://www.arrow.com/en/categories/sensors/magnetoresistive-sensors.
21. *How Atomic Magnetometers Work*. 2012; Available from: http://mfam.geometrics.com/atomicmagnetomet.html.
22. Twarge. *SimpleVectors.svg*. 2008; Atomic magnetometer principle of operation, depicting alkali atoms polarized by a circularly polarized pump beam, precessing in the presence of a magnetic field and being detected by optical rotation of a linearly polarized pump beam.]. Available from: https://en.wikipedia.org/wiki/File:SimpleVectors.svg.
23. Pappas, D.P. *High Sensitivity Magnetic Field Sensor Technology overview*. 2008. 50.
24. *D48DIA*. [cited 2017; Available from: https://www.kjmagnetics.com/proddetail.asp?prod=D48DIA.
25. *Neodymium Magnets 3/8 in x 1 in Diametrically Magnetized Cylinder*. Available from: http://appliedmagnets.com/neodymium-magnets-3-8-in-x-1-in-diametrically-magnetized-cylinder-p-89.html.
26. *Practical Introduction to Frequency-Domain Analysis*. Documentation 2017 [cited 2017; Available from: https://www.mathworks.com/help/signal/examples/practical-introduction-to-frequency-domain-analysis.html.
27. Strogatz, S.H. and I. Stewart, *Coupled Oscillators and Biological Synchronization*, in *Scientific American*. 1993. p. 102-109.
28. Strogatz, S.H., *Sync: The Emerging Science of Spontaneous Order*. 2003: Hyperion.
29. Krousgrill, C.M. and J.F. Rhoads. 2013 [cited 2017; Available from: https://i.ytimg.com/vi/lZPtFDXYQRU/maxresdefault.jpg.
30. Quinn, D.D., R.H. Rand, and S.H. Strogatz, *Singular unlocking transition in the Winfree model of coupled oscillators.* Physical Review, 2007. **3**(75): p. 036218.
31. Peskin, C.S., *Principles of Electrophysiology with Special Reference to the Heart*, in *Mathematical Aspects of Heart Physiology*. 1975, Courant Institute Lecture Notes. p. 241-278.
32. Mirollo, R.E. and S.H. Strogatz, *The spectrum of the locked state for the Kuramoto model of coupled oscillators.* Physica D, 2005. **205**: p. 249-266.
33. Strogatz, S.H. *Spontaneous Synchronization in Nature*. in *1997 IEEE International Frequency Control Symposium*. 1997.
34. Winfree, A.T., *Biological Rhythms and the Behavior of Populations of Coupled Oscillators.* J. Theoret. Biol., 1967(16): p. 15-42.
35. Strogatz, S.H., *From Kuramoto to Crawford: exploring the onset of synchronization in populations of coupled oscillators.* Physica D, 2000. **143**: p. 1-20.
36. Bar-Eli, K. and B.G. Ermentrout. *Oscillation death*. 2008 [cited 2017; Available from: http://www.scholarpedia.org/article/Oscillation_death.
37. Kuramoto, Y. *Self-entrainment of a population of coupled non-linear oscillators*. in *International Symposium on Mathematical Problems in Theoretical Physics*. 1975. Kyoto: Springer.

38. Bronski, J.C., L. DeVille, and M.J. Park, *Fully synchronous solutions and the synchronization phase transition for the finite-N Kuramoto model.* Chaos, 2012(22): p. 17.
39. Yeung, S.M.K. and S.H. Strogatz, *Time Delay in the Kuramoto Model of Coupled Oscillators.* Physical Review Letters, 1998. **82**(3): p. 648-651.
40. AZOSensors. Available from: https://www.azosensors.com/images/equipments/EquipmentImage_516.jpg.
41. DomoticX.com. Available from: http://domoticx.com/wp-content/uploads/Kompas-3-assen-HMC5883L-arduino-schema.png.
42. ; Available from: https://encrypted-tbn3.gstatic.com/images?q=tbn:ANd9GcRbk18p-_WqnxCwU0pxJwohx3OM81lq3t9ceqtfivlsmragoan3zg.
43. Damiano, N., *Through-the-Earth, Post-Accident Communications—an Emerging Technology*, in *CDC NIOSH Technology News*. 2012, DHHS (NIOSH) Publication: Pittsburgh, PA.

11 APPENDIX A

11.1 Arduino Code

11.1.1 LoRa Transmitter

```
/*
Filename: “Time_Amplitude_Encrypted_Liter_Transmitter_rev3”

An Arduino code example for interfacing with the HMC5883

Credits:

Dan Orfeo
dan.orfeo@gmail.com

Example of use of the FFT libray
Copyright (C) 2014 Enrique Condes

by: Jordan McConnell
 SparkFun Electronics
 created on: 6/30/11
 license: OSHW 1.0, http://freedomdefined.org/OSHW

Analog input 4 I2C SDA
Analog input 5 I2C SCL
*/

#include <Wire.h> //I2C Arduino Library
#include "arduinoFFT.h"
#include <SPI.h>
#include <LoRa.h>
#include <stdlib.h>
#include <AESLib.h>

arduinoFFT FFT = arduinoFFT(); /* Create FFT object */
/*
These values can be changed in order to evaluate the functions
*/
const uint16_t samples = 256; //This value MUST ALWAYS be a power of 2
double samplingFrequency = 20;
/*
These are the input and output vectors
Input vectors receive computed results from FFT
```

```
*/
double xImag[samples];
double yImag[samples];
double zImag[samples];

#define SCL_INDEX 0x00
#define SCL_TIME 0x01
#define SCL_FREQUENCY 0x02

#define address 0x1E //0011110b, I2C 7bit address of HMC5883

void setup(){
 //Initialize Serial and I2C communications
 Serial.begin(9600);
 Wire.begin();

 //Put the HMC5883 IC into the correct operating mode
 Wire.beginTransmission(address); //open communication with HMC5883
 Wire.write(0x02); //select mode register
 Wire.write(0x00); //continuous measurement mode
 Wire.endTransmission();

 int x,y,z; //triple axis data
 int i;
 int n;
 int threshold = 50;             // set feature amplitude threshold value
 double xArray[samples];
 double yArray[samples];
 double zArray[samples];

 while (!Serial);
 Serial.println(" ");
 if (!LoRa.begin(915E6)) {
  Serial.println("Starting LoRa failed!");
  while (1);
 }

 for (n=0; ; n++){
  for (i = 0; i < samples; i++){

    //Tell the HMC5883 where to begin reading data
    Wire.beginTransmission(address);
    Wire.write(0x03); //select register 3, X MSB register
    Wire.endTransmission();
```

```
    //Read data from each axis, 2 registers per axis
     Wire.requestFrom(address, 6);
     if(6<=Wire.available()){
       x = Wire.read()<<8; //X msb
       x |= Wire.read(); //X lsb
       z = Wire.read()<<8; //Z msb
       z |= Wire.read(); //Z lsb
       y = Wire.read()<<8; //Y msb
       y |= Wire.read(); //Y lsb
     }

     //Add data to arrays
     xArray[i] = x;
     yArray[i] = y;
     zArray[i] = z;

     delay(50);}

//    PrintVector(xArray, (samples >> 1), SCL_INDEX);    // print raw x,y,z data to serial
port
//    PrintVector(yArray, (samples >> 1), SCL_INDEX);
//    PrintVector(zArray, (samples >> 1), SCL_INDEX);

   int xmaxValue = 0;                          // get max values for x,y,z
   int j;
   for (j = 1; j < samples; ++j) {
     if ( abs(xArray[j]) > abs(xmaxValue) ) {
        xmaxValue = xArray[j];
     }
   }

   Serial.println("X-max amplitude:");
   Serial.println(xmaxValue);

   ////////////////////////////

   int ymaxValue = 0;
   int k;
   for (k = 1; k < samples; ++k) {
     if ( abs(yArray[k]) > abs(ymaxValue) ) {
        ymaxValue = yArray[k];
     }
   }

   Serial.println("Y-max amplitude:");
   Serial.println(ymaxValue);
```

```
  ////////////////////////////

  int zmaxValue = 0;
  int l;
  for (l = 1; l < samples; ++l) {
   if ( abs(zArray[l]) > abs(zmaxValue) ) {
      zmaxValue = zArray[l];
   }
  }

  Serial.println("Z-max amplitude:");
  Serial.println(zmaxValue);
  Serial.println(" ");

  //Peform FFT on the x data Array
  FFT.Windowing(xArray, samples, FFT_WIN_TYP_HAMMING, FFT_FORWARD);
/* Weigh data */
  FFT.Compute(xArray, xImag, samples, FFT_FORWARD); /* Compute FFT */
  FFT.ComplexToMagnitude(xArray, xImag, samples); /* Compute magnitudes */
  double xvalue = FFT.MajorPeak(xArray, samples, samplingFrequency);

  //Peform FFT on the y data Array
  FFT.Windowing(yArray, samples, FFT_WIN_TYP_HAMMING, FFT_FORWARD);
/* Weigh data */
  FFT.Compute(yArray, yImag, samples, FFT_FORWARD); /* Compute FFT */
  FFT.ComplexToMagnitude(yArray, yImag, samples); /* Compute magnitudes */
  double yvalue = FFT.MajorPeak(yArray, samples, samplingFrequency);

  //Peform FFT on the z data Array
  FFT.Windowing(zArray, samples, FFT_WIN_TYP_HAMMING, FFT_FORWARD);
/* Weigh data */
  FFT.Compute(zArray, zImag, samples, FFT_FORWARD); /* Compute FFT */
  FFT.ComplexToMagnitude(zArray, zImag, samples); /* Compute magnitudes */
  double zvalue = FFT.MajorPeak(zArray, samples, samplingFrequency);

  // check to see if x,y,z signals were strong enough to warrent transmitting calculated FFT
data, if not, replace frequency with 0

  if (abs(xmaxValue) > threshold) {
   xvalue = xvalue;
  }
  else {
   xvalue = 0;
  }
```

```
  if (abs(ymaxValue) > threshold) {
    yvalue = yvalue;
  }
  else {
    yvalue = 0;
  }

  if (abs(zmaxValue) > threshold) {
    zvalue = zvalue;
  }
  else {
    zvalue = 0;
  }

  Serial.println("X-direction frequency:");
  Serial.println(xvalue);
  Serial.println("Y-direction frequency:");
  Serial.println(yvalue);
  Serial.println("Z-direction frequency:");
  Serial.println(zvalue);

  String xstring = "";                    // sketch_oct17a_slim AES128-bit encryption
  xstring = String(xvalue,3);                 // x-data encryption

  char Ax = 'X';
  char Bx = ':';
  char Cx = ' ';
  char Dx = xstring[0];
  char Ex = xstring[1];
  char Fx = xstring[2];
  char Gx = xstring[3];
  char Hx = ' ';
  char Ix = ' ';
  char Jx = ' ';
  char Kx = ' ';
  char Lx = ' ';
  char Mx = ' ';
  char Nx = ' ';
  char Ox = ' ';
  char Px = ' ';

  uint8_t key[] = {0,1,2,3,4,5,6,7,8,9,10,11,12,13,14,15};
  char datax[] = {Ax, Bx, Cx, Dx, Ex, Fx, Gx, Hx, Ix, Jx, Kx, Lx, Mx, Nx, Ox, Px}; //16
chars == 16 bytes
  aes128_enc_single(key, datax);
```

```
  String ystring = "";                  // sketch_oct17a_slim AES128-bit encryption
  ystring = String(yvalue,3);               // y-data encryption

  char Ay = 'Y';
  char By = ':';
  char Cy = ' ';
  char Dy = ystring[0];
  char Ey = ystring[1];
  char Fy = ystring[2];
  char Gy = ystring[3];
  char Hy = ' ';
  char Iy = ' ';
  char Jy = ' ';
  char Ky = ' ';
  char Ly = ' ';
  char My = ' ';
  char Ny = ' ';
  char Oy = ' ';
  char Py = ' ';

  char datay[] = {Ay, By, Cy, Dy, Ey, Fy, Gy, Hy, Iy, Jy, Ky, Ly, My, Ny, Oy, Py}; //16
chars == 16 bytes
  aes128_enc_single(key, datay);

  String zstring = "";                  // sketch_oct17a_slim AES128-bit encryption
  zstring = String(zvalue,3);               // z-data encryption

  char Az = 'Z';
  char Bz = ':';
  char Cz = ' ';
  char Dz = zstring[0];
  char Ez = zstring[1];
  char Fz = zstring[2];
  char Gz = zstring[3];
  char Hz = ' ';
  char Iz = ' ';
  char Jz = ' ';
  char Kz = ' ';
  char Lz = ' ';
  char Mz = ' ';
  char Nz = ' ';
  char Oz = ' ';
  char Pz = ' ';

  char dataz[] = {Az, Bz, Cz, Dz, Ez, Fz, Gz, Hz, Iz, Jz, Kz, Lz, Mz, Nz, Oz, Pz}; //16
chars == 16 bytes
```

```
    aes128_enc_single(key, dataz);

//    Serial.println(" ");
//    Serial.print(datax);
//    Serial.print(" ");
//    Serial.print(datay);
//    Serial.print(" ");
//    Serial.print(dataz);
//    Serial.println(" ");

    delay(150);

    // send packet
    LoRa.beginPacket();
    LoRa.print(datax);
    LoRa.endPacket();

    delay(150);

    LoRa.beginPacket();
    LoRa.print(datay);
    LoRa.endPacket();

    delay(150);

    LoRa.beginPacket();
    LoRa.print(dataz);
    LoRa.endPacket();

    delay(150);

    software_Reset();
  }
}

void software_Reset() // Restarts program from beginning but does not reset the peripherals
and registers
{
asm volatile ("  jmp 0");
}

void loop() {
  // put your main code here, to run repeatedly:

}
```

```
void PrintVector(double *vData, uint16_t bufferSize, uint8_t scaleType) // print doubles
{
 for (uint16_t i = 0; i < bufferSize; i++)
 {
  double abscissa;
  /* Print abscissa value */
  switch (scaleType)
  {
    case SCL_INDEX:
      abscissa = (i * 1.0);
 break;
    case SCL_TIME:
      abscissa = ((i * 1.0) / samplingFrequency);
 break;
    case SCL_FREQUENCY:
      abscissa = ((i * 1.0 * samplingFrequency) / samples);
 break;
  }
  Serial.print(abscissa, 6);
  Serial.print(" ");
  Serial.print(vData[i], 4);
  Serial.println();
 }
 Serial.println();
}
```

11.1.2 LoRa Receiver: “Encrypted_LoRa_Receiver_rev2”

```
/*
Filename: “Encrypted_LoRa_Receiver_rev2”

*/

#include <SPI.h>
#include <LoRa.h>
#include <TimeLib.h>
#include <AESLib.h>

void setup() {
 Serial.begin(9600);
 while (!Serial);

 Serial.println("LoRa Receiver");

 if (!LoRa.begin(915E6)) {
  Serial.println("Starting LoRa failed!");
```

```
    while (1);
  }
}

void loop() {
  // try to parse packet
  int packetSize = LoRa.parsePacket();
  if (packetSize) {
    // received a packet
    Serial.println(" ");
    Serial.println("Received packet '");

    // read packet
    while (LoRa.available()) {

      String datastring = LoRa.readString();

//      Serial.print(datastring[0]);
//      Serial.print(datastring[1]);
//      Serial.print(datastring[2]);
//      Serial.print(datastring[3]);
//      Serial.print(datastring[4]);
//      Serial.print(datastring[5]);
//      Serial.print(datastring[6]);
//      Serial.print(datastring[7]);
//      Serial.print(datastring[8]);
//      Serial.print(datastring[9]);
//      Serial.print(datastring[10]);
//      Serial.print(datastring[11]);
//      Serial.print(datastring[12]);
//      Serial.print(datastring[13]);
//      Serial.print(datastring[14]);
//      Serial.print(datastring[15]);

      char A = datastring[0];
      char B = datastring[1];
      char C = datastring[2];
      char D = datastring[3];
      char E = datastring[4];
      char F = datastring[5];
      char G = datastring[6];
      char H = datastring[7];
      char I = datastring[8];
      char J = datastring[9];
      char K = datastring[10];
      char L = datastring[11];
```

```
    char M = datastring[12];
    char N = datastring[13];
    char O = datastring[14];
    char P = datastring[15];

    uint8_t key[] = {0,1,2,3,4,5,6,7,8,9,10,11,12,13,14,15};
    char data[] = {A, B, C, D, E, F, G, H, I, J, K, L, M, N, O, P}; //16 chars == 16 bytes
    aes128_dec_single(key, data);
    Serial.print("decrypted:");
    Serial.println(data);
   }

   // print RSSI of packet
   Serial.print("Estimated SNR (dB): ");
   Serial.println(LoRa.packetSnr());
   Serial.print("' with RSSI ");
   Serial.println(LoRa.packetRssi());
   Serial.print(day());
   Serial.print("/");
   Serial.print(month());
   Serial.print("/");
   Serial.print(year());
   Serial.print(" ");
   Serial.print(hour());
   Serial.print(":");
   Serial.print(minute());
   Serial.print(":");
   Serial.print(second());
   Serial.println(" ");
  }
}
```

11.1.3 DC Motor (created by Dr. Dylan Burns)

```
#include <AFMotor.h>


AF_DCMotor motor(2, MOTOR12_64KHZ); // create motor #2, 64KHz pwm
AF_DCMotor motora(2, MOTOR12_64KHZ); // create motor #2, 64KHz pwm

  const int threshold1 = 675;  //moisture / dielectric threshold value
  const int threshold2 = 600;  //moisture / dielectric threshold value

void setup() {
  Serial.begin(9600);           // set up Serial library at 9600 bps
  //Serial.println("Motor test!");
```

```
  motor.setSpeed(100);     // set the speed to 200/255
  motora.setSpeed(500);     // set the speed to 200/255

}

void loop() {
   // read the input on analog pin 0:
  int sensorValue = analogRead(A0);
  // print out the value you read:
  Serial.println(sensorValue);
  delay(1);        // delay in between reads for stability

   // if the analog value is high enough, turn on the LED:
  if (sensorValue > threshold2 && sensorValue < threshold1) {
    motor.run(FORWARD);      // turn it on going forward
  //delay(1000);

  }else if (sensorValue < threshold2) {
    motora.run(FORWARD);      // turn it on going forward
  //delay(1000);

  } else {
    motor.run(RELEASE);      // stopped
    motora.run(RELEASE);      // stopped
   //  delay(1000);
  }

//  motor.run(FORWARD);      // turn it on going forward
//  delay(1000);

//  Serial.print("tock");
//  motor.run(BACKWARD);     // the other way
//  delay(1000);
//
//  Serial.print("tack");
//  motor.run(RELEASE);      // stopped
//  delay(1000);
}
```

11.1.4 DC Motor Moisture (created by Dr. Dylan Burns)

```
#include <AFMotor.h>


AF_DCMotor motor(2, MOTOR12_64KHZ); // create motor #2, 64KHz pwm
```

```
AF_DCMotor motora(2, MOTOR12_64KHZ); // create motor #2, 64KHz pwm

  const int threshold1 = 675;  //moisture / dielectric threshold value
  const int threshold2 = 600;  //moisture / dielectric threshold value

void setup() {
  Serial.begin(9600);           // set up Serial library at 9600 bps
  //Serial.println("Motor test!");

  motor.setSpeed(100);     // set the speed to 200/255
  motora.setSpeed(500);     // set the speed to 200/255

}

void loop() {
   // read the input on analog pin 0:
  int sensorValue = analogRead(A0);
  // print out the value you read:
  Serial.println(sensorValue);
  delay(1);        // delay in between reads for stability

   // if the analog value is high enough, turn on the LED:
  if (sensorValue > threshold2 && sensorValue < threshold1) {
    motor.run(FORWARD);      // turn it on going forward
  //delay(1000);

  }else if (sensorValue < threshold2) {
    motora.run(FORWARD);      // turn it on going forward
  //delay(1000);

  } else {
    motor.run(RELEASE);      // stopped
    motora.run(RELEASE);      // stopped
   //  delay(1000);
  }
//  motor.run(FORWARD);      // turn it on going forward
//  delay(1000);

//  Serial.print("tock");
//  motor.run(BACKWARD);     // the other way
//  delay(1000);
//
//  Serial.print("tack");
//  motor.run(RELEASE);      // stopped
//  delay(1000);
}
```

11.2 Matlab Code

11.2.1 Process Data for HMR2300 Magnetometer: "hmr2300_reader_III.m"

```
function [x y z]=hmr2300_reader(fname)
clear all
clc
close all;
filename='magnet under concrete_off.txt'
fid=fopen(filename);  %change to txt file you are procressing from HMR
a=fread(fid);
fclose(fid);

% Determine number of lines in text file
fid = fopen(filename);
allText = textscan(fid,'%s','delimiter','\n');
number_of_lines = length(allText{1})-4;
fclose(fid)

A=char(a);
ind=find(a==13);

B=[];
for k=2:length(ind)-3,
    b=char(a(ind(k)+2:ind(k)+28))';
    B=cat(1,B,b);
end

for k=2:size(B,1),
    x(k-1)=str2num(strcat(B(k,1),B(k,3),B(k,5:7)))*1/.15; %A/D counts
to nT
    y(k-1)=str2num(strcat(B(k,10),B(k,12),B(k,14:16)))*1/.15;
    z(k-1)=str2num(strcat(B(k,19),B(k,21),B(k,23:25)))*1/.15;
end

figure;
plot(x, 'b');hold on;plot(y,'r');plot(z,'g');
legend('x = Blue','y = Red', 'z = Green')


%-----------------X Axis FFT---------------------------
Fs = 20;              % Sampling frequency--------
T = 1/Fs;             % Sampling period
L = number_of_lines;  % Length of signal------------
t = (0:L-1)*T;        % Time vector

upper = 2000;            % Comment this line out to remove upper limit
value

X = fft(x);
P2 = abs(X/L);
P1 = P2(1:L/2+1);
```

```
P1(2:end-1) = 2*P1(2:end-1);

figure()
f = Fs*(0:(L/2))/L;
plot(f,P1)
xlim([0 10])
ylim([0 upper])
title('Single-Sided Amplitude Spectrum of X(t)')
xlabel('f (Hz)')
ylabel('|P1(f)|')

%-----------------y Axis FFT--------------------------

Y = fft(y);
P2 = abs(Y/L);
P1 = P2(1:L/2+1);
P1(2:end-1) = 2*P1(2:end-1);

figure()
f = Fs*(0:(L/2))/L;
plot(f,P1)
xlim([0 10])
ylim([0 upper])
title('Single-Sided Amplitude Spectrum of Y(t)')
xlabel('f (Hz)')
ylabel('|P1(f)|')

%-----------------z Axis FFT--------------------------

Z = fft(z);
P2 = abs(Z/L);
P1 = P2(1:L/2+1);
P1(2:end-1) = 2*P1(2:end-1);

figure()
f = Fs*(0:(L/2))/L;
plot(f,P1)
xlim([0 10])
ylim([0 upper])
title('Single-Sided Amplitude Spectrum of Z(t)')
xlabel('f (Hz)')
ylabel('|P1(f)|')
```

12 APPENDIX B

12.1 Rotating Magnet Flow Meter Flume Calibration Data

Hz	in H20	h (mm)	15 Hz				23 Hz				30 Hz			
			x	y	z		x	y	z		x	y	z	
15	1.7483	17.93		1.32	1.33	1.33		1.1	1.1	1.09		2.09	2.09	2.09
	1.6739			1.51	1.51			1.5	1.5			2.26	2.26	2.26
23	6.0753	24.56		1.61	1.61			1.71	1.71	1.71		2.36	2.36	2.36
	5.8058			1.69	1.69	1.69		2.07	2.08	2.09		2.47	2.47	2.46
30	11.206	27.26		1.77	1.77			1.4	1.4	6.27		2.55		2.55
				1.83	1.83	1.83		2.09	2.09	2.09		2.53	2.52	2.52
					1.83	1.83		2.19	2.19	2.19		2.5	2.51	
				1.91	1.91	0.46		2.28	2.28	2.28		2.26	2.26	2.26
						0.45		2.36	2.36	2.36				
				1.94	1.94	0.45								
				1.93	1.93	0.46								
		Median		1.69				2.09				2.36		

	15 Hz			23 Hz			30 Hz		
	in H20	Median		in H20	Median		in H20	Median	
	1.7483	1.7111		6.0753	5.94055		11.206	11.206	
	1.6739			5.8058					
Q low	0.000497		Q low	0.000926		Q low	0.001272		
Q high	0.004395		Q high	0.008189		Q high	0.011248		
Q average	0.002446		Q average	0.004558		Q average	0.00626		

Magnetic Flow Meter	
15	1.69
23	2.09
30	2.36

Venturi Flow Meter	
15	0.002446
23	0.004558
30	0.00626

Ckc	0.558
akc	0.022
kb	0.003
P	0.11
b	0.5
B	1
g	9.8

15 Hz		23 Hz		30 Hz	
h (mm)	h (m)	h (mm)	h (m)	h (mm)	h (m)
17.93	0.01793	24.56	0.02456	27.26	0.02726
Q	0.002297	Q	0.003608	Q	0.004197

Weir Dam	
15	0.002297
23	0.003608
30	0.004197